Nanoparticle-enhanced Foam in Carbonate and Sandstone Reservoirs

CONFIDENTIAL

Joris Roebroeks

MSc Thesis

Title : Nanoparticle-enhanced Foam in Carbonate and Sandstone Reservoirs

Author : Joris Roebroeks

Date : October 2014
Professor(s) : Dr. ir. Rouhollah Farajzadeh
Supervisor(s) : Dr. ir. Rouhollah Farajzadeh and Dr. Ali Akbar Eftekhari
Postal Address : Section for Petroleum Engineering
Department of Geoscience & Engineering
Delft University of Technology
P.O. Box 5028
The Netherlands
Telephone: : (+31) 15 2781328 (secretary)

Abstract

Foam flooding as a mechanism to enhance oil recovery has been intensively studied and is the subject of multiple research groups. However, limited stability of surfactant-generated foam in presence of oil and low chemical stability of surfactants in the high temperature and high salinity of an oil reservoir are among the reasons for foam EOR not being widely applied in the field.

Unlike surfactants, nanoparticles, which are shown to be effective in stabilizing bulk foam, are chemically stable in a wide range of physicochemical conditions. Recent studies suggest that synthesized nanoparticles with altered surface properties can aid foam generation and increase foam stability in porous media. However, large scale production of nanoparticles and altering its surface properties can be expensive and in some cases impractical.

In this study, the focus lies on a silica-based nanoparticle that is available in large quantities and can be processed economically without separate surface treatment, which gives it the potential to become a practical solution in the field. The synergistic effect of a combination of low concentration surfactant and low concentration nanoparticle in increasing the stability of foam in porous media is demonstrated in this paper. The research is primarily conducted by performing core-flooding experiments under varying conditions to quantitatively assess and compare the potential of the nanoparticle-enhanced foam.

Two types of reservoir rocks have been investigated: sandstone and carbonate rocks, of which the latter is known to be challenging to successfully flood with foam. The results have been compared to experiments at lower pressures and ambient temperature. It is observed that by adding even low concentrations of nanoparticles to a near-CMC surfactant solution, the foam viscosity can considerably increase. The experimental result shows that addition of small amount of nanoparticles creates foam whose strength is equivalent to the foam generated with 10-fold surfactant concentration which can lead to more economical foam flooding process.

List of abbreviations

M:	Mobility ratio [-]
k:	Permeability [m^2]
μ:	viscosity [Pa s]
f_g:	foam quality [-]
V:	volume
σ:	surface tension [N/m]
Γ:	surface excess concentration [mol/m^2]
μ:	chemical potential [J/mol]
p:	pressure [Pa]
Π_d:	disjoining pressure [Pa]
P_c:	capillary pressure [Pa]
S:	saturation [-]
n:	bubble density or Corey exponent
λ:	mobility
A:	cross-sectional area [m^2]
L:	length [m]
q:	flow rate [m^3/s]
k_H:	Henry's Constant [L atm/mol]
N_{ca}:	capillary number
F:	force [N]
v:	velocity [m/s]
t:	time [s]
ε:	permittivity [m^2]
T:	temperature [˚K or ˚C]
z:	electrolyte charge [C]
A:	Hamaker Constant [J]
h:	distance [m]
F:	solid fraction [-]
D_p:	particle diameter [m]
E:	Energy [J]
ϑ:	contact angle [˚]

Subscripts:

r:	relative
o:	oil
w:	water
g:	gas
cw:	connate water
gr:	residual gas
f:	foam
nf:	no foam
i:	injectant or component *i*

Table of contents

List of figures

List of tables

1 Introduction

Energy demand and supply

The usage of hydrocarbon resources is deeply woven into modern society. Our transportation system largely relies on this source of energy, hydrocarbons are used to generate electricity, and many consumer products require hydrocarbons as a raw production material. Because of the reliance of our civilization on the petroleum industry, it has become an integral part of technology, society and politics.

Oil is a finite resource. The rate at which new oil is maturing is much slower than mankind is currently extracting it from the subsurface. As oil and gas fields get depleted, new sources of hydrocarbon need to be found in order to keep up with demand. Therefore energy companies put a large effort to meet the increasing demand. However, ever after 1980 the amount of oil that has been produced exceeded the amount of new discoveries according to the International Energy Agency. Based on the decline in new oil discoveries and the prediction for oil consumption, M. King Hubbert, a geoscientist working for Shell, suggested 'Peak oil' to occur around 2005 (Deffeyes, 2001). Peak oil would be the event where the point of maximum oil production is reached, after which the amount of oil produced per day would decline.

Hubbert did not consider the technological advancements. Our methods to find new oil fields improved, and with more effective methods the industry was able to economically produce fields that were deemed uneconomical previously. An example are the current developments in shale technology. With a combination of horizontal drilling and hydraulic fracturing technologies the very tight shale plays became accessible for production. Not only gas could be produced, but oil as well. At the 4th of July 2014 Bloomberg reported the news the United States of America had overtaken Saudi Arabia as biggest oil producer. This was made possible by the surge in oil production from shale plays, such as the Bakken formation in North Dakota.

In addition to finding new oil fields and radical new technologies unlocking new supplies, a constant factor throughout the years has been to improve recovery of existing reservoirs. In the early days of the petroleum industry, 'depletion' of the reservoir was achieved by drilling the reservoir and letting natural oil flow do the work. Gas expansion and natural water drives were able to let oil flow, but achieved only very low recovery rates. In order to improve recovery, the mechanism for recovery had to be improved. The mechanisms used for oil recovery can be distinguished in primary, secondary and tertiary recovery.

Primary, secondary and tertiary recovery

Primary recovery relies on natural mechanisms to drive oil to the surface. A natural water drive from an aquifer displaces the oil towards the producing wells, for example. The expansion of a gas cap yields a similar effect. The recovery factor (which is the ratio of oil that can be ultimately produced divided by the oil that is initially in place) that can be achieved with primary production is typically around 5 – 15% (Tzimas et al., 2005).

Production from wells can be further improved by applying secondary recovery techniques. These techniques are also referred to as 'Improved Oil Recovery' or IOR processes. They aim to maintain the reservoir pressure and hence displace the oil by injection of a fluid, which can be either (natural) gas or water. Another technique associated with secondary production is artificial lift. Artificial lift decreases the required pressure to let oil flow to the surface by ‘lifting’ the oil. Gas lift reduces the overall density in the wellbore and is commonly used. The recovery factor that can be achieved with primary and secondary recovery is roughly 35 – 45% (Tzimas et al., 2005).

Tertiary recovery methods often increase the mobility of the oil or decrease the mobility of the displacing fluid. They are referred to as ‘Enhanced Oil Recovery’, or EOR techniques. Increasing the mobility can be achieved by thermal methods, which reduce the viscosity of (heavy) oil e.g. by injecting steam. Novel technologies use surfactants to reduce the surface tension between water and oil in the reservoir. This allows displacement of oil which would otherwise be immovable. Supercritical carbon dioxide flooding has been proven a successful method for tertiary recovery as well. Tertiary methods have the potential to allow for another 5 – 15% of oil recovery, depending on the reservoir and oil type.

Combining technologies

Many innovations are not new by themselves, but manage to successfully combine existing technologies into a process that can be used for a new purpose. The combining of technologies has enabled us to operate in remote and harsh conditions, such as the Arctic or in deep oceans. Furthermore, new combinations of technologies are being used to maximize oil production. New methods for oil displacement are of vital importance to the industry, as even a few percent of extra recovery from every field in the world could imply months of even years’ worth of oil resources.

In this study, a combination of two techniques is being explored for their potential. One is the mechanism of foam injection, which has been studied extensively. The second technique is the addition of nanoparticles to foam in order to increase foam strength. A stronger or more viscous foam would imply a more efficient oil displacement. The findings in this report pave the road for the oil industry to increase their reservoir potential.

This remainder of the introduction discusses the concept of foam flooding, and briefly explains the effect of adding nanoparticles to foam. It also summarizes the current state of technology regarding this subject. Based on these state-of-art researches the aim of this thesis is introduced.

1.1 The mobility ratio

When displacing oil with a fluid, a more efficient displacement can be achieved when the mobility ratio is improved. The mobility ratio can be stated as (1):

$$M = \frac{k_{ri}}{k_{ro}} \Big/ \frac{\mu_o}{\mu_i} \qquad (1)$$

Where M is the mobility ratio, k_r the relative permeability and μ the viscosity of oil (o) of the injectant (i). The equation describes how mobile the injectant is compared to the fluid that has to be displaced, in this case oil. A mobility ratio above 1 will mean the injectant moves more freely through the reservoir than the oil does. This is the case when gas is injected into an oil reservoir. The mobility ratio can exceed 100, which is considered unfavourable. Equation (1) indicates the mobility ratio can be lowered by increasing the viscosity of the injectant, by decreasing the oil viscosity or by changing the relative permeability of the fluids.

The oil viscosity can be reduced by thermal methods for enhancing oil recovery. An increase in temperature will cause the oil viscosity go down more than the viscosity of the injectant does, resulting in a lower mobility ratio and therefore an improvement of the displacement.

The viscosity of the injectant is typically controlled by the type of injectant, gas or liquid, temperature and pressure. However, techniques have been developed that allow for viscosity manipulation. Examples include the addition of polymers to the injected liquid or the creation of a foam (Figure 1).

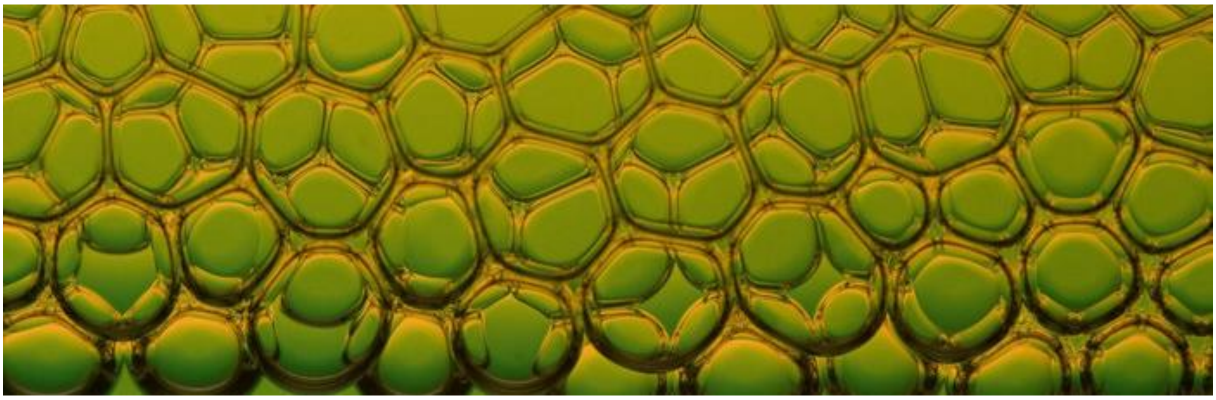

Figure 1: Photograph of a foam (source: ESA)

Foam consists of pockets of gas separated by a liquid film with the aid of a surfactant. The ‘apparent’ viscosity of foam is higher than of that of the individual components separately. In addition, the required gas is sometimes readily available from nearby gas fields containing nitrogen or carbon dioxide. This can potentially make it very easy to economically generate large quantities of foam.

Foam helps to overcome typical gas-injection issues in three ways; by reducing gravity override (Figure 2 A), reducing channelling (Figure 2 B) and reducing viscous fingering (Figure 2 C).

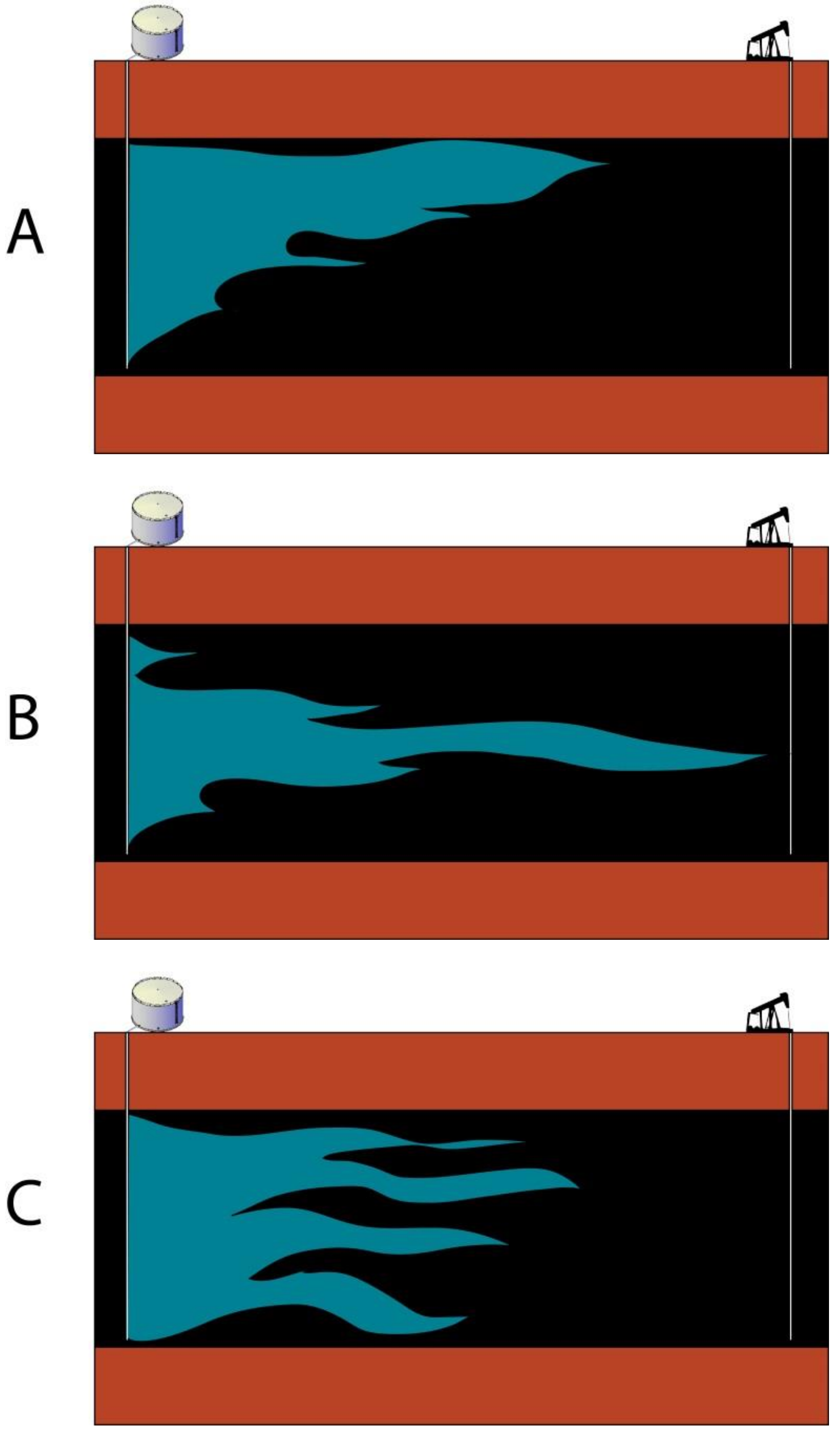

Figure 2: Effects of A) gravity override, B) channeling, C) viscous fingering

Gravity override occurs due to the density difference between gas and oil. Gas is lighter, so it tends to migrate upward due to buoyancy. Channelling can occur when gas finds a way through a high-permeable zone and breaks through from the injector to the producer. As soon as a breakthrough is established most of the injected gas will flow through the space which is occupied by gas, as this is the path of least resistance. This will greatly reduce efficiency. Lastly, viscous fingering occurs due to the viscosity difference between the injectant and oil. It can leave areas filled with oil unswept, which will cause it to be increasingly difficult to extract afterwards. By injecting foam instead of gas, these problems can be largely avoided.

Foam should remain in its dispersed state to overcome the above-mentioned problems. However, the difficulties in doing so have caused it to not be widely applied in the field yet. When flooding with foam in an oil-filled porous medium some complications arise. First of all, surfactant is lost due to adsorption to the rock formation. Secondly, surfactant is partitioned to the oil. A surfactant loss will case decreased foamability and decreased foam viscosity. In addition, foam-oil interfaces are very unstable and will result in lamella destruction. The elevated temperature will cause many foaming agents to work less efficiently. The mechanics behind these foam complications are explained in the theoretical sections of this study.

1.2 Nanoparticles

The stability of foam at reservoir conditions is the key for successful foam flooding. In some non-petroleum industries, nanoparticles are used to enhance foam stability (Green et al., 2013). Products for personal care and hygiene, and many products in the food industry are already making extensive use of nanoparticles to stabilize their foaming products. The Journal of Petroleum Technology noticed an increase in attention from the industry for nanoparticle-enhanced foam. This section provides a brief overview of recent studies on this topic.

1.2.1 Nanoparticle-Stabilized Supercritical CO_2 Foams for Potential Mobility Control Applications

(Espinosa, Caldelas, Johnston, Bryant, & Huh, 2010)

In this study the authors generated a supercritical CO_2-in-water foam that was stabilized with surface-treated nanoparticles. The nanoparticles were 5nm silica nanospheres with two different surface coatings. One coating made the particle hydrophilic, the other salt tolerant. They used deionized water to generate stable foams at nanoparticle concentrations of 0,05 wt% (0,5 g/L), and found that higher salinities required an increased nanoparticle concentration. They did not use a surfactant to aid in foam generation. They observed that adding nanoparticles to the mixture increased the resistance to flow (apparent viscosity) by two to eighteen times when compared to a situation without nanoparticles. They were unsuccessful in their attempt to use a special coating to generate salt-resistant nanoparticles, but they did successfully generate stable foams at elevated temperatures (up to 95˚C) with the usage of nanoparticles only.

1.2.2 Generation of Nanoparticle-Stabilized Supercritical CO_2 Foams

(J Yu, Liu, Li, & Lee, 2012)

This study was focussed on using CO_2 foams for CO_2 storage purposes, a field which faces similar challenges as EOR does. Effects of particle concentration, brine salinity, pressure, temperature and surfactant were assessed on their ability to generate foam. The particle was a nanosilica approximately 100 – 150 nm in diameter. They only observed foamability in a static column, rather than core-flooding or other experiments with any kind of flow. When the temperature was increased from ambient (25˚C) to 60 ˚C, no foam generation was observed with only nanoprticles. Their explanation for this effect was that the high temperature caused an elevated interfacial tension, and the high temperature also caused increased mobility of the nanoparticles, prohibiting them from adsorbing on the CO_2 – water interface.

A notable finding is that they were able to generate CO_2 foam with surfactant and nanoparticles, whereas previously they were not able to create foam with the same concentration of the same surfactant *without* nanoparticles. Their explanation for this observation was that the surfactant had adsorbed on the particle surface. Therefore the electrostatic interaction between the particles and the surfactant heads resulted in a monolayer adsorption of the surfactant at the particle surface, which transformed the particle from hydrophilic to partially hydrophobic. The particles became surface active and were able to stabilize the bubbles. The effect where additional surfactant added to a nanoparticle dispersion could cause the particles to aggregate because of the surfactant charge neutralizing the nanoparticle electrostatic repulsion was also identified. All of the above are theories also described in this thesis.

1.2.3 Stabilizing Nano Particle Dispersions in High Salinity, High Temperature Downhole Environments

(Mcelfresh, Wood, & Ector, 2012)

In order to successfully generate a nanoparticle-enhanced foam at reservoir conditions, the nanoparticle dispersion needs to be stable at reservoir conditions. Mcelfresh et al. (2012) found the zeta potential to be most directly correlated to dispersion stability. They identified the detrimental effects pH and surface modifications such as ion adsorption can have on the dispersion stability by significant reduction of the zeta potential. Therefore, they concluded that the suspension must be tolerant to high salinity and temperature environments.

1.2.4 The Application of Nanoparticle-Stabilized CO_2 Foam for Oil Recovery

(Jianjia Yu, Mo, Liu, & Lee, 2013)

This study investigated the effects of silica nanoparticles of 17 – 20 nm on supercritical CO_2 foam in both static column tests and core flow experiments at a pressure of 1200 psi and 20˚C. The foam flooding followed the waterflooding in a sandstone core. They reported better performance from the enhanced foam for sandstone cores with a lower permeability. From a practical point of view, they reported that their nanoparticles did not cause any pore clogging as the core permeability remained unchanged after performing the experiments. In the static experiments nanoparticles without surfactant were enough to generate foam. They observed no change in interfacial tension when nanoparticles were used in combination with surfactant, but they did recognize the effect where the adsorption of nanoparticles at the interface can decrease the contact area between the gas and liquid (brine), and henceforth help with stabilization.

1.2.5 Conditions for Generating Nanoparticle-Stablized CO_2 foams in Fracture and Matrix Flow

(Aroonsri et al., 2013)

This study investigated a variety of silica 5nm nanoparticles with different surface coatings. They found the hydrophilic-CO_2-philic balance (HCB) to be very important when designing a nanoparticle that could generate a stable foam. They identified shear rates for which foam could be generated in-situ with the use of nanoparticles. Above a certain share rate, nanoparticle foam apparent viscosity increases drastically. They identified the importance of a suitable coating in order to achieve the right HCB in order for the particles to adsorb on the interface.

An interesting observation is how an increase in salinity could cause some nanoparticles radically change behaviour. A suspension in seawater salinity did not generate a stable foam. This is due to the salinity increase causing the nanoparticles to behave more hydrophobically, lowering the HCB and bringing the contact angle closer to 90˚. As can be read in the section Coalescence prevention in this thesis, this causes the adsorption energy to increase which on its turn causes more stable foam bubbles. They indicate that a salinity increase can also cause the foam to be more viscous, but the addition of too much surfactant causes the nanoparticle dispersion to lose stability. Therefore, salinity control is a very important parameter to control during the formation of foams. A second observation that stands out is that they were not able to generate a nanoparticle foam if the foam quality was above 0.95 or below 0.5.

1.2.6 Study of particle Structure and Hydrophobicity Effects on the Flow Behaviour of Nanoparticle Stabilized CO_2 Foam in Porous Media

(Jianjia Yu, Wang, Liu, & Lee, 2014)

This paper subjects three types of silica nanoparticles to an investigation on the effects of particle structure and wettability on supercritical CO_2 foam generation. They used two types of amorphous silica nanopowders with different surface properties, and a crystalline nanoparticle. The amorphous nanoparticles had a size of ~10nm, while the crystalline particle was approximately 70nm in size. Crystalline silica and amorphous silica showed similar behavior. Wettability of nanoparticles was found to be the most significant parameter that controlled supercritical CO_2 foam generation and stabilization, with the most hydrophobic silica nanoparticles exhibiting the most noticeable effect on CO_2 foam mobility reduction. In addition increased hydrophobicity caused a decrease in bubble size.

1.2.7 Synergistic stabilization of foams by a mixture of nanoparticles and surfactants

(Singh & Mohanty, 2014)

This study shows that the half-life of foam can increase drastically when more nanoparticles are added. Furthermore it confirms the theory that nanoparticles trapped at the plateau border increase stability by reducing liquid drainage through those plateaus. Not only did half-life time increase by increasing the nanoparticle fraction, the mobility reduction factor also increases by adding more nanoparticles according to this study.

1.2.8 Study nanoparticle-stabilized CO2 foam for oil recovery at different pressure, temperature and rock samples

(Mo, Jia, Yu, Liu, & Lee, 2014)

This study shows that pressure can be an important factor in oil recovery by nanoparticle CO_2 foams. The effect of temperature was investigated, and it was found that increasing the temperature can have a destabilizing effect on foam stability due to the nanoparticles adsorbing less easily on the bubble interface because of their increased mobility. In addition, this study took limestone and dolomite into account. It shows that the permeability of their dolomite sample went from 295 mD to 110 mD as a result of particle plugging (particle size is 5 nm) when experiments with oil were performed.

They do not describe their expectations on the results for carbonate core-flooding, or compare nanoparticle foam with surfactant foam in carbonate cores. Nanoparticle foam might have an edge over surfactant foam in this scenario. As has been described, foam travelling through a porous medium is a continuous process of lamellae destruction and generation. In sandstone reservoirs, the irregular shape of the pore space provides ample opportunities for foam to be generated. In carbonate however, the pore space is much smoother. Therefore, there are less points where foam can be generated and therefore foamability is much less. Nanoparticles, especially when combined with surfactant, might provide these irregularities that are beneficial for foam generation. Therefore it can be valuable to compare nanoparticle and non-nanoparticle foam for a carbonate reservoir, but as stated that has not been done in this study.

1.2.9 Nanoparticle stabilized CO2 in water foam for mobility control in enhanced oil recovery via microfluidic method

(Nguyen, Fadaei, & Sinton, 2014)

The nanoparticle utilized in this study is a silica nanoparticle with a 50% dichlorodimethyl silane surface coating. They found that this nanoparticle alone can be more effective for the generation of a stable foam than a SDS surfactant. Coalescence was prevalent in SDS foam, but almost no coalescence was visible in the nanoparticle foam. This agrees with the theory presented in this thesis that adsorption of nanoparticles at the vapour – liquid interface makes it very resistant against coalescence because of the high energy required to remove the nanoparticle from the interface.

1.2.10 Synergistic Stabilization of Foams by a Mixture of Nanoparticles and Surfactants

(Singh & Mohanty, 2014)

The authors of this paper recognized the potential of nanoparticles to enhance foam. In this study, the synergistic effect of nanoparticles and surfactant were investigated. Their theoretical overview gives an indication of the different mechanisms through which nanoparticles enhance foam. The nanoparticle used in this study is made of a surface-coated silica, with a mean diameter of 20 nm. The surfactant was Bioterge AS-40 in pure water, and the gaseous phase was nitrogen. They observed an increasing half-life time of foam in bulk mode with increasing nanoparticle concentration. The authors also observed multiple effects which retard bubble coalescence and liquid drainage. Most importantly, the core-flooding experiments performed by them showed an increase in mobility reduction factor of nanoparticle-enhanced foam.

1.3 Literature summary

In the discussed literature CO_2 was the primary focus. Experiments on N_2 foams were performed only by Singh & Mohanty. This can be expected because CO_2 flooding is a more widely applied type of EOR. Regardless, this points out a hiatus on N_2 foam knowledge.

Most of the studies weighed nanoparticle foams versus surfactant foams, rather than exploring the opportunities to combine both to create an enhanced foam. The benefits that could be obtained by adding nanoparticles instead of more surfactant has not received much attention either. Again, only Singh & Mohanty studied the synergistic capabilities.

The particles investigated in the presented studies are not suitable candidates for field-scale applications. Firstly, the particle sizes used in most studies are relatively small, with most studies using sub 50 nm sizes. Using small particles has both advantages and disadvantages. Amongst the benefits of using small particles are reduced filtration and improved physical behaviour. However small particles are more costly. Small nanoparticles are suitable to prove the working principle behind them. In order to find an optimal economic solution larger particles should also be considered, which is not done in the presented studies.

Secondly, most particles use a surface-coating to enhance or change their surface properties. Again, surface-treating a large quantity of nanoparticles for a field-scale application would be very costly. Because of above-mentioned reasons the nanoparticles studied so far would not be practical nor economical. Therefore they can likely not be implemented as an economical field-scale solution.

There is no data available on non-surface coated nanoparticle behaviour in collaboration with surfactant. Additionally, the data available on high temperature and high pressure experiments is very limited. Because this would mimic reservoir conditions and potentially alters surfactant behaviour, it would be valuable to gain knowledge of nanoparticle behaviour at those conditions.

1.4 Thesis objectives

Recent studies at the Delft University of Technology tested a new type of nanoparticle in collaboration with Shell Global Solutions that can be produced economically. The cost of large-scale production of these particles are low compared to alternatives. Their size is approximately 150 nm, and no additional surface coatings are used. Therefore this can potentially be the nanoparticle solution that will allow foam to be more widely applied.

The primary aim of this thesis is to obtain knowledge on the performance of these nano particles when used together with a surfactant. Both sandstone and carbonate cores should be subjected to experimental research, as carbonate is known to be challenging to successfully flood with foam.

By comparing experiments with and without nanoparticles, insight is obtained on the enhancements that can be obtained by using them. A reliable method to conduct experiments and avoid drawbacks of using these nanoparticles should be developed.

2 Foam

Foam consists of pockets of gas separated by liquid films. It is an example of a dispersed medium, which is a substance consisting of at least two immiscible fluids (Simjoo, 2012), stabilized by a surfactant. This chapter focusses on foam. First foam physics and the parameters influencing foam behaviour will be described. Afterwards it discusses the behaviour of foam in porous media.

2.1 Bulk foam behaviour

The term ‘bulk’ foam is used when the foam confinement is larger than the size of the bubbles (Schramm, 2005), an example is displayed in Figure 3.

Figure 3: Foam in 'bulk' (source: comacgroup)

A further division can be made by distinguishing between ball foam, which consists of separated spherical bubbles, and polyhedral foam (Figure 4). Mainly the latter is of interest in this study, as the behaviour of lamellae in polyhedral foam can be compared to their behaviour in porous media.

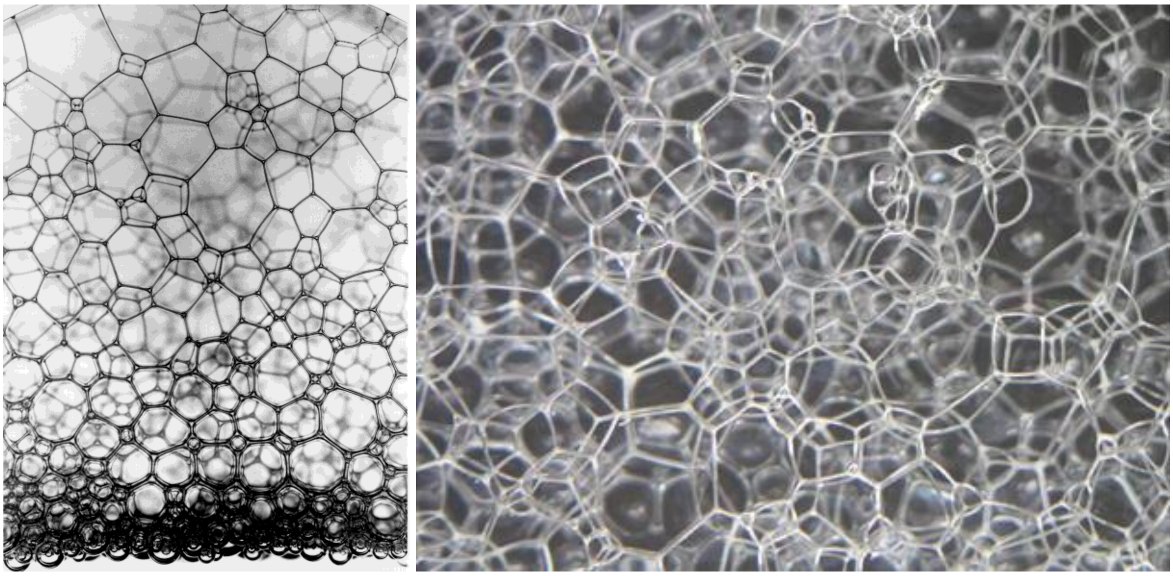

Figure 4: Examples of polyhedral foam (source: physics.ucla.edu)

2.1.1 General foam parameters

A number of parameters are closely related to foam behaviour and will be used throughout this thesis. This section will briefly explain them.

2.1.1.1 Quality

Foam quality is described as the volume fraction of gas:

$$f_g = \frac{V_g}{V_l + V_g} \tag{2}$$

where f_g [-] is the foam quality, and V_g [m^3] and V_l [m^3] the volume of gas and liquid respectively.

2.1.1.2 Texture

The amount of lamellae per unit volume is commonly referred to as foam texture or bubble density. Foam lamellae reduce the mobility of gas, and therefore more lamellae typically means a greater reduction of the gas mobility. There is no practical way to directly determine the amount of lamellae per unit volume. The only experimental method is a straightforward counting of the bubbles, which near impossible for a non-opaque porous medium.

More lamellae reduce the mobility of the gas to a greater extent. Therefore, the reduction of gas mobility can give an impression of the amount of lamellae, or foam texture. By conducting core-flooding experiments as described in this study an impression of the gas mobility reduction is obtained, and an impression of foam texture is obtained.

2.1.1.3 Stability

One of the major goals of this study is to enhance foam stability. Therefore, stability is a term that will be used throughout this thesis. Stability of the foam describes how the foam structure (films and channels) remains stable over time. Inversely, unstable foam describes foam in which the films or bubbles have collapsed. Stability can be quantified as the time required for half the foam volume to collapse or coalesce. The mechanisms governing foam stability have to be studied to obtain insight in how foam stability can be manipulated, which is done in this chapter. Schramm (2005) described three methods in order to test foam stability:

- Measure the lifetime of a single bubble
- Measure steady-state foam volume under given gas flow
- Measure the rate of collapse of a static foam column

These methods are very intuitive, and provide results that are easy to interpret. However, they do not apply specifically for foam in a porous medium. Foam flow in a porous medium is a continuous process of foam destruction and generation. The balance between these two determines how stable foam in a porous medium is. Foam will appear stable if there are many lamellae, implying a high bubble density. This means there needs to be little lamellae destruction (Goodwin, 2009). As described previously, an impression of the bubble density can be obtained through the conduction of core-flooding experiments.

The stability of foam in a porous medium depends on many parameters such as foam quality, pH, temperature, salinity and concentration and type of surfactant, which will be explained in this chapter.

2.1.2 Surfactants

Foam stability is not a topic that is relevant only in the oil and gas industry, but also in everyday life such as personal care and food industries. Many foams such as shampoo or shaving cream maintain structure over an extended period of time. This is made possible by the addition of a surface-active agent or 'surfactant'.

Most surfactants are amphiphilic, which means they have a hydrophilic and hydrophobic part. Because a part of the molecule is attracted to water and a part is repulsed from water, they adsorb very well on the surface, or interface, between those two phases. Surfactant molecules typically obtains the amphiphilic behaviour by having a head and a tail. The tail is often a linear, aromatic or branched hydrocarbon chain, which explains why it is soluble in oil. Most surfactants have either one or two tails. The head is usually a group which is soluble in water. The head groups can vary greatly between different surfactants, which will be explained later. A useful classification can be made based on the electric charge of the hydrophilic head group. Non-ionic surfactants have no charged groups, anionic and cationic surfactants have negatively and positively charged groups respectively, and amphoteric surfactants have both. As will become clear later in this thesis, the charge of the hydrophilic head group can have great effects on surfactant related behaviour.

Figure 5 shows adsorbed surfactant molecules on a water-oil interface. The yellow hydrocarbon tails are dissolved in the oil droplet, while the hydrophilic heads are dissolved in water.

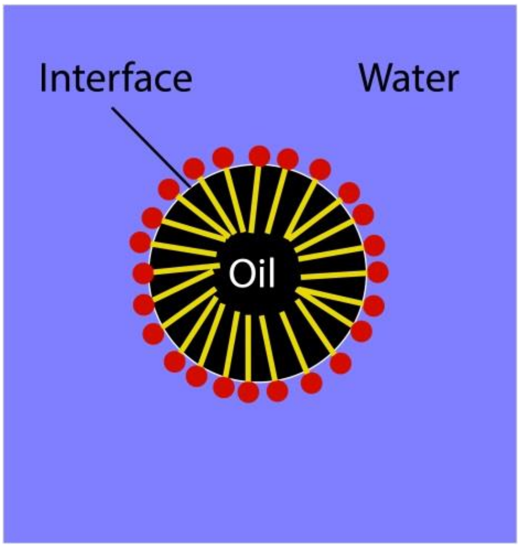

Figure 5: oil droplet in water, surfactant molecules adsorbed on the oil-water interface (not to scale)

Surfactants help in foam generation because they reduce the surface tension between two phases. Surface tension is a measure for how difficult it is to extend the surface area of a fluid (Goodwin, 2009). A high surface tension will mean a large requirement of energy to increase the surface area. It is energetically favourable to have a low interfacial area between two phases. Because foam has a very high surface area, it is naturally unstable. By merging bubbles the surface free energy is reduced. This is a process called coalescence and occurs spontaneously for foams. Another parameter that influences the rate at which coalescence occurs is the interfacial tension (IFT). A lower IFT means a lower Gibbs free energy, and therefore lower driving force for coalescence. A reduction in IFT is achieved by surfactants, because it is energetically favourable for their molecules to be adsorbed at the interface (Spencer & Heuberger, 2009).

A useful surfactant-classification can be made by the composition of the hydrophilic head group based on their electrostatic charge. Non-ionic surfactants have no charge groups, anionic and cationic surfactants have negatively and positively charged groups respectively. Amphoteric surfactants have both.

The Gibbs adsorption isotherm for multicomponent systems (equation (3)) relates changes in concentration of a surfactant with changes in surface tension.

$$\begin{aligned} -d\sigma &= \Gamma_1 d\mu_1 + \Gamma_2 d\mu_2 + \ldots \\ -d\sigma &= \sum_i \Gamma_i d\mu_i \end{aligned} \tag{3}$$

In which σ is the surface tension, Γ_i is the surface excess of component i and μ_i is the chemical potential of component i. The surface excess is a representation of the difference between the total moles of component i in the system and the amount of moles of component i in a particular phase (Goodwin, 2009).

2.1.2.1 Critical Micelle Concentration

An important characteristic of a surfactant is the critical micelle concentration, or CMC. The CMC is the maximum solubility of the surfactant monomer in a solvent. It is a very important parameter for all industries using surfactants. Below the CMC value, ionic surfactants behave like an electrolyte. They will dissolve and have an effect on the electrolytic properties of the solvent such as electric conductivity and electromotive force. Above CMC these properties change dramatically, indicating cooperative association processes taking place. This process is also referred to as the formation of 'micelles' (Schramm, 2005), which is driven by the hydrophobicity of the hydrocarbon surfactant tails. At CMC, these micelles start to form and additional surfactant added to the solvent agglomerates in these micelles. This is shown in Figure 6.

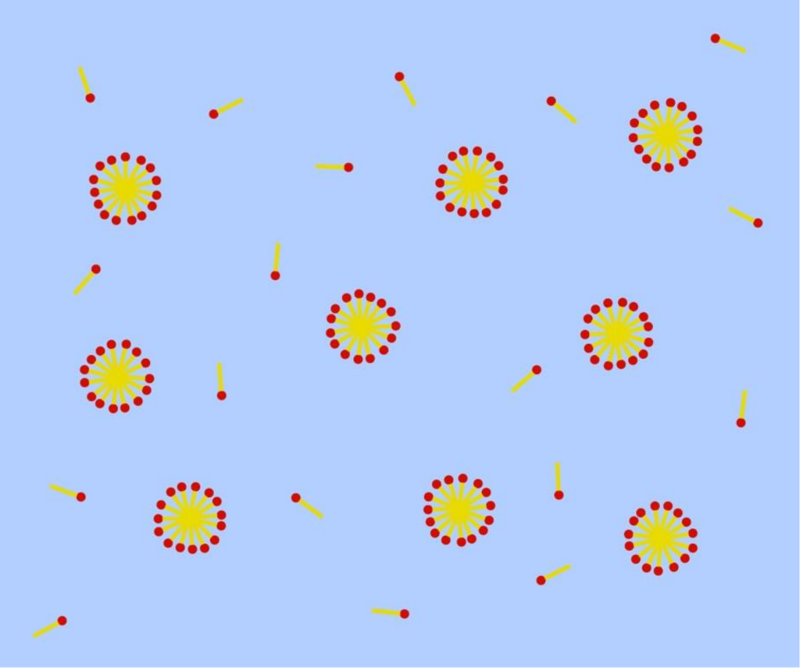

Figure 6: Surfactant micelles in a liquid: the hydrophilic heads are dissolved in water while the hydrophobic tails form a cluster.

The hydrophobic surfactant tails can no longer escape the water by adsorption at the interface, hence they will agglomerate together with the heads pointing outward and in contact with the water where they can dissolve. The transition from additional molecules being able to adsorb at the interface, to additional molecules solely being used to create more micelles, is sudden. Above this concentration newly added molecules will be used to create more micelles and the surface tension is almost independent of surfactant concentration.

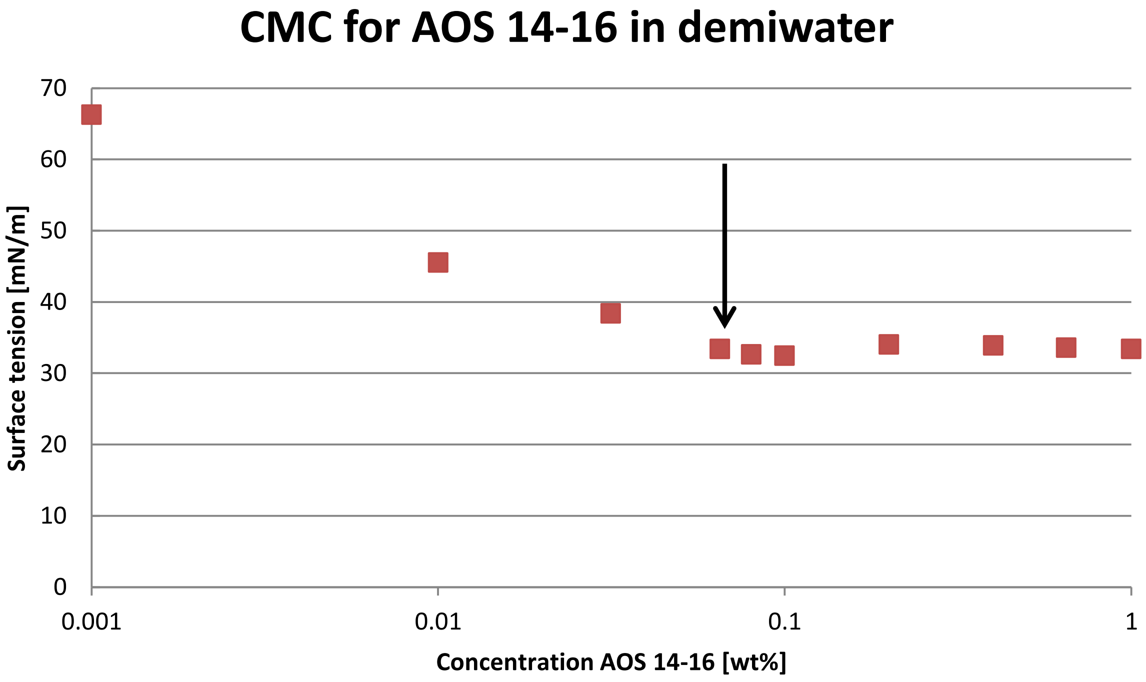

Figure 7: CMC for Bioterge AS-40 (AOS 14-16) in demineralized water, arrow indicates CMC at 0,08 wt%

Figure 7 shows an example of the transition from below to above CMC. When the surface tension is plotted versus the logarithm of the surfactant concentration, CMC can be found at the intersection between the line with negative slope and horizontal line. In this figure CMC is determined from AOS 14-16 in demineralized water. It's value appears to be at a concentration of 0,08 weight percent.

The state of the film can be mathematically described by the Gibbs adsorption isotherm equation (3) and the Gibbs-Duhem equation, equation (4):

$$dp = \sum_i c_i \, d\mu_i \tag{4}$$

In which p is the pressure, c is the bulk-phase concentration of component i, and μ the chemical potential. Both equations together describe a film but are not able to quantify quantities such as film thickness or disjoining pressure as the Gibbs adsorption isotherm characterizes only a single interface (Rusanov & Krotov, 2003). Both equations can be re-written to obtain the fundamental equation for a thin film, equation (5):

$$d\sigma = -2\Gamma_1 d\mu_1 + hd\Pi_d \tag{5}$$

In which h is the lamella thickness, and Π_d the disjoining pressure which is the pressure difference between the gas and liquid phase for a stable lamella.

2.1.3 Disjoining pressure

The disjoining pressure is a measure for the stability of a lamella, which can be enhanced by ionic surfactants. A lamella consists of two vapour-liquid interfaces, between which interaction forces occur. These interactions show many similarities to interaction between particles, which the next chapter on nanoparticle behaviour will discuss. The relevant forces include attractive forces such as van der Waals forces, and repulsive forces such as electrostatic repulsion, which all contribute to the total Gibbs energy of the interacting surfaces.

When the disjoining pressure is positive this indicates a repulsive force, while a negative disjoining pressure indicates an attractive force. Figure 8 gives a schematic drawing for the disjoining pressure as a function of its main contributors, the van der Waals attraction, the electrostatic repulsion and steric repulsion forces.

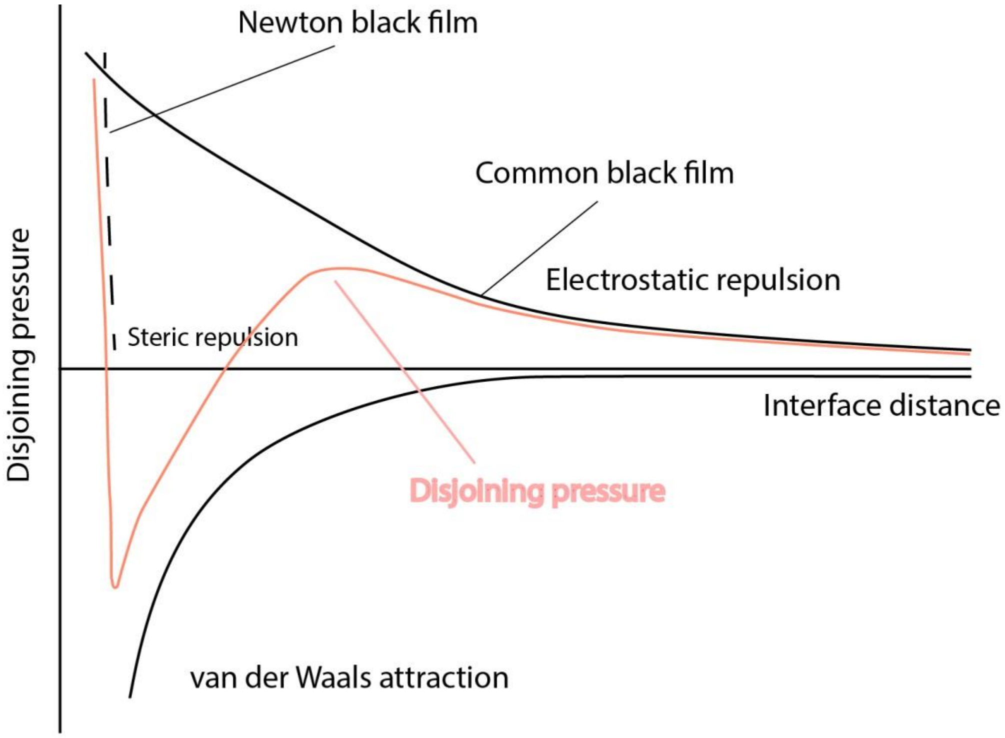

Figure 8: sketch of disjoining pressure as function of its main contributors (adapted from: (Stubenrauch & Klitzing, 2003)**)**

The characteristics of surfactants play a big role in making the interfaces react with each other in the way they do as given in Figure 8. Figure 9 illustrates some of these interactions.

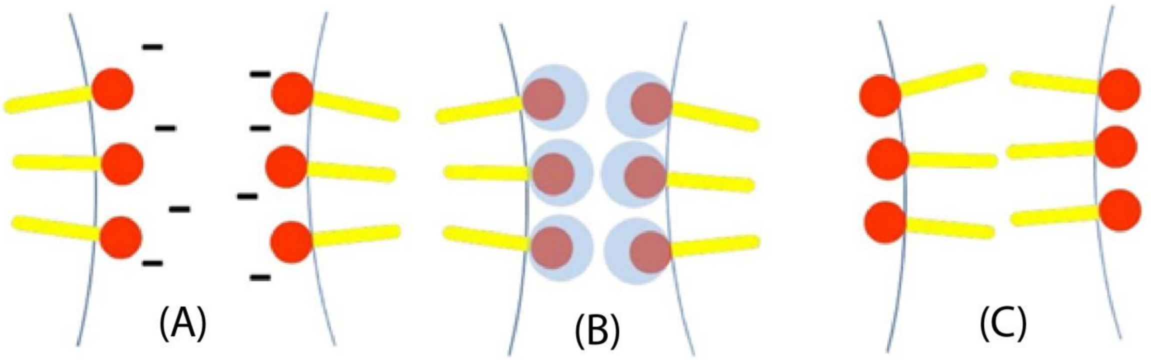

Figure 9: interaction between surfactant molecules adsorbed at thin liquid film interfaces. A) shows the effect of electrostatic stabilization, B) shows hydration stabilization and C) shows steric stabilization (adapted from: (Spencer & Heuberger, 2009)**)**

From observing the figures it becomes clear that the disjoining pressure will only play an influential role for small distances between the interfaces, as the interfaces do not experience as much interaction for thick films. Hence, the disjoining pressure approaches zero for thick films. Because there are no strong repulsive forces for thick films, film thinning can occur. In a foam the pressure in the gas phase is higher than the pressure in the liquid phase (the lamella) which causes capillary suction (Stubenrauch & Klitzing, 2003). The pressure difference is also called the capillary pressure and shown in equation (6).

$$\Delta P = P_c = \frac{2\sigma}{r} \tag{6}$$

Where P_c is the capillary pressure, σ the interfacial tension and r the radius of the plateau border.

If it was not for the repulsive forces from Figure 9 that increase in magnitude when the distance between the interfaces decrease, the lamellae would completely drain because of attractive forces. In reality capillary drainage is eventually prevented when the disjoining pressure is large enough to overcome them.

This knowledge can now be applied to determine areas where the liquid film is stable. In the region where Π_d decreases with decreasing thickness, the films will drain because of decreasing repulsion. This process continues until either Π_d increases again, or until the film ruptures. The area where this is the case separates the graph in two stability zones. One is called the region of the Common Black Film (CBF), and the other the zone of the Newton Black Film (NBF).

The repulsive forces that stabilize the CBF and NBF are different. The NBF is stabilized by entropic confinement forces such as steric repulsion. This repulsive force increases quickly for films draining smaller than a certain size. The stability range of the NBF is therefore small. The CBF is stabilized by electrostatic repulsion. (Freedman, Zhang, & Zhong, 2009)

Summarizing, the disjoining pressure is the pressure that prevents the two interfaces lamella from merging. If it is too small the lamellae either break or thin until depleted. This section also described how surfactants aid in the generation of dispersions, and how they can increase the disjoining pressure based on their interaction.

2.2 Foam in porous media

Unlike ‘bulk’ foam, foam flowing through a porous medium experiences a very dynamic process. On a macroscopic scale foam in porous media seems comparable to ‘bulk’ foam with characteristics such as a viscosity which depends on many parameters. On a microscopic level it becomes clear that there are large differences. In static foam, foam lamellae experience the effects of all kinds of interactions. When foam is flowing through a porous medium the lamellae are forced through narrow openings and large voids, but are also subjected to contact with oil. All these processes cause a lot of stress on the lamellae, which will often rupture as a result. Though, most reservoir rocks offer ample opportunities for foam to be regenerated.

2.2.1 Foam generation

Foam generation in porous media is very complex. There is no lack in theories on how foam is being generated, but the successful implementation of all these models into a single model on which all foam experts can agree has proven to be challenging. The modelling of foam flow through a porous medium is not within the scope of this thesis; however, the theories presented below discuss foam generation in a conceptual way, rather than preparing them for model implementation. In general, there are three underlying mechanisms for foam generation, which are leave-behind, capillary snap-off, and lamella division (Chen, Yortsos, California, & Rossen, 2004; Tanzil, Hirasaki, & Miller, 2002). Weak foam can be generated by the process called leave-behind, which occurs when gas fingers enter neighbouring liquid-filled pores. Capillary snap-off and lamella division generally create much stronger foams.

Lamellae being generated through leave-behind are created when gas enters liquid-filled pores. They are essentially thin liquid films that remain after gas has swept neighbouring pores, and therefore have a direction parallel to gas flow. This implies that they do not make the gas discontinuous. In other words, the lamellae this mechanism provides does not help to reduce gas mobility. It is regarded to as weak foam.

Snap-off occurs when gas enters a pore filled with a wetting liquid. It is a mechanism that is dependent on the pressures in the pore. The walls of the pore are wet by the surfactant solution. If the mean curvature of the gas-liquid interface in the constriction is greater than that in the rest of the capillary, the capillary pressure in the pore neck is higher than anywhere else. If the pressure gradient in the gas phase is negligible, this means that the liquid-phase pressure is lower in the neck than in the rest of the capillary. Consequently, liquid flows into the constriction and accumulates there in a collar. This collar can grow, become unstable, and bridge across which creates a lamella (Falls et al., 1988)

Lamella division is a process that occurs when the pressure gradient is large enough to mobilize the lamellae. In other words, it occurs when foam is moving through the porous medium. A new lamella might be generated when an existing lamella encounters a split in the flow path. In such a scenario the lamella might split itself and continue as two separate lamellae, one for each branch. The schematics of the foam generating processes can be found in Figure 10.

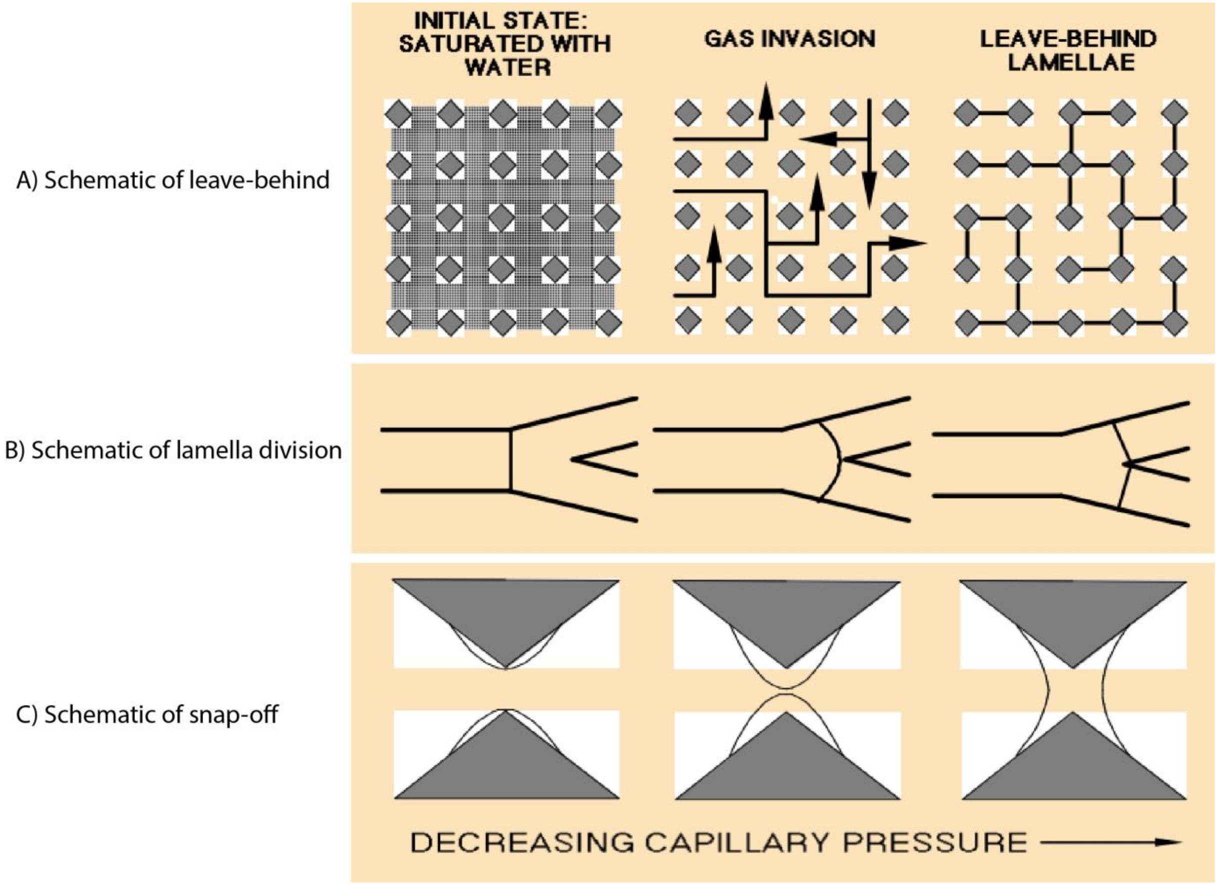

Figure 10: schematic drawing of foam generation processes. A) depicts leave-behind, B) depicts division and C) lamella snap-off, adapted from (Snap-Off and Foam Generation in Porous Media by W.R. Rossen, n.d.)

2.2.2 Foam destruction

The primary mechanism for foam destruction is destruction due to capillary suction, which is a function of wetting liquid saturation, permeability, wettability and surface tension among other parameters. The amount of capillary suction which causes the lamellae to rupture is called the critical or limiting capillary pressure. When this point is reached no foam bubbles can be sustained. In practice, the transition from foam to no-foam for a certain capillary pressure is very abrupt (Khatib, Hirasaki, & Falls, 1988). Because foam strength depends on the texture, which is governed by the capillary pressure, a sudden change in gas mobility will be noticeable around the limiting capillary pressure. As the capillary suction depends on wetting liquid saturation, there is a water saturation corresponding to the critical capillary pressure, called the critical water saturation (Freedman et al., 2009).This will be used in the modelling part of this thesis.

Secondly, foam destruction is dependent on the surfactant concentration (Simjoo, 2012). Bubble coalescence due to poor foaming can be expected for surfactant concentrations below CMC. For surfactant concentrations above CMC the bubble-coalescence rate appears to be very small. While initially the surfactant concentration can be above CMC, adsorption on the reservoir surface might cause the surfactant concentration to drop along with the in-situ travelled distance.

Tertiary mechanisms for foam destruction are destruction due to bridging of the lamellae by a hydrophobic particle, and foam rupture due to movement over a hydrophobic surface such as oil. When a liquid films comes into contact with a hydrophobic substance, the contact angle from the liquid on that surface changes. Eventually this might lead to a rupture of the film.

2.3 Modelling foam flow

The dynamics of foam in a porous medium are not yet fully understood. There is no universal theory that can explain all different facets of foam behaviour. Basically there are three different approaches to foam flow modelling, each of which has their own inherent strengths and weaknesses:

- Mechanistic or population-balance models
- Semi-empirical models
- Empirical models

The mechanistic approach tracks the bubble density. The bubble population-balance and percolation theory fall within the mechanistic approaches. The bubbles can be generated by any of the mechanisms explained above. However, in the population-balance models so far only snap-off has been considered. Results that are obtained with a (semi) empirical method are deducted from observations and therefore inherently reliable, but because of this empirical nature the results are often obtained by fitting parameters and not actual scientific relationships. Even though there is no general agreement on the best method, there are some key factors all models require which have been identified (Kovscek, 1998).

- The presence of foam reduces gas mobility
- Foam behaves like a non-Newtonian fluid
- Surfactant concentration, salinity, temperature and wettability influence foam characteristics
- Adsorption, partitioning and surfactant transport should be adequately described

This chapter will first provide a brief overview of the different foam modelling approaches. Afterwards a method to analyse foam core-flooding experiments will be discussed.

2.3.1 Mechanistic or population-balance models

As has been described previously, foam texture is of major influence on the gas mobility reduction factor (MRF) and therefore pressure gradient. Predicting the texture, otherwise known as bubble population, is done in mechanistic or population-balance models. Moving lamellae in porous media have a limited lifetime, as continuous stretching as well as many other mechanics causes the lamellae to break. Multiple processes also cause new lamellae to be continuously generated. Population-balance models describe these processes of generation, destruction, displacement and agglomeration of lamellae through balance conservation differential equations (Falls et al., 1988). The population balance is given in equation (7):

$$\frac{\partial}{\partial t}\left[\phi\left(S_f n_f + S_t n_t\right)\right] + \nabla\left(u_f n_f\right) = q_f \tag{7}$$

Where S_f and S_t are flowing and trapped gas saturation, n_f and n_t represent the number density of flowing and trapped bubbles and q_f is the net rate of bubble generation (Falls et al., 1988; Lotfollahi et al., 2014). This model can be simplified by assuming local equilibrium or steady-state. In this case $q_f = 0$.

Percolation Theory

When simulating flow in a reservoir, the field is often divided in 'blocks'. These blocks get a value assigned for its properties that influence fluid flow, such as permeability and porosity. This way a simulation is carried out with averaged values over several hundreds of cubic meter reservoir volume. However, there is also the possibility to simulate on the much smaller-scale network of pore volumes and throats of the porous medium. In order to achieve this all pore volumes and other small-scale elements of a porous medium need to be randomly connected to each other. The statistics of all these interconnected elements can provide information about the rate-limiting conductance of larger-scale systems (Hunt, 2001).In this theory, a reservoir volume is represented by a network of pores that are interconnected by capillary tubes. The amount of connections (tubes) a pore has to its neighbouring pores determines the system behaviour. How this works in detail is described in (Gauglitz & Rossen, 1990).

2.3.2 Empirical or local-equilibrium models

Empirical or local-equilibrium models do not explicitly calculate foam texture. Instead, they obtain he effect of texture implicitly through reducing gas mobility as a function of surfactant concentration, phase saturations and other factors.

The mobility of foam in terms of relative permeability and viscosity is displayed in equation (8).

$$\lambda_f = \frac{kk_{rf}}{\mu_f} \tag{8}$$

Empirical models adjust gas viscosity or mobility in presence of foam, similar to mechanistic models. An example of increasing gas viscosity has been developed by (Ramirez, Marfoe, & Kazemi, 1987):

$$\mu_f = \mu_g \left[1 + 0.01 C_s \left(S_w - S_{wr}\right) f\left(v_g\right)\right] \tag{9}$$

Where C_s represents the surfactant concentration and v_g is the gas-phase velocity. The constant 0.01 used in this equation is an estimation for the increase in effective gas viscosity. The current value will yield an approximate five to tenfold viscosity increase, but it can be adjusted if a greater viscosity increase is anticipated.

Another technique in modelling the effects of foam is by reduction of gas mobility. This is typically done by introduction of a 'Mobility Reduction Factor' or MRF. Especially in steady state experiments this has proven to be a useful method. There are two ways to define the MRF:

$$MRF = \frac{\Delta P_{with\ \ foam}}{\Delta P_{without\ \ foam}} \tag{10}$$

$$MRF = \frac{\Delta P_{with\ \ foam} - \Delta P_{without\ \ foam}}{\Delta P_{without\ \ foam}} \tag{11}$$

For strong foams both definitions can be used interchangeably as the pressure drop with foam is much larger than the pressure drop without foam. A higher MRF implies a stronger and a more finely textured foam. The MRF is introduced in simulators by using them to correct for gas permeability in case of foam, as displayed in equation (12):

$$k_{rf}\left(S_g\right)=\frac{k_{rg}\left(S_g\right)}{1+MRF} \tag{12}$$

2.3.3 Semi-empirical methods

Besides a purely mechanistic or empirical approach, there are also hybrid approaches known as semi-empirical methods. These are based on mechanistic descriptions, but apply simplifications in order to obtain fractional flow curves in the presence of foam. These simplifications include one-dimensional displacement, Newtonian viscosity, no viscous fingering, no capillary-pressure gradients, negligible gravitational impact, no physical dispersion, incompressible phases and immediate attainment of local steady states (Freedman et al., 2009). The effect foam will have on the gas mobility will be expressed through the use of the MRF (Dholkawala, Sarma, & Kam, 2007).

It has been shown that (semi-)empirical models have an edge over population balance models when considering their user friendliness (Boeije & Rossen, 2013). While they provide this user friendliness they also take mechanistic concepts into account rather than solely rely on empirical correlations. In addition, less computations need to be made, less parameters need to be considered, and fewer numerical issues are encountered. Therefore, (semi-)empirical models are often used to simulate foam processes.

Next an approach to model foam flow will be introduced. The model of choice is the CMG-STARS model, which will be observed from both a theoretical and practical point of view. The theoretical part will discuss the equations that compose the model. The practical part will explain which input data is required, and how the model can be solved effectively.

2.4 The CMG-STARS model

By combining fundamental equations for flow through porous media with empirical relationships the foundation is built for the CMG – STARS model (Cheng et al., 2000; Computer Modeling Group, 2007). In this model the gas relative permeability is multiplied by a factor *FM*, which amongst others contains a function describing dry-out and shear thinning.

One of the features of this model is the ability to account for different flow characteristics in the high and low foam quality regime. For low qualities, it allows for an increase in apparent foam viscosity until the maximum is reached, after which the apparent viscosity gradually decreases. A second feature is that many of parameters that are associated with this model can be obtained by performing laboratory experiments (Abbaszadeh et al., 2014; Ma et al., 2013, 2014).

This chapter will explain which experiments need to be conducted in order to utilize the CMG – STARS model, as well as provide a theoretical background and a practical step by step explanation on how to approach implementing the experimental results.

2.4.1 Experimental prerequisites

In order to apply the CMG-STARS model experimental input is required. Most important are the data obtained from experiments in which the apparent viscosity of foam has been observed over the full range of injected foam qualities. The foam viscosity can be obtained through calculation by measuring the pressure drop over a core of a known length and with known cross-sectional diameter which is in a steady state through the use of Darcy's Law. The procedure on how to perform these calculations and how to let the CMG-STARS model successfully determine relevant parameters is described in the section 2.4.3.

An example of an experimental setup that can be used to obtain the required data is given in the chapter Experimental methods. First of all, the set of equations that compose the model will be discussed.

2.4.2 Required functions prior to modelling

The experimental setup can measure pressure drops at certain intervals. The pressure drop for every measurement can be directly converted to apparent viscosity through Darcy's Law (13):

$$\mu_{app} = -\frac{k \bullet A \bullet \Delta P}{q_{tot} \bullet L} \tag{13}$$

With q_{tot} as the fixed total Darcy velocity:

$$q_{tot} = q_{gas} + q_{liq} \tag{14}$$

The core cross-sectional area A is known, and permeability k can be determined from a separate experiment. In a permeability-testing experiment a fluid with a known viscosity will be injected at different flow rates while the pressure drop over the core is measured. The relationship between pressure drop and injection rate can be plotted and yields the permeability.

In order for the experiment to be useful q_{tot} has to be constant, hence its two constituents $q_{gas}$and q_{liq} should be accurately controlled. For injection of CO_2 solubility should be taken into account, this can be done through Henry's Law, equation (15). Henry's Law relates solubility to pressure.

$$S = k_H \bullet P \tag{15}$$

Henry's Constant, k_H, is different for each gas. Indeed it is higher for CO_2 (0.034 mol L^{-1} atm^{-1}) than for example N_2 (0.00061 mol L^{-1} atm^{-1}) at the same temperature. The total solubility in [mol L^{-1}] can be converted to a volumetric flow rate by the Span & Wagner equation of state, which gives the molar density of CO_2 based on ambient temperature and pressure (Span & Wagner, 1994). Again this is a pressure dependent relationship. Due to the pressure gradient required to achieve foam flow, pressure will not be equal through the core during the experiment. By setting the outlet pressure as high as the available equipment allows, the relative pressure change will be minimized. Therefore solubility and compression of the gas will remain as constant as possible, and the foam quality is independent of location. This means a steady state has been reach along the entire core. The amount of gas that should be co-injected with the surfactant is now known. It is the total amount of gas that will dissolve, plus the total amount of gas that remains undissolved and makes up for the gas fraction in the foam. The next chapter explains this in more detail.

$$q_{g,inj} = q_{g,liq} + q_{g,gas} \tag{16}$$

2.4.3 Modelling equations

In absence of oil when only gas and water are present, in total 13 parameters are involved with modelling the incompressible isothermal 2-phase foam flow through a porous medium in which the dry-out function and shear thinning effect are included. The set of equations show these parameters S_{wc}, S_{gr}, k_{rw}^0, n_w, k_{rg}^0, n_g, μ_w, μ_g, *fmmob*, *fmdry*, *epdry*, *fmcap* and *epcap.* The explanation of the last five parameters is given in Table 1 and obtained from (Computer Modeling Group, 2007)

Parameter	Explanation
fmmob	Reference mobility reduction factor in foam model. For strong foams this number is typically large
fmdry	Critical water saturation. Below this saturation foam collapses.
epdry	Parameter regulating slope of dry-out function, tuning the abruptness of the dry-out process. A small value indicates a smooth transition.
fmcap	Smallest capillary number expected to be encountered by foam.
epcap	Represents shear thinning behaviour in low quality regime.

Table 1: Explanation of fmmob, fmdry, epdry, fmcap and epcap

By utilization of the equations these parameters will be obtained to fit the model. It is assumed the relative-permeability parameters are known or can be reliably estimated. The equations are obtained from the literature (Abbaszadeh et al., 2014; Boeije & Rossen, 2013; Computer Modeling Group, 2007; Ma et al., 2013, 2014).

$$S_w + S_g = 1 \tag{17}$$

Equation (17) indicates a two-phase system with a satisfied material balance of phase saturations. Since a system is observed at steady state so saturations do not change over time, this equation will suffice.

$$u_w = -\frac{k \bullet k_{rw} \bullet \nabla p_w}{\mu_w} \tag{18}$$

$$u_g = -\frac{k \bullet k_{rg}^{f} \bullet \nabla p_g}{\mu_g} \tag{19}$$

Equations (18) and (19) apply Darcy's Law to foam-free systems to obtain the momentum balance.

$$k_{rw} = k_{rw}^{0} \left(\frac{S_w - S_{wc}}{1 - S_{gr} - S_{wc}} \right)^{n_w} \tag{20}$$

$$k_{rg}^{f} = k_{rg}^{nf} \bullet FM = k_{rg}^{0} \left(\frac{S_g - S_{gr}}{1 - S_{gr} - S_{wc}} \right)^{n_g} \bullet \frac{1}{1 + fmmob \bullet F2 \bullet F5} \tag{21}$$

Equations (20) and (21) are Corey-type relative-permeability curves. Equation (21) includes the foam dry-out and shear-thinning functions (F2 and F5) in the foam model.

$$F2 = 0.5 + \frac{arctan\left[epdry(S_w - fmdry)\right]}{\pi} \tag{22}$$

$$F5 = \left(\frac{fmcap}{N_{ca}} \right)^{epcap} \tag{23}$$

$$N_{ca} = \frac{u_{tot} \bullet \mu_{foam}}{\sigma_{wc}} \tag{24}$$

Equations (22) and (23) describe the foam dry-out and shear-thinning effect. Lastly, equation (24) calculates the capillary number.

As explained, the steady-state experiments work with a fixed total velocity. The gas fractional flow is controlled, and by measuring the pressure drop over the core the apparent viscosity can be calculated. Similar to before:

$$f_g = \frac{q_g}{q_g + q_w} \tag{25}$$

$$\mu_{foam,app} = -\frac{k \bullet A \bullet \Delta p}{(q_{gas} + q_{liq}) \bullet L} \tag{26}$$

These equations can be re-written by using equations (17)-(19) to replace the fluxes. Furthermore, capillary-pressure gradients and potential changes due to height differences will be ignored. This yields f_g and $\mu_{foam,app}$ as a function of water saturation, which are the two main objective functions of the model given in equations (27) and (28).

$$f_g = \frac{1}{1 + \frac{k_{rw}(S_w)}{\mu_w} \frac{\mu_g}{k_{rg}^f(S_w)}} \tag{27}$$

$$\mu_{foam,app} = \frac{1}{\frac{k_{rw}(S_w)}{\mu_w} + \frac{k_{rg}^f(S_w)}{\mu_g}} \tag{28}$$

Based on this theoretical framework, it can now be described how the parameters *fmmob*, *fmdry*, *epdry*, *fmcap* and *epcap* describing the system behaviour, can be obtained.

2.4.4 Fitting procedure

Based on the equations described in the previous section a number of steps will be performed in order to find the five variables in such a way that they most closely match the experimentally observed values. A step-by-step elaboration on the procedure is given in this chapter.

1) Obtain experimental values

Variable	From
f_g	Core-flooding experiment
μ_{app}	Core-flooding experiment
σ_{wc}	Surface tension experiment
k	Permeability experiment
A	Core size data
u	Experiment parameter
S_{wc}	Measure
S_{gr}	Measure
k_{rg}^0	Measure
n_g	Measure
k_{rw}^0	Measure
n_w	Measure

2) The function framework should be defined. Despite the model consisting of two main objective functions, they are a function of other functions, which are on their turn functions of other functions and so on. In order to maintain overview it is wise to break the larger functions down into smaller parts. F5 should not be included yet and be put to 1.

   The final result should be two fully defined functions describing f_g and $\mu_{foam,app}$ with all their variables as a function of S_w, *fmmob*, *epdry* and *fmdry*.

3) Define the range over which water saturations will be observed to be in between connate water saturation S_{wc} and one minus the residual gas saturation $1\text{-}S_{gr}$.

4) Without taking function F5 into account, the error between the modelled foam behaviour and the behaviour that was observed should be made as small as possible by finding the optimal *fmmob*, *epdry* and *fmdry*. Therefore, a function should be defined which simply calculates the difference between the actual measurement and the modelled result for the water saturations at which the real measurements were taken.

   Model fitting can be enhanced by introducing a 'weight factor' to the measured values. This weight factor multiplied with the error at a certain water saturation, will give that certain point an increased importance when a least square error algorithm is applied to find the best model fit. For example, when the point where the maximum apparent viscosity is found is given an increased weight factor the algorithm will match *fmmob*, *epdry* and *fmdry* in such a way the modelled foam behaviour finds its maximum at the same location.

5) Make an initial guess for *fmmob*, *epdry* and *fmdry*. A least-square error algorithm will attempt to find the optimum, but the time it requires to find the optimum can greatly be reduced by wisely choosing the initial conditions.

6) Solve the nonlinear least-square problem. This is easily done with a software program for numerical computation such as MATLAB which can apply either a trust region reflective algorithm or the Levenberg - Marquardt algorithm. In vector terms, the optimization problem that will be solved this way can be stated as:

   $$min_x \|f(x)\|_2^2 = min_x(f_1(x)^2 + f_2(x)^2 + \cdots + f_n(x)^2)$$

   Where in this case *x* is a 1x3 matrix containing *fmmob*, *epdry* and *fmdry*. The model is now solved for the scenario where only F2 is involved.

7) For the situation where the shear-thinning effect is included, an initial guess for *fmcap* and *epcap* needs to be made in addition to the initial estimations made at 5).

8) When solving the nonlinear least-square problem similar to step 6), rather than solving for 3 different values, the system is now searching for 5 parameters to fit the data. Compared to step (7) which solved for the situation without F5, obtaining the best fit has become slightly more complicated. It takes an extra, implicit, step to calculate the apparent viscosity.

9) For the situation where F5 is involved step 2) has to be repeated. This time, the functions of which the function framework is constructed depend not only on S_w, *fmmob*, *epdry* and *fmdry*, but also on three parameters associated with implementing F5: *fmcap*, *epcap* and μ_{foam} (see equation(23)).

   However, μ_{foam} has now become a function of itself in such a way that it became impossible to solve analytically. Again, with a program for numerical computation the solution for μ_{foam} can easily be found. When the equation is numerically solved, the nonlinear least-square solving algorithm can adjust the 5 remaining parameters to achieve a better fit between μ_{foam} and the experimentally observed parameters.

Appendix A – MATLAB scripts contains the MATLAB script which closely follows these steps.

2.5 Summary

This chapter has provided insight in how surfactants work, and how they work in foam creation. One of the main principles behind surfactants is their ability to reduce surface tension, and enhance interactions between lamella interfaces. This helps reinforce the lamellae by increasing the maximum disjoining pressure. Some methods that can cause foam creation in porous media have been described. Also some methods that discussed foam destruction have been touched upon, and it has become clear that foam flow in a porous medium is a continuous process of these generation and destruction mechanics.

An overview of the approaches the different categories of foam models use is provided. Some models try to accurately describe the mechanistic processes of bubble generation and destruction, while others try to match empirical correlations with experimental data. A semi-empirical model can be used as an ‘in-between’, by combining some physical, mechanistic aspects with empirical correlations that are easy to use. The CMG-STARS model is an example of this. A detailed guide on how to implement experimental data into this model has been provided. The guide provides a practical solution on how to solve the different equations involved in this model by using a numerical computation program.

This thesis aims to combine elements of surfactant- with nanoparticle mechanics and uses parameters from the CMG-STARS model to describe the result. The next chapter will discuss nanoparticle physics in order to be able to do this. It will become clear that nanoparticles and surfactants have many similarities.

3 Nanoparticles

Nanoparticles are at the core of this study. In this chapter it is explained why nanoparticles can aid in the generation of a stronger foam. In order to fully describe why it is believed nanoparticles have a beneficial effect on foam, their physical behaviour will be described. Afterwards it will be explained how nanoparticles enhance foam, or how the nanoparticles themselves can act as a surfactant. Ongoing research will also be discussed in this chapter.

3.1 Nanoparticle physics

The behaviour of nanoparticles is fundamentally different from particles at a much larger scale (centimetre and above). The dominant forces that govern the motion of larger objects play a very different role on these very small objects. Similarly, parameters that do not play a significant role in the behaviour of large scale objects become very important when considering nanoparticles. Temperature is a good example, a cup of coffee will be freshly made at 90 degrees Celsius, but it is essentially the same at 10 degrees, albeit less tasteful. For objects on a small scale temperature plays a dominant role. Apart from temperature this chapter will discuss the important nanoparticle parameters.

3.1.1 Surface interaction

For the successful application of nanoparticles foam boosters, the nanoparticles are required to be in the dispersed state. In other words, they have to be separated particles that do not agglomerate over time. In order to achieve this the aggregation – dispersion behaviour should be understood. This behaviour is controlled by the interaction between the surfaces of neighbouring nanoparticles, and to get an overview of what forces are influencing the interactions are displayed in Table 2.

Surface interaction	Generation mechanism
Van der Waals interaction	Short-ranged electromagnetic force between molecule and/ or atoms, which have neutral charge only
Overlap of electric double layer	Electrical interaction by the overlap of electrical double layer around particle in solution
Steric interaction of adsorbed polymer	Short-ranged interaction by the overlap of adsorbed polymer layer on particles
Bridge force	Formation of the bridge of polymer binder and/ or surfactant between particles
Hydration force	Overlap of hydrogen – bonded water molecule on hydrophilic surface on particle
Depletion	Negative absorption of solute and polymer by having less affinity for the surface than the solvent

Table 2: examples of surface interaction between particles in liquid phase, adjusted from (Kamiya et al., 2012)

3.1.2 DLVO theory

The van der Waals interaction and overlap of electric double layers, the first two items of the table, are the main constituents of the DLVO theory, which is named after its creators Derjaguin, Landau, Verwey and Overbeek (Verwey & Overbeek, 1999).

3.1.2.1 Van der Waals force

The 'van der Waals force' (or interaction), is the sum between attractive or repulsive forces between molecules, other than those due to covalent bonds, or electrostatic interaction of ions with another or with neutral or charged molecules. It therefore has three components:

- The force between two permanent dipoles (Keesom force)
- The force between a permanent dipole and a corresponding induced dipole (Debye force)
- The force between two instantaneously induced dipoles (London dispersion force)
- The Pauli exclusion principle

Where a permanent dipole is a molecule which has (at least) 2 atoms with a large difference in electronegativity and hence create a dipole. An induced dipole can be created when a permanent dipole repels the electrons of another molecule, inducing a dipole moment. An instantaneous dipole is created because electrons tend to move around a lot, and therefore can create a temporary difference in electron concentration. The Pauli exclusion principle is a quantum-mechanical principle that prevents the collapse of molecules.

If a real-life example has to be given that represents the DLVO theory, one could think of a table full with magnets. All magnets (dipoles) attract and repulse one another, creating an initially random movement. However, in the end the majority of those magnets would most likely end up stuck together. This is not the case with molecules in a liquid. Because of thermal energy (temperature), the molecules will always be in thermal motion. Therefore the electrostatic attraction will be averaged during a longer time, as molecules spin, turning an attracting into a repulsive force. This can be called the 'thermal averaging' effect. It is said that thermal averaging at room temperature is usually enough to overcome the electrostatic component (the Keesom force).

Both the Keesom force and the Debye force require permanent dipoles to be present. When this is not the case, the London dispersion force will be the main contributor to the van der Waals force.

The modelled net resulting force between a pair of molecules as a function of distance is called the Lennard-Jones potential. It is often used as an aid in the visualization of the DLVO theory, as can be seen in Figure 11.

3.1.2.2 Electric double layer

When present in a liquid (nano)-particles may provide surfaces that are electrostatically charged, resulting in a so-called 'wall surface potential'. Ions that are present in the liquid may be attracted or repulsed by this potential, depending on whether they are co- or counter-charged. It may be obvious that for the case where this surface is in equilibrium with the liquid, the electrostatic charge is neutralized by the presence of the counter-ions. This means that there is an increased presence of these counter-ions in the region near the particle surface, in a region known as the 'electrical double layer', or EDL.

Within the EDL, two zones can be distinguished. Very close to the charged surface, the ions are strongly attracted and are therefore relatively immobile. This zone is called the 'Stern layer' or 'Helmholtz layer'. Further away from the surface the ions are much less bound to the surface, and are more mobile. The counter-ions surrounding the wall minimize the Gibbs free energy. Furthermore, it results in a layer of ions surrounding the surface of the particle. The ions in this layer have equal charge, which is either positive or negative. The layers surrounding other particles in the liquid have the same charge. Therefore, the layers of individual particles generate a repulsive force between those particles. With increasing distance between the particles, the magnitude of the repulsive force decreases.

The DLVO theory consists of the (repulsive) double layer force, and the van der Waals force, which can be approximated by using the Lennard-Jones potential. Combining the two mechanisms yields the result displayed in Figure 11.

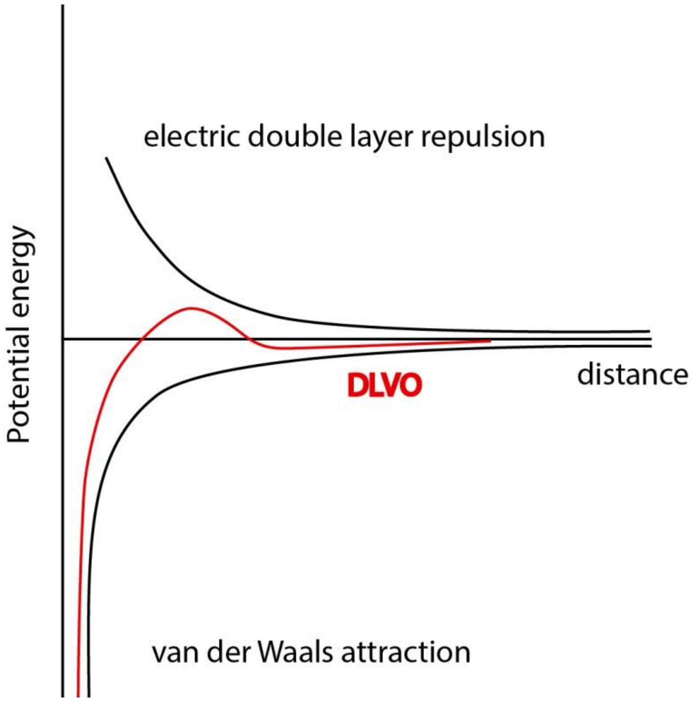

Figure 11: sketch of DLVO attraction and repulsion consisting of its two constituents. The resulting DLVO interaction is displayed in red.

In the sketch it can be observed the attractive van der Waals force is dominant for a close distance between two particles. When some distance is maintained, the electric double layer repulsive force has the upper hand. According to the DLVO theory, two particles will remain separated once a certain distance between the particles has been achieved. This distance is typically in the nm range. When the surfaces are closer to each other, the surface repulsive potential cannot prevent aggregation. This principle will be utilized during the preparation of nanoparticles, described in the section Nanoparticle Preparation.

3.1.3 Nanoparticle surface properties

When nanoparticles are suspended or dispersed in a liquid, they continuously collide with other particles because of the liquid movement, or the random thermal motion. Because of the continuous collisions, there are ample opportunities for nanoparticles to coagulate. Whether or not coagulation occurs depends on the balance between the kinetic energy nanoparticles possess, and the energy potential associated with their interaction potential. When coagulation of two particles leads to a lower total potential energy, coagulation as a result of these collisions is more likely to occur.

The relative moment of two particles *i* and *j* involved in a collision can be described by a general motion equation, equation (29):

$$m_i\left(\frac{dv_{ij}}{dt}\right)=F_{Iij}+F_{Bij}+F_{Fij} \tag{29}$$

Where v_{ij} is the relative velocity of the particle, F_{Iij} the static interaction independent of fluid motion, F_{Bij} the time-averaged force due to Brownian motion, and F_{Fij} the hydrostatic interaction.

The most fundamental theory on the stability of dispersions describes the stability solely as a function of parameter F_{Iij}. This parameter describes effects such as van der Waals and electrostatically repulsive forces as mentioned earlier. When this repulsive force exceeds a certain threshold, a particle collision will not result in coagulation. Because the stability only depends on $\mathrm{F}_{\mathrm{Iij}}$ and not the other two forces mentioned in equation (29), no knowledge is required on the detailed relative moment of the particles. This makes this theory very useful to work with. In cases where much more collisions between particles can be expected this theory does not suffice. In that situation the equation needs to be solved to assess the contribution of each individual force.

A contributor to the parameter F_{Iij} is the electrostatic repulsion. This can be due to the electric double layer effect, or due to the surface charge of the nanoparticles themselves. There are three mechanisms for surface-charging a nanoparticle.

- Charging by functional groups
- Charging by adsorbed ions
- Charging by isomorphic substitution

Oxide particles such as SiO_2, TiO_2 and Al_2O_3 are susceptible to charging by functional groups. An example is the adsorption of water molecules and formation of –OH groups on the particle surface. Once a metal oxide has adsorbed a water molecule, ions in the water may react with the –OH group:

$$M-O^{-}+H_2O \overset{OH^{-}}{\rightleftarrows} M-OH \overset{H^{+}}{\rightleftarrows} M-OH_2^{+}$$

In the chemical reaction above *M* represents a metal atom. The balance of the above equation depends on the balance of H_3O^+ and OH^- ions, or the pH of the solution. At high acidity the surface potential is always positive, and for high alkalinity this surface potential turns negative. Somewhere in between there is a point of zero charge, pH_0. Each oxide has their own point of zero charge. For example, SiO_2 pH_0 is around 2.6, for α-Al_2O_3 pH_0 is found around 9.

The other two charging mechanisms, charging by adsorbed ions and charging by isomorphic substitution have only limited relevance in this study. Charging by ionic adsorption occurs mainly in AgI crystallized nanoparticles and a few variants such as AgBr, AgCl and Ag_2S. Their surfaces may be charged because of an excess of either adsorbed Ag^+ or I^-. Charging by isomorphic substitution occurs mainly in clay particles. Their crystalline structure may contain defects where Si^{4+} ions have been substituted by Al^{3+}. The difference in charge results in charging particles.

As described above, nanoparticles in a liquid are generally charged. The characteristics of their behaviour due to this charge can be divided in mechanics that can be explained with the DLVO theory, and non-DLVO interactions.

3.1.3.1 DLVO interaction and dispersion control

When the DLVO theory had been introduced, the Stern layer and EDL were discussed, with the Stern layer consisting of firmly adsorbed ions on the particle surface, and the EDL consisting of a ‘cloud’ of ions neutralizing the surface electric charge. The gradient of electric potential draws ions to the surface, while thermal diffusion counteracts this force. At the surface, the potential can be denoted as Ψ_0, which decreases linearly until the boundary of the Stern layer and EDL, Ψ_d. It is very difficult to experimentally determine the value of Ψ_0, so instead the term Ψ_d is used, which is also called the ‘zeta potential’.

The magnitude of the zeta potential is a measure for the electrostatic repulsion between charged particles. It therefore is an important indicator for the stability of a colloidal dispersion. When the potential (or repulsion) is small, attracting van der Waals forces are more likely to overcome the repulsing forces, triggering aggregation. Similarly, particles with a high zeta potential, or high repulsion due to their charge, are more likely to resist aggregation. Table 3 gives an indication of the stability of a liquid as a function of their zeta potential.

Zeta potential [mV]	Colloidal stability
0 – 10	Fast coagulation
10 – 30	Beginning instability
30 – 40	Moderate stability
40 – 60	Good stability
60 and above	Excellent stability

Table 3: colloidal stability for zeta potential ranges

Together with the molar concentration of electrolytes, the zeta potential are the main parameters to control in order to achieve dispersion stability. The zeta potential can be adjusted by controlling the pH, as has been described in the section ‘Nanoparticle surface properties’. The concentration of available electrolytes (C_e) can be controlled by adding salts. The electrostatic repulsive force of the particles disappears when more salts are present. The Critical Coagulation Concentration, or CCC, is the C_e for which the repulsive electrostatic potential equals the attractive potential due to van der Waals forces. When C_e > CCC, the coagulation rate is constant, and for C_e < CCC the coagulation rate is called the ‘slow coagulation region’. The CCC can be calculated as shown in equation (30).

$$CCC = \frac{7{,}2 \ x \ 10^{-57} \varepsilon_r^3 T^5}{z^6 A^2} \tag{30}$$

Where ε_r is the medium permittivity, T is the temperature, z is the electrolyte charge and A is Hamaker’s constant. As CCC is reversely proportional to z^6, the CCC for divalent ions is 64 times lower than for monovalent ions, and for trivalent ions the CCC decreases 729 times. The addition of multivalent ions to a dispersion can be very effective to promote aggregation. Because of the same reason, even a very small concentration of di- or trivalent ions can quickly destabilize an otherwise stable dispersion.

Summarizing, when the DLVO theory is followed either the zeta potential or electrostatic repulsion should be changed to modify stability. Changing the repulsion can be done effectively by controlling the valence and amount of ions present in the liquid phase.

3.1.3.2 Non-DLVO interaction and dispersion control

Not all interactions that have been observed by previous experiments can be explained solely by the DLVO model. Examples of non-DLVO interactions that could be relevant for this study are surfactant and polymer interactions.

3.1.3.3 Surfactant interaction

Surfactants often have a hydrophilic head and a hydrophobic tail. When the particle itself has hydrophilic or hydrophobic properties, surfactant can adsorb on the particle surface. In the case of a hydrophobic nanoparticle, for example, the tail is adsorbed on the surface while the head will be directed towards the solution. When dispersed, the charge of the adsorbed surfactant heads will increase the stability.

Surfactant adsorption will also occur when a surfactant with the opposite charge of the nanoparticle surface is chosen. As the surfactant heads will carry this (opposite) charge, they will tend to adsorb on the particle surface. This will have a negative effect on the dispersion stability. Hydrophobic heads adsorbing on the particle surface will turn the whole particle hydrophobic when the surface is fully covered, as hydrophobic particles tend to be attracted to each other. In this scenario the dispersion may be stabilized again by addition of more surfactant. This will create a second layer of adsorption in which the heads of additional adsorbed surfactants are pointing outward, effectively reversing the surface charge and therefore stabilizing the solution.

3.1.3.4 Polymer interaction

As is displayed in Table 2 some forces influencing the interaction between particles are related to polymers. These forces arise when a polymer dispersant is added to the liquid, which leads to a process called physical adsorption.

Physical adsorption occurs when a polymer is adsorbed on the particle surface. This way, steric repulsion and the dissociation of modifier molecules increase the electrostatic repulsion force. Steric repulsion relies on the amount of volume atoms within a molecule require. Electron clouds surrounding individual atoms being brought in close proximity require a certain amount of energy in order to do so, which is energetically unfavourable. An energetically favourable state can be achieved when the polymer string adsorbs on the particle surface. If this is to be done successfully the structure of the polymer should be considered. Both the molecular weight and the concentration of the polymer dispersant have to be carefully chosen. In the ideal case, each particle to be dispersed is totally covered with polymers.

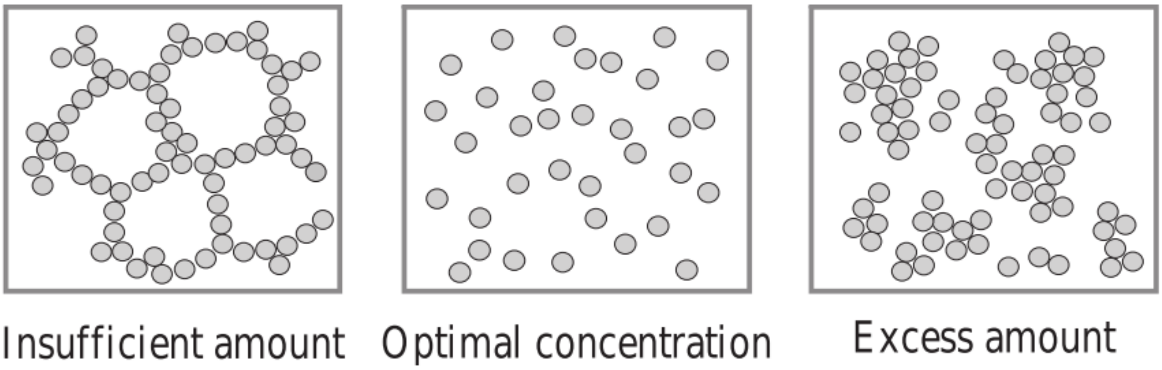

Figure 12: effect of polymer concentration on particle (Kamiya et al., 2012)

Figure 12 displays the effect of surface coverage of polymers on particle aggregation. In the case of a polymer deficit, uncovered surfaces will still tend to aggregate with other uncovered surfaces. Polymers have the opportunity to bridge multiple particles, creating chain like aggregation. In the case of excess polymer, the concentration of polymer dispersant in the liquid phase increases. This promotes collision between the particles, and 'massive' aggregates will form. In both cases the polymer acts as a flocculant.

3.1.4 Nanoparticle dispersion achievement

When nanoparticles are supplied in a dry state they are often in aggregated form, as stacking pressure during drying or transportation overcomes repulsive forces. Theories on stability of nanoparticles are only valid on nanoparticles, and not on their coagulated form. The mechanics of individual nanoparticles can often not be put to use to turn aggregates into stable nanoparticles. This section investigates some methods to reverse the aggregation process.

The red curve in Figure 11 resembles the attraction or repulsion according to the DLVO theory. The highest value the calculated DLVO potential achieves is an indication whether or not the particle can be dispersed. If this peak value of the potential energy is 10-20 times higher than the product of absolute temperature T and Boltzmann constant k, it is considered physically possible to achieve a dispersion (Kamiya et al., 2012).

The average distance between the particles depends on the solid fraction, and will be given by Woodcock's equation (Woodcock et al., 1987).

$$h_{susp} = D_p\left[\left\{1/\left(3\pi F\right)+5/6\right\}^{0.5}\right] \tag{31}$$

Where h_{susp} is the mean surface distance between the particles, F is the solid fraction, and D_p is the particle diameter. As can be seen in equation (31), the average distance will decrease with increasing fraction of solids. Additionally, the average surface distance decreases with decreasing particle size, e.g. the mean surface distance for small particles is smaller than for larger particles with the same solid fraction F. For the successful dispersion of larger particles additional repulsive forces can be required, as the electrostatic repulsive force alone is not sufficient, especially for high solid concentrations. In such cases steric forces improve dispersion stability. Polymer dispersants can provide these steric forces by surface modification, but have their own challenges to overcome. More on this is in the section Nanoparticle surface properties.

Because of the small size of the nanoparticles, they are not susceptible to fluid drag. Stirring of the suspension will not be enough to obtain a dispersed state. Rather, ultrasonic homogenisation, subsonic slurry collision, milling methods or other mechanic techniques will be required to break the agglomerates.

3.1.4.1 Ultrasonic milling

The working principle behind ultrasonic milling relies on sound waves being transmitted into a fluid through the use of a so-called ‘sonotrode’. The sonotrode is a mechanical component that transmits ultrasonic vibrations from a transducer to the fluid. Because of the sinusoidal behaviour of these vibrations, alternating high- and low-pressure cycles are generated inside the liquid. During the low-pressure regime small bubbles will form. They are mostly vacuum, but can also contain a low quantity of vapour. While they can expand during the low-pressure phase, the high-pressure phase will cause the voids to violently implode. This process is called ultrasonic cavitation. Ultrasonic cavitation causes local high-velocity liquid jets which can achieve speeds of up to 1000 km/h, while the local pressure can temporarily increase to over 2000 bar and temperatures exceeding 5000 ˚K.

There are three mechanisms reducing the size of agglomerated particles because of ultrasonic cavitation (“Ultrasonic Wet-Milling and Micro-Grinding,” 2014):

- Erosion
- Shear failure
- Fission

Surface erosion is caused by vacuum bubbles collapsing in very close proximity to the surface. The local liquid jets cause very high shear rates within the liquid. Larger (agglomerated) particles are more susceptible to fluid drag and will hence be subjected to high internal shear stresses when in proximity to one of these jets. When the failure rate of the particle is exceeded this will cause the particle to break. Lastly, fission because of inter-particle collisions is able to decrease particle size too. Jets have the ability to ‘launch’ and accelerate a particle to a high velocity. If this particle hits another particle before it slows down, the energy released at impact can be enough to defragment either one or both particles. Because of these three effects, ultrasonic treatments have the potential to not only de-agglomerate coagulated particles but can also prove to be an effective milling or grinding technique.

Ultrasonic techniques can be applied to obtain a short term dispersion, but in order to maintain stability over an extended period this will not suffice. For long-term stability, the surface chemistry of nanoparticles should be understood.

3.2 Nanoparticles in foam applications

Nanoparticles are in many ways similar to surfactants. For their surfactant-like properties they are dependent on their capabilities to adsorb on the interface between two fluids. For foam enhancement, one would be particularly interested in how their adsorption on a liquid – vapour interface behaves. A number of mechanisms which can achieve this have been identified.

3.2.1 Coalescence prevention

This effect has first been noticed in the very early 20th century (Pickering, 1907). He described this phenomenon for the case where solid particles were employed to stabilize an oil-water emulsion. The same principles also hold true when the particles are able to adsorb on a gas-liquid interface. As has been described earlier, the contact angle between a particle surface and the liquid is a measure of hydrophobicity. A small contact angle indicates the liquid will wet the surface, while a high contact angle is an indication of the opposite.

Particles that do not have a strongly hydrophilic or hydrophobic nature adsorb easy on a gas-liquid interface. The amount of energy associated with being adsorbed on that interface is given by equation (32).

$$\Delta E = -\pi r^2 \sigma_{gl} (1 - |\cos\ \theta_{gl}|)^2 \tag{32}$$

In which ΔE is the stabilization energy, r is the radius of the (spherical) particle, σ_{gl} is the interfacial tension between the gas and liquid phase, and ϑ_{gl} is the contact angle. This term is maximized for a contact angle of 90 degrees, where the cosine term will be 0. A contact angle of 90 degrees also corresponds to neither hydrophilic nor hydrophobic properties of the particle. The energy associated with adsorption on the interface can be enhanced further when the particle has amphiphilic properties.

There are more observations to be made from equation (32). Firstly, the adsorption energy increases with (the square of) particle size. This means that larger particles adsorbed at the interface provide more stability. Secondly, the energy difference is always negative. This implies that it is always favourable for a particle to adsorb at the interface rather than to stay in either of the two phases, as long as a contact angle can be defined.

This surface-adsorbed beneficial state prevents bubbles from coalescing, because if two bubbles were to coalesce the overall interfacial area has to decrease. This means that some of the particles that are at their energetically beneficial state at the interface have to leave their position, which costs a relatively large amount of energy. This energy requirement is a threshold value that is typically too large to overcome by thermal fluctuations.

3.2.2 Plateau stabilization

Foam contains thin films separating gas bubbles. Where these bubbles connect is called the foam plateau border. Figure 13 illustrates this. Drainage occurs due to for example gravity drainage or capillary suction. This process continues until the lamellae snap and the gas bubbles coalesce or until the film is stabilized. When nanoparticles have considerable hydrophilic properties they tend to collect at the plateau border.

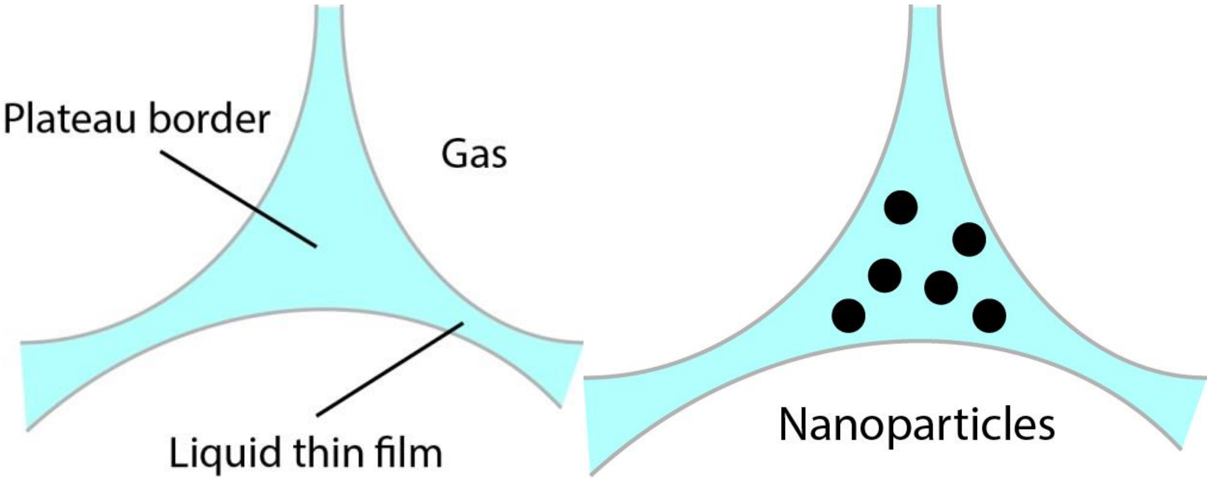

Figure 13: nanoparticles at the plateau border preventing film drainage

When the nanoparticles have gathered in the plateau border they obstruct liquid flow through that plateau, slowing down drainage. Therefore nanoparticles have a stabilizing effect on lamellae by increasing the time it requires to drain them.

3.2.3 Nanoparticle lamella bridging

Hydrophilic nanoparticles can stabilize films by bridging. This is shown in Figure 14. It shows a spherical particle that bridges between two bubble films, with a contact angle θ. If this angle is above 90 degrees, the positive capillary pressure in the film adjacent to the particles will cause drainage of liquid away from the particle. This causes a hole in the lamella. If the particle is hydrophilic the contact angle is below 90 degrees. After an initial drainage a critical film thickness is achieved and the film gets planar. Further drainage causes the capillary pressure to draw liquid towards the particle and thus stabilizes the film by bridging (Singh & Mohanty, 2014). Therefore hydrophilic nanoparticles can stabilize foam films.

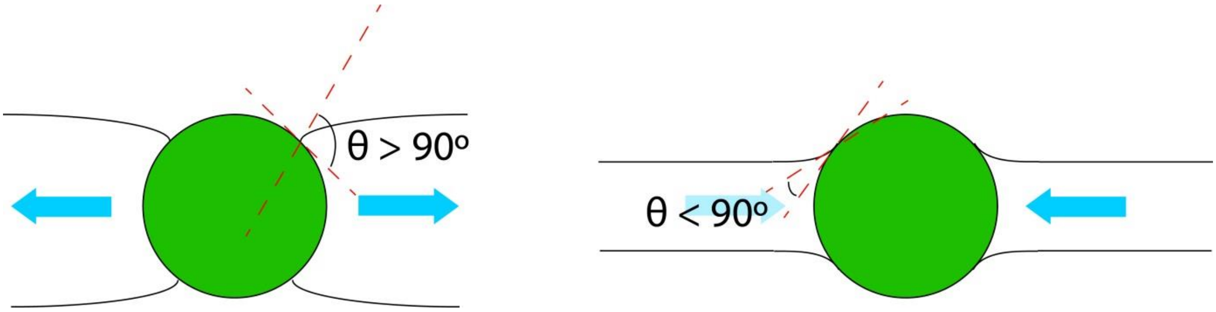

Figure 14: The effect of nanoparticle bridging (adapted from (Singh & Mohanty, 2014))

3.2.4 Amphiphilic nanoparticle foam shielding

A study suggested an ‘amphiphilic nanoparticle foam shielding’ effect. The amphiphilic properties of the nanoparticles used in this research caused them to strongly adsorb at the liquid – vapour interface, as part of the particle is hydrophilic and the other part is hydrophobic. This causes a barrier at the bubble surface which aids in the prevention of rupture and coalescence. The research showed that also at high temperature stable foams could be generated. This is a very interesting mechanic to consider for foam stabilization in the presence of oil.

In-situ, foam lamellae travel through the pores of the reservoir formation. During their travel, new foam lamella get generated, but foam lamella also get destroyed. One of the processes that destroys foam lamella are patches of oil. The change in wettability induces a change in contact angle. This causes the foam lamella to snap which is illustrated by Figure 15.

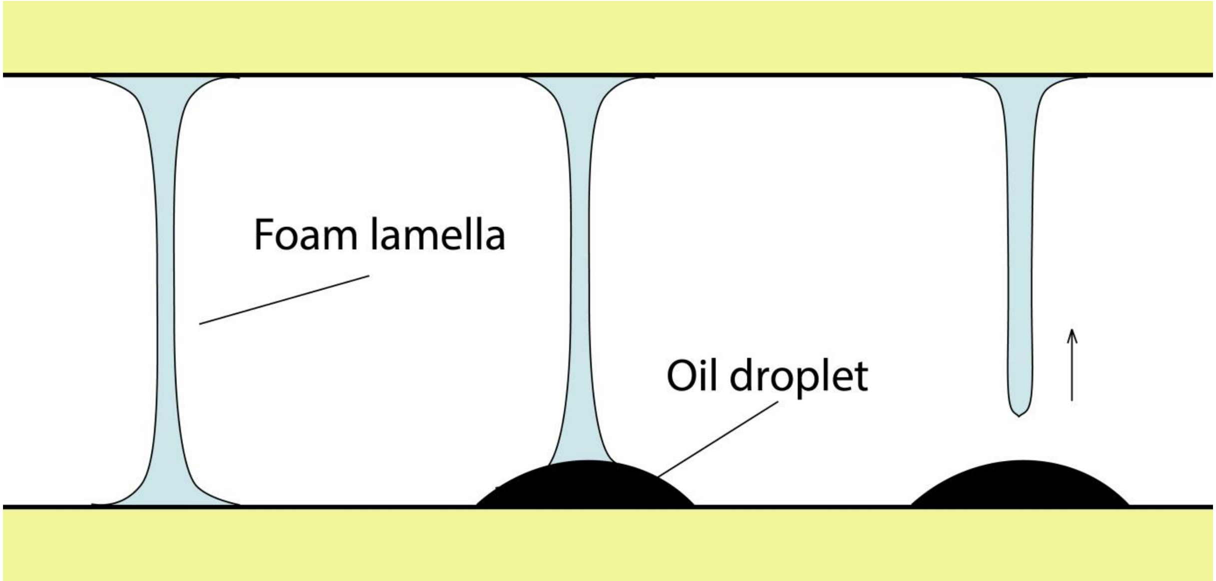

Figure 15: foam lamella destruction by snap-off at oil interface

Figure 15 displays three scenario's. The first lamella travels through the pore, unhindered, wetting both surfaces. The second lamella shows a foam lamella that is temporarily stable on the oil droplet surface. This could be due to nanoparticles shielding the lamella from contact with the oil. As long as the time the lamella resides on the foam droplet does not exceed a certain limit, the lamella can safely pass the droplet. The third lamella is not stabilized, and will therefore snap off at the oil droplet. This is caused by a change in contact angle at the lamella – oil interface. The surface tension causes this situation to be unstable. Therefore the situation as depicted in Figure 15 is not stable, causing the lamella to fully retreat until it resides at the top side of the figure.

3.2.5 Oscillatory structural force

When liquid films containing colloidal particles are thinning, this thinning occurs stepwise. Stepwise thinning is called 'stratification'. The colloidal particles can be nanoparticles, but surfactant micelles create this effect as well. There an underlying mechanisms that creates this stepwise thinning. At a liquid interface, particles that are near the interface will try to order themselves in a crystal-like manner when the surface roughness at the interface is much smaller than the particle diameter. Ordering occurs because the particles themselves are mutually repulsive, but they are forced into the restricted volume of the (thinning) film. The number density of colloidal particles at the interface will oscillate.

In the case of a thin film, the structured region around the two opposing surfaces overlap, which gives rise to an oscillatory disjoining pressure and interaction energy (Marinova et al., 1998). The amplitude of the disjoining pressure decreases exponentially with film thickness, and as the film thickness decreases, the crystal-like structure depletes layer by layer.

It has been observed experimentally that when the concentration of nanoparticles is sufficient, foam stability is enhanced because of the increased disjoining pressure (Binks, 2002).

3.3 Summary

This chapter has provided detailed information on nanoparticle behaviour. First of all, it is discussed how nanoparticle dispersions can be achieved and controlled. Much of the physics that control dispersion behaviour also influence how nanoparticles can create or enhance foam, which was discussed secondly.

With the knowledge gained in the theoretical part of this chapter those observations can be explained and understood. The fundamentals are now built to put the new type of nanoparticle to the test, and develop the right methods in order to do so. This will be done in Chapter 4.

4 Experimental methods

The experimental setups are described in this chapter. A general overview of each setup is given, and the way they are used is briefly described. After the overview of the setups other preparations required to conduct the experiments are explained. Properties of the used equipment are provided.

4.1 Setups

4.1.1 Core flooding setup 1

Core flooding setup 1 is used for experiments at low pressure and ambient temperature. It is suitable for experiments with both CO_2 and N_2. The gas feed is handled by a flow controller, obtaining its gas from a high pressure gas cylinder. Liquid flow is regulated by a pump. The two fluid flows combine prior to injection in the core. Two ΔP pressure gauges measure the pressure drop, one measures the drop over the whole core, and another measures the drop over an internal interval. Two other pressure gauges measure the pressure at entrance, and at a point in the core. By combining their readings the absolute pressure in the core can be determined at four points. Lastly, the back pressure assures a constant pressure at the core outlet and therefore the whole core. A schematic overview of this setup is given in Figure 16. Details on the equipment used are provided in Table 4.

In order to process the measurements the setup is connected to a computer. This computer displays and records the pressure measurements and optionally a scale on which the outlet vessel can be placed. Using the in-house-developed MP3 laboratory interface environment, measurements are stored every 10 seconds and written to a data file.

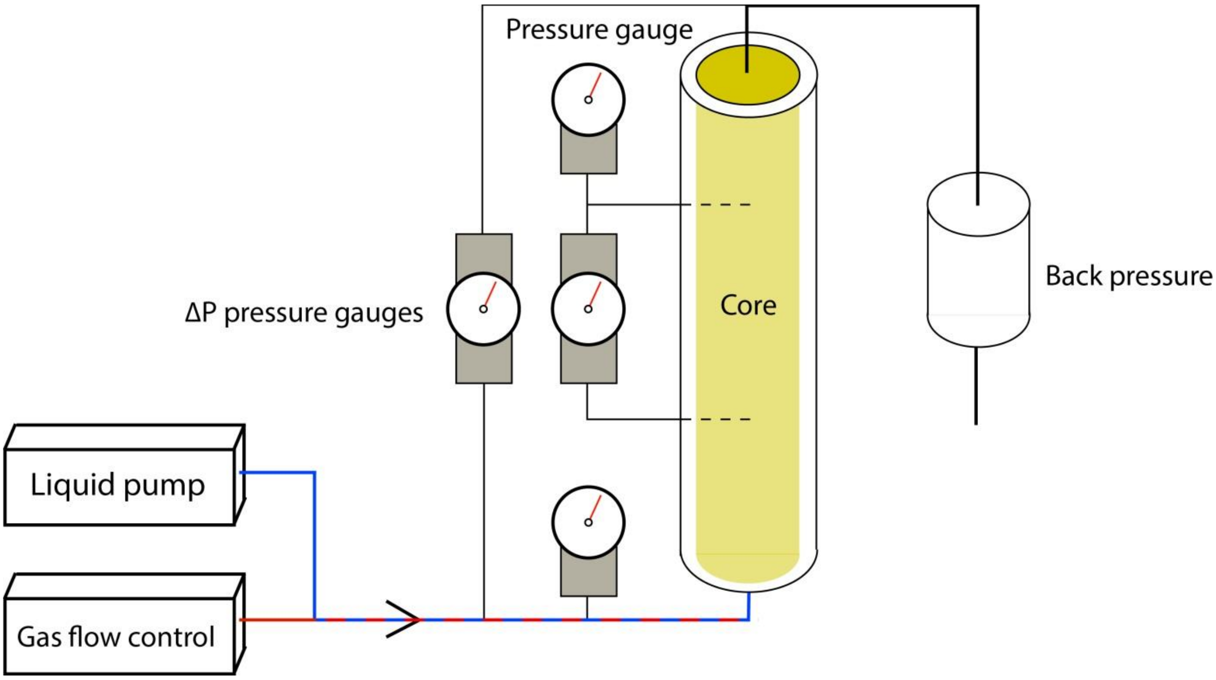

Figure 16: schematic drawing of setup 1

Component	Type
Liquid pump	General Electric P-900
Gas flow controller	Bronckhorst EL-Flow mass flow meter & pressure meter
Pressure gauge	General Electric UNIK 5000
ΔP pressure gauge	Endress Hauser Deltabar S
Core holder	Polyether ether ketone (PEEK) core holder
Back pressure	Steel/ PEEK back pressure

Table 4: setup 1 equipment

4.1.2 Core flooding setup 2

The second core flooding setup is similar to the first one. However, this setup allows for experiments to be conducted at high pressure (~80 bar) and temperature (80 degrees Celsius). Temperature is controlled by placing the core holder into an oven. In order to be able withstand the elevated pressure only metal lines are used, and the core holder is specially designed to handle high pressures. An improvement with respect to setup 1 are a fully computer-controlled gas and liquid flow controllers. A schematic overview of setup 2 is given in Figure 17, and details on the used equipment are provided in Table 5. Figure 18 is a photograph of the setup in the laboratory.

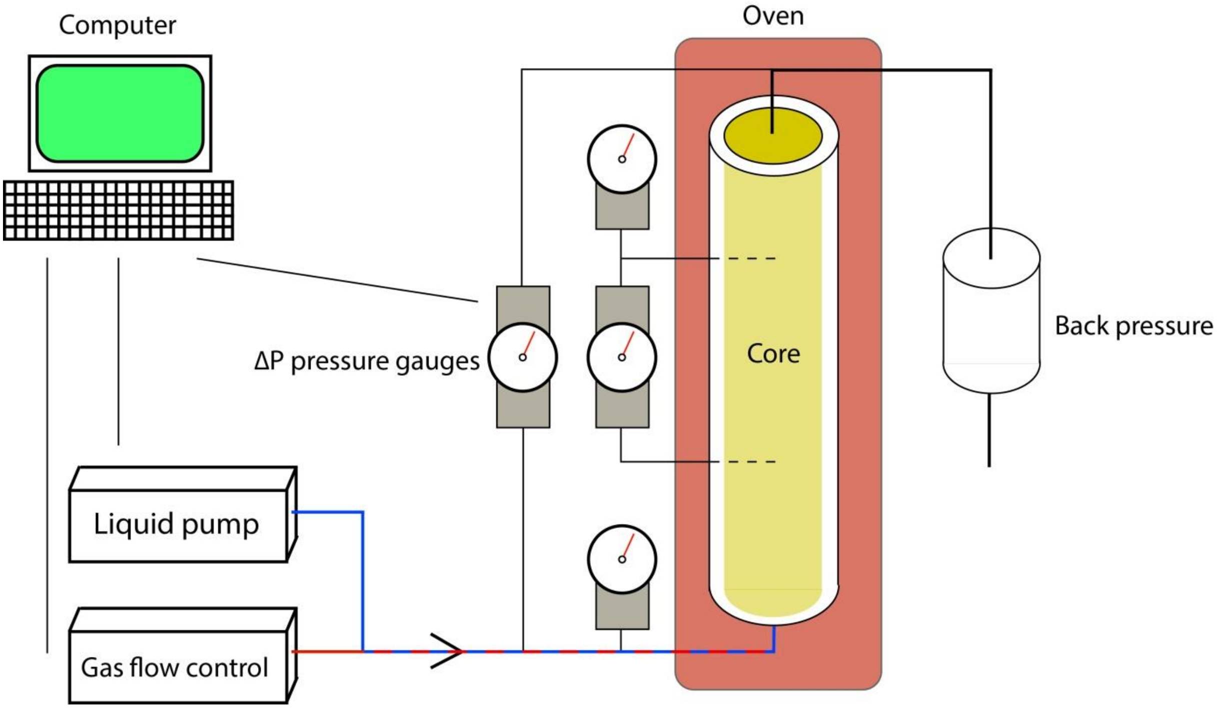

Figure 17: schematic drawing of setup 2

Component	Type
Liquid pump	Ametek Chandler Engineering Quizix QX pump
Gas flow controller	Bronckhorst EL-Flow mass flow meter & pressure meter
Pressure gauge	General Electric UNIK 5000
ΔP pressure gauge	Endress Hauser Deltabar S
Core holder	Polyether ether ketone (PEEK) high pressure core holder

Back pressure	Steel/ PEEK back pressure
Oven	Memmert UF75

Table 5: setup 2 equipment

Figure 18: core flooding setup 2

4.1.3 Foam column

Nanoparticles obstruct fluid flow in the lamellae and plateau borders, and hence reduce drainage rates of the above-lying lamellae. If this is indeed the case, generated nanoparticle-foam would be more 'wet' compared to a foam without that particle. In order to assess the potential of the nanoparticle used in this study an experimental setup bas been built to determine the capability of this particle to reduce drainage. As foam is being generated the amount of liquid in the tube will decrease. However, if the injection rate is small enough the top lamellae start to drain while foam is still being formed at the bottom. If drainage is indeed slower for the surfactant-nanoparticle combination, the liquid level for equal foam columns should be lower as there is more liquid present in the foam phase due to slower drainage.

In this setup, foam is generated by injecting gas into surfactant from the bottom side. In a column with a diameter of 4.5 cm the foam height is measured as a function of time. By comparing the liquid level to the height of the foam column, the amount of liquid in the 'foam phase' is determined. By utilizing a gas flow controller the rate at which foam is being generated is controlled. Figure 19 shows a schematic of this setup, Figure 20 shows two photographs of the setup in action.

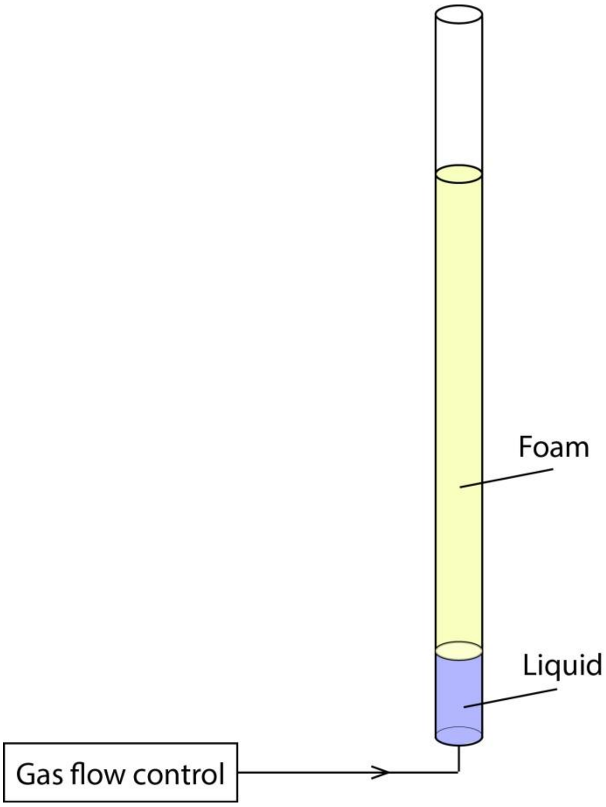

Figure 19: schematic of foam column setup

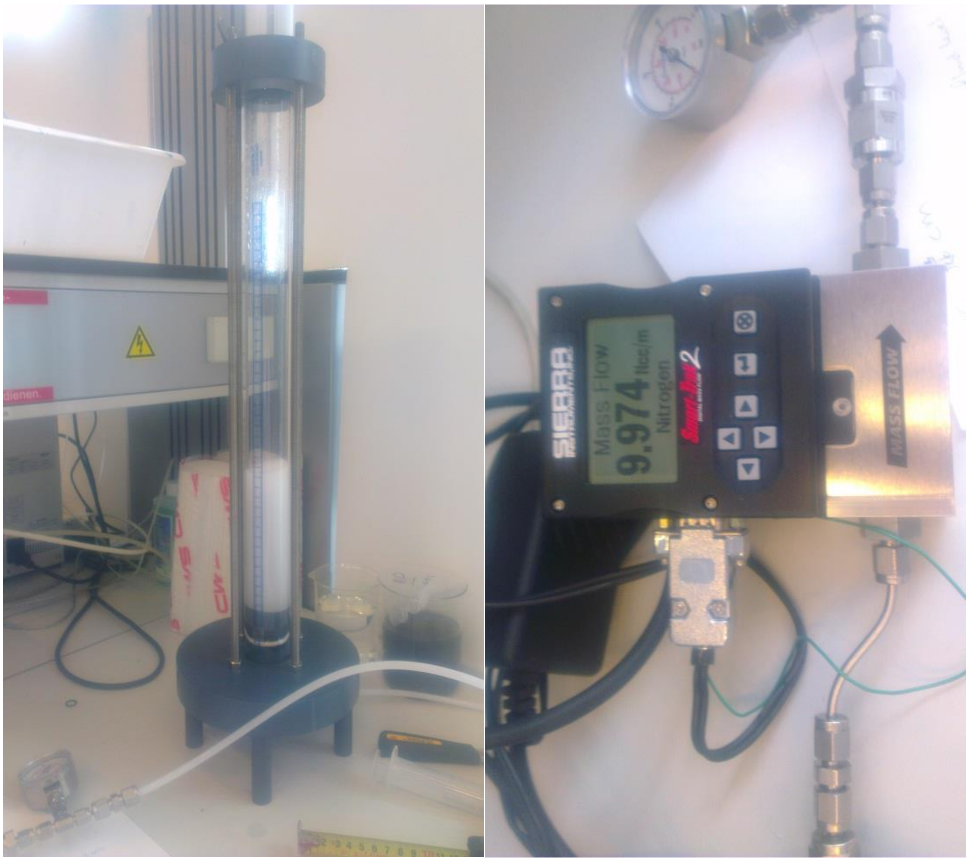

Figure 20: foam column with foam being generated on the left, Sierra gas flow controller on the right

4.2 Core preparation

The core is drilled from a larger piece of sandstone or carbonate rock. It has a length of ~17 cm and a diameter of 40 or 38,1 mm depending on the drill bit. As the experiments require fluid flow through the entire length of the core, the core walls must be sealed. This confinement is achieved by coating the core walls with glue, and afterwards adding a thick (~5 mm) epoxy layer. This provides a strong confinement that prevents liquid flow through the walls of the core, and helps to protect the core from damage and allows the core to be placed securely inside the core holder. A schematic is provided in Figure 21, a picture of the core-holder inside the oven is given in Figure 22.

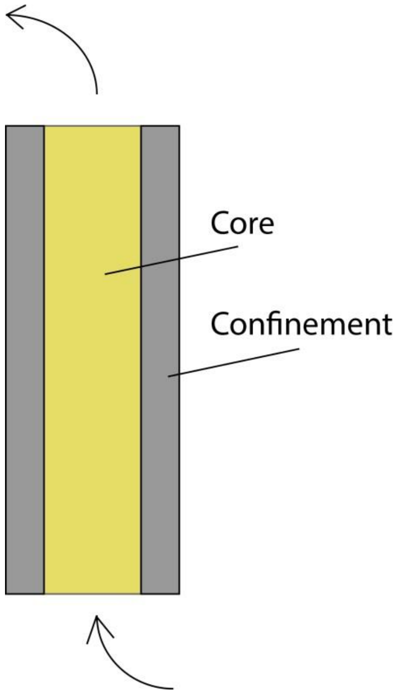

Figure 21: schematic of core and wall confinement

When a core is installed it has to be prepared for experiments. If the core has already been used for another experiment this means it has to be cleaned and remaining foam has to be removed. This is done by injecting a foam killer, in this case 2-propanol (IPA) diluted with demi water. IPA breaks down lamellae and prevents the formation of new ones. Nonetheless, removing trapped foam is very difficult.

The next step is to flush the core with CO_2. This is very suitable to push out liquids and dry the core. In addition, IPA is evaporated by flushing with gas. After injecting CO_2 for approximately 10 minutes the system can be vacuumed from the outlet side of the system. As soon as the vacuum is established the core can be saturated with surfactant. During this process the vacuum should be maintained so liquid is guaranteed to be able to saturate the whole core. The system is pressurized as soon as it is entirely liquid-filled. CO_2 flushing pushed out all other gasses in the system. As CO_2 has a high solubility, increasing the pressure will help dissolve gasses in the liquid phase. It is important to keep the pressure in the back pressure and in the system approximately equal, as a large pressure differential can damage the membrane sealing the system. The core is fully filled with a noncompressible fluid (liquid), so with a continuous circulation of liquid, the pressure can be increased at any rate as long as there is liquid flowing out of the system.

The experiments conducted under steady-state conditions, study the effect of varying foam quality on foam strength. The influence of any other parameter should be minimized to clearly see the effect of the variable that is being studied. One of the variables that influences foam strength is surfactant concentration. In a virgin core surfactant adsorbs on the grain surface until an equilibrium is reached. For a steady-state experiment it is important this equilibrium is reached before the measurements are taken. An injection of approximately 20 pore volumes of surfactant with the surfactant concentration that will ultimately be used should now be injected. Carbonate cores require a much larger volume of surfactant to be injected. In this study, 100 pore volumes had to be injected before a steady-state was observed. When this is complete, the core preparation for a steady-state experiment is completed. How achieving a surfactant-saturated core was verified is explained in the next section.

Figure 22: Picture of core holder inside oven

4.2.1 Verification of surfactant adsorption

There are two methods to verify if the core has been fully saturated with surfactant:

- Measure surface tension or total organic carbon (TOC) in affluent
- Observe steady-state pressure drop

Both methods have been applied during this study. A measurement of the surface tension gives information on the amount of the surfactant in the solution. This can be compared to the initial amount of surfactant. Steady-state has been achieved if the surfactant concentration in the original solution and affluent are equal. This method can only be applied when the surfactant concentration is at or below CMC. If the concentration is above CMC the TOC in the affluent can be measured and compared to the original solution.

Another method to observe if the adsorption of surfactant has achieved a steady-state is by observing the pressure drop while foam is injected. When the core is fully surfactant-adsorbed the pressure drop is constant over time.

4.2.2 Core types

In this study three different core types are used: Bentheimer Sandstone core, ‘Mergel’ Chalk and ‘Estaillades’ Limestone. XRD analysis is performed on these cores to determine the mineral contents, of which the results are provided in the next section.

4.2.2.1 Bentheimer Sandstone

#	**Compound name**	**Concentration**
1	Al_2O_3	1,931
2	CaO	0,208
3	Cl	0,02
4	Co_3O_4	0,001
5	Cr_2O_3	0,005
6	Fe_2O_3	0,172
7	K_2O	0,827
8	MgO	0,064
9	Na_2O	0,022
10	NiO	0,002
11	P_2O_5	0,03
12	PbO	0,003
13	SO_3	0,02
14	SiO_2	96,616
15	SrO	0,002
16	RiO_2	0,072
17	ZnO	0,002
18	ZrO_2	0,004

Table 6: Bentheimer Sandstone consituents

4.2.2.2 Mergel Chalk

The researchers investigating the Mergel core specifically searched for clay components. In their research they did not find any evidence of clay inside the sample. However, the presence of clay inside the Chalk is highly disputed.

#	Compound name	Concentration
1	$CaCO_3$	84,5
2	$MgCO_3$	15,5
3	SiO_2	0

Table 7: Mergel Chalk constituents

4.2.2.3 Estaillades Limestone

#	Compound name	Concentration
1	$CaCO_3$	97
2	$MgCO_3$	3

Table 8: Estaillades Limestone constituents

4.3 The nanoparticle

Removed due to confidentiality.

#	Compound name	Concentration (wt%)	Absolute error (%)

Table 9: contents removed due to confidentiality

4.3.1 Nanoparticle Preparation

Removed due to confidentiality.

Figure 23: Removed due to confidentiality.

Figure 24: Removed due to confidentiality.

Removed due to confidentiality.

Component	Type
Mill	Retsch PM 100 CM
Ultrasonic transducer	Hielscher UIP1000hd

Table 10: equipment for nanoparticle preparation

4.4 Surfactant carriers

In this study experiments have been performed with different surfactant carriers, i.e. seawater, a calcium chloride solution and demineralized water. This section explains how these solutions are prepared, and why they are used.

4.4.1 Artificial seawater

The consideration to choose for saline water is very practical. Not only because it is readily available (especially in offshore fields), but also because water that is already present in a reservoir is often saline. As ions can be very important for the stability of nanoparticle dispersions as well as surfactant behaviour it should be considered to assess the validity of the nanoparticle for real field-scale applications.

The precise concentration of seawater varies across the globe. The average composition of seawater actually consists of a very large number of salts (Lyman & Fleming, 1940). The six most common salts are used for seawater preparation in this study as displayed in Table 11.

Solution	Salt	Concentration [g/L]
1	NaCl	23,926
	Na_2SO_4	4,008
	KCl	0,677
	$NaHCO_3$	1,196
2	$MgCl_2 \cdot 6H_2O$	10,636
	$CaCl_2 \cdot 2H_2O$	1,4598

Table 11: constituents for artificial seawater

As Lyman and Fleming have indicated, the interaction between different salts might cause precipitation at high salt concentrations. To prevent (local) high concentrations and therefore precipitation, they suggest creating two different solutions (as indicated in Table 11) and slowly mixing after all salts have been dissolved. When creating the seawater is complete, surfactant can be added as desired. As has been mentioned earlier it is important to eliminate influences from any variable other than the investigated one on the output of our measurements. Therefore it is preferential to make seawater in large quantities so small salt concentration differences do not influence the experiments.

4.4.2 Calcium chloride solution

One of the concerns regarding surfactants is their reactivity with some ions present in seawater. For the AOS surfactant used in this study calcium is known to have some interactions, as it can replace the sodium ion in the surfactant molecule. In order to isolate the effect of calcium molecules on the surfactant behaviour from the effect of other ions present in seawater, a solution is made with $CaCl_2$ in demi water. The concentration of Ca^{2+} is roughly 0.4 w%.

4.4.3 Demineralized water

The preparation of demineralized water requires no explanation. Despite not being a surfactant carrier that would be considered for a field-scale application, demi water is very useful in a laboratory environment. As has been explained, ions present in a solution can have a detrimental effect on the stability of colloidal dispersions. There are techniques to neutralize the effect of ions, but these are not required when working with demi water. Therefore, demi water is very convenient when working with nanoparticles, as dispersion stability is less of a concern.

4.5 Surfactants

The experiments are typically conducted using a surfactant concentration around CMC. The surface tension of each surfactant was measured for different surfactant concentrations to determine CMC.

4.5.1 BIO-TERGE AS-40

This surfactant is also referred to as AOS 14-16. This is an aqueous solution of sodium olefin sulfonate, which contains 40% active components. The CMC for AOS 14-16 is measured for 4 different liquid phases:

- Tap water
- Demineralized water
- Demi water + 1% $CaCl_2$
- Artificial seawater

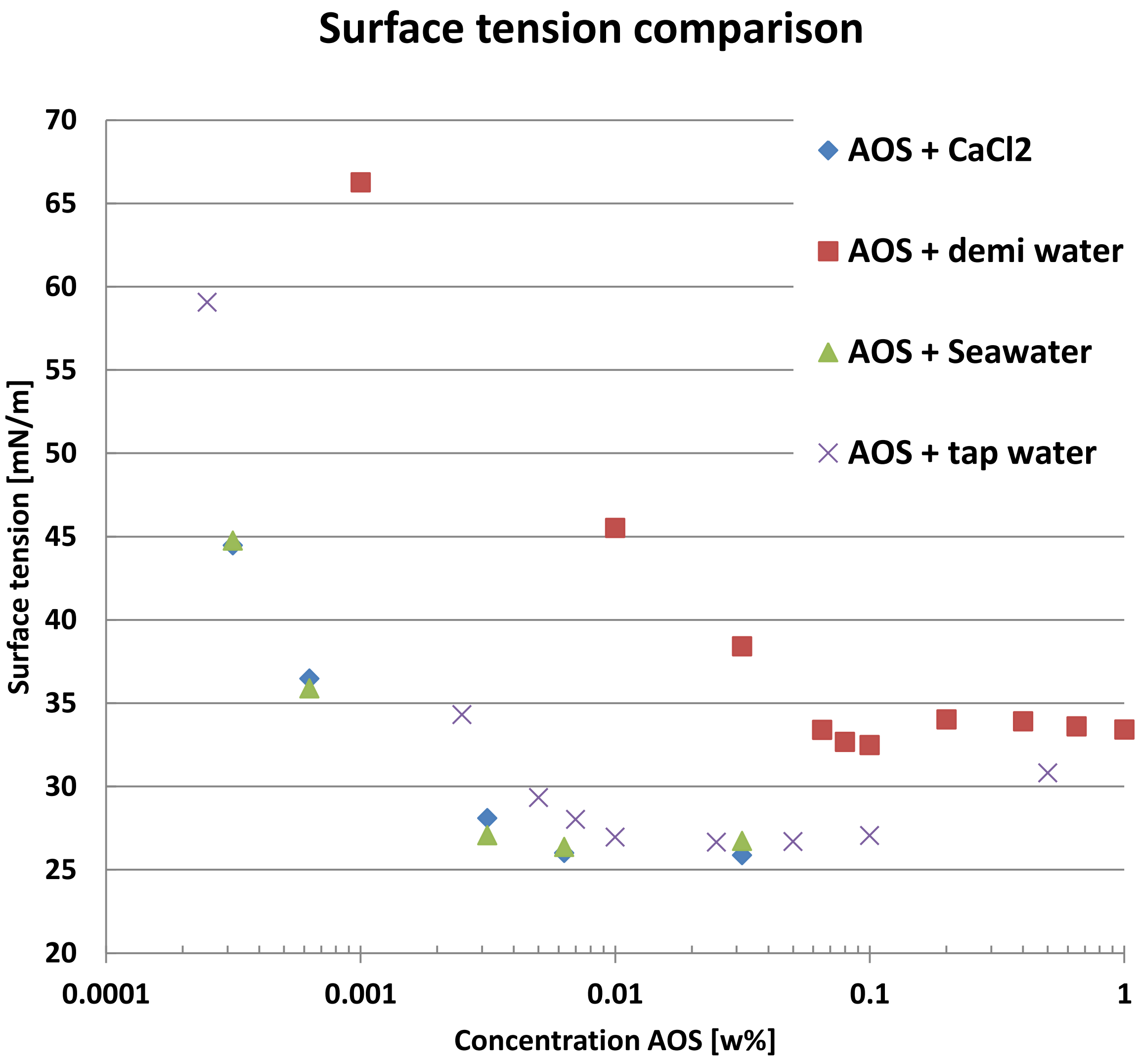

Figure 25: CMC of AOS 14-16 in various liquid types

In Figure 25 an overview is given of the measurements performed for these four scenario's. The CMC can be determined as explained in section 2.1.2.1 by finding the intersection between the negative slope and horizontal line. For AOS in demi water, the CMC is around a concentration of 0,08 wt%. In the other cases both the CMC as well as the surface tension at that CMC is lower. For tap water CMC occurs around 0,01 wt% and this is even slightly lower for seawater or 1% $CaCl_2$. There appears to be no or little difference between the cases of seawater and 1% $CaCl_2$.

4.5.2 AMMONYX CETAC-30

This is an aqueous solution of cetyl trimethyl ammonium chloride containing 30% active components. The trimethyl head group of the surfactant is positively charged. This causes this surfactant to be a more suitable than the (negatively charged) AOS 14-16 when dealing with oil-wet carbonates, as the carbonate surface is generally positively charged. When using a surfactant of the opposite charge, this will cause a large amount of additional adsorption. Since Ammonyx has an equal charge this will aid in the reduction of adsorption issues.

5 Results

This chapter presents the experimental results. Both the raw measurements and the processed results are provided. In cases where the experimental outcome was not satisfactory, the adjustments to the followed method are given in order to enhance the setup. Data on the following experiments is provided in this section:

- Low pressure & temperature core flooding
- High pressure & temperature core flooding
- Nanoparticle experiments
- Bulk foam experiments

First information is provided on the basic calculations that are required prior to conducting the experiments. This procedure is equal for high- and low pressure experiments. For each experiment the result of the fitting procedure is given. The second section contains information obtained from static bulk foam experiments.

5.1 Core flooding measurement processing

Low-pressure core flooding experiments are conducted using setup 1 (4.1.1), and high pressure core flooding experiments are conducted using setup 2 (4.1.2). The detailed procedure to process the measurements has been explained in sections (2.4.1) to (2.4.4).

For both cases the apparent viscosity of the injected foam is calculated using Darcy's equation. This is done by converting the pressure drop for every foam quality. The result is a set of different viscosities for the range of foam qualities. By applying the procedure presented in section 2.4.4, these points are fitted to a local-equilibrium model of CMG-STARS. The MATLAB scripts which are used in this study can be found in Appendix A – MATLAB scripts. The first script converts measurements to apparent viscosities. The second script fits the viscosities to the CMG – STARS model.

The total volumetric flow rate inside the core is fixed for each experiment, and is constant when changing foam quality. Two factors influencing volumetric flow should be taken into account in the experiments, which are the compressibility and solubility of the gasses.

5.1.1 Compressibility

For all gas flow controllers described in section 4.1, the gas flow is set by a volumetric value at standard or normal laboratory conditions, e.g. atmospheric pressure and 0˚C. Experiments are conducted under different conditions. The volumetric gas flow rate at core conditions is determined by multiplying the gas fraction with the total flow rate. The translation from the gas flow rate at core conditions to the gas flow rate at normal conditions is made using an Equation of State (EOS). A different EOS is available for CO_2 and N_2. In case of the former, Span & Wagner is applied, and in case of the latter Jacobsen Stewart is applied.

The application of an EOS provides an initial estimate for the value to which the gas flow controller should be set, but this does not guarantee the gas fraction inside the core will end up at the desired value. The pressure changes across the core because of the foam generation, therefore the specific volume of gas changes as well. By calculating the real gas fraction inside the core based on the measurement, the range of gas fractions inside the core is obtained. This range is displayed as horizontal blue line in the figures displaying the processed measurements.

5.1.2 Solubility

The gas solubility can be approximated using Henry's Law, which relates the amount of gas dissolved in the liquid phase to the pressure. Henry's Constant (k_H) is a value that relates the amount of dissolved gas per unit volume to pressure. For nitrogen k_H is 0,61 mmol/L/atm, and for carbon dioxide k_H is 34 mmol/L/atm.

Because the pressure inside the core changes, the solubility of N_2 and CO_2 will change with it. For nitrogen this effect is negligible, but for CO_2 the change in solubility should be taken into account. The result of this effect is that the gas fraction at the high-pressure inlet side of the core does not only decrease due to compression, but also due to increased solubility. The model processing the measurements takes this effect into account.

5.1.3 Permeability

Every time a new core is used or a core is cleaned, the permeability is determined. In order to determine the permeability the core should be fully saturated with liquid. The core has to be cleaned, flushed with CO_2, vacuumed, and then saturated with liquid while increasing the pressure. Increasing the pressure causes any CO_2 that is still left to dissolve in the liquid phase. For multiple flow rates the resistance to flow are measured and the permeability is calculated using Darcy's Law. When the average of these experiments is taken, a reliable permeability is obtained.

A reliable result is obtained when no single permeability measurement deviates significantly from the average. This is visualized by plotting all measurements, and see how well they align. Figure 26 displays the alignment for experiment A. The slope of the trend line indicates the average permeability. As can be observed the measurements agree with the average, with only two minor deviations at flow rates of 2 and 4 mL/min. This is due to measurement errors, which are more likely to occur at lower flow rates. Taking the average by only measuring higher flow rates (4 and above) is therefore equally reliable. A good way to verify the validity of the average is by verifying if the trend line would go through the (0;0) point in the graph. A permeability measurement taken with only higher flow rates is displayed in Figure 27.

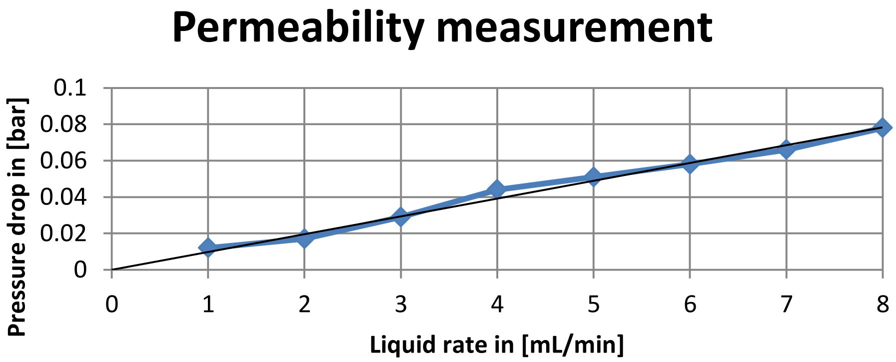

Figure 26: Permeability measurement for experiment A

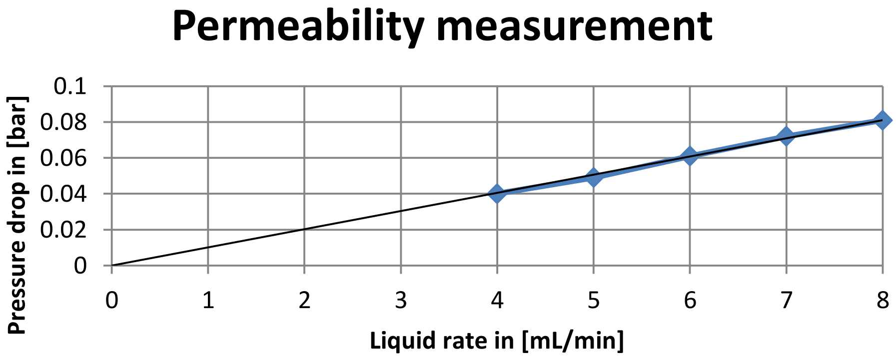

Figure 27: Permeability measurement for experiment E

5.2 Core flooding results

This section gives an overview of the taken measurements and processed results for the low – pressure setup. Section 5.3 gives the processed data for the high – pressure setup. The circumstances under which the experiments were performed are different for each experiment. Table 12 provides an overview of all experimental parameters for each experiment (numbered alphabetically). The parameters include:

Gas phase: The type of gas used to generate foam.
Surfactant: The type of surfactant being investigated, either AOS 14-16 or Ammonyx
Concentration: The weight percentage of surfactant in liquid phase.
Nanoparticle: Indicates if this experiment was conducted with nanoparticles.
Carrier: The liquid phase which was carrying nanoparticles and surfactant.
Core: SST is Bentheim Sandstone. CARB(1) is Chalk, CARB(2) is Estaillades Limestone.
Total flow rate: Foam volumetric flow rate inside the core.
Back pressure: Pressure at the core outlet.
Temperature: Temperature at which the experiment was conducted.
Liquid viscosity: Liquid viscosity associated with the temperature.
Gas viscosity: Gas viscosity associated with temperature and pressure.
Permeability: Measured core permeability.
Running time: Total running time of the experiment.
Time to SS: Typical time required for the system to achieve steady-state conditions.

5.2.1 Experiment overview

Experiment	Gas phase	Surfactant	Concentration [w%]	Nanoparticle	Carrier	Core	Total flow rate [mL/min]	Back pressure [bar]	Temperature [deg C]	Liquid viscosity [cP]	Gas viscosity [E-5 Pa.s]	Permeability [D]	Running time [hrs]	Time to SS [hrs]
A	N2	AOS	0.0315	-	H_2O	SST	1	20	21	0.98	1.7897	2.46	240	12
B	CO_2	AOS	0.0315	-	H_2O	SST	1	10	21	0.98	1.4828	2.03	290	12
C	CO_2	AOS	0.0315	-	H_2O + 1w% $CaCl_2$	SST	1	10	21	0.98	1.4828	1.83	414	12
D	CO_2	AOS	0.0315	-	Seawater	SST	0.5	10	21	0.98	1.4828	2.11	503	24
E	N_2	AOS	0.0315	-	Seawater	SST	0.5	10	21	0.98	1.7739	2.43	393	24
F	N_2	AOS	0.0315	-	Seawater	SST	0.5	80	80	0.355	2.1430	1.86	48	2
G	N_2	AOS	0.0315	-	Seawater	SST	1	80	80	0.355	2.1430	1.86	48	1
H	N_2	AOS	0.1	-	Seawater	SST	1	80	80	0.355	2.1430	1.86	48	1
I	N_2	AOS	0.5	-	Seawater	SST	1	80	80	0.355	2.1430	1.86	48	1
J	N_2	AOS	0.0315	Yes	Seawater	SST	1	80	80	0.355	2.1430	1.86	48	1
K	N_2	AOS	0.0315	-	Seawater	SST	1	80	25	0.893	1.9351	1.78	36	1
L	N_2	AOS	0.1	-	Seawater	SST	1	80	25	0.893	1.9351	1.78	36	1
M	N_2	AOS	0.5	-	Seawater	SST	1	80	25	0.893	1.9351	1.78	36	1
N	N_2	AOS	0.0315	Yes	H_2O	SST	1	80	25	0.893	1.9351	1.78	24	1
O	N_2	AOS	0.0315	-	H_2O	SST	1	80	25	0.893	1.9351	1.78	36	1
P	N_2	AMM	0,05	-	H_2O	CARB (1)	1	80	25	0.893	1.9351	5,51	48	1
Q	N_2	AMM	0,05	Yes	H_2O	CARB (1)	1	80	25	0.893	1.9351	5,51	48	1
R	N_2	AMM	0,05	-	H_2O	CARB (2)	1	80	25	0.893	1.9351	0.097	48	1
S	N_2	AMM	0,05	Yes	H_2O	CARB (2)	1	80	25	0.893	1.9351	0.097	48	1

Table 12: overview of experimental parameters

5.2.2 Experiment A: Nitrogen + 0,0315% AOS 14-16 in demi water

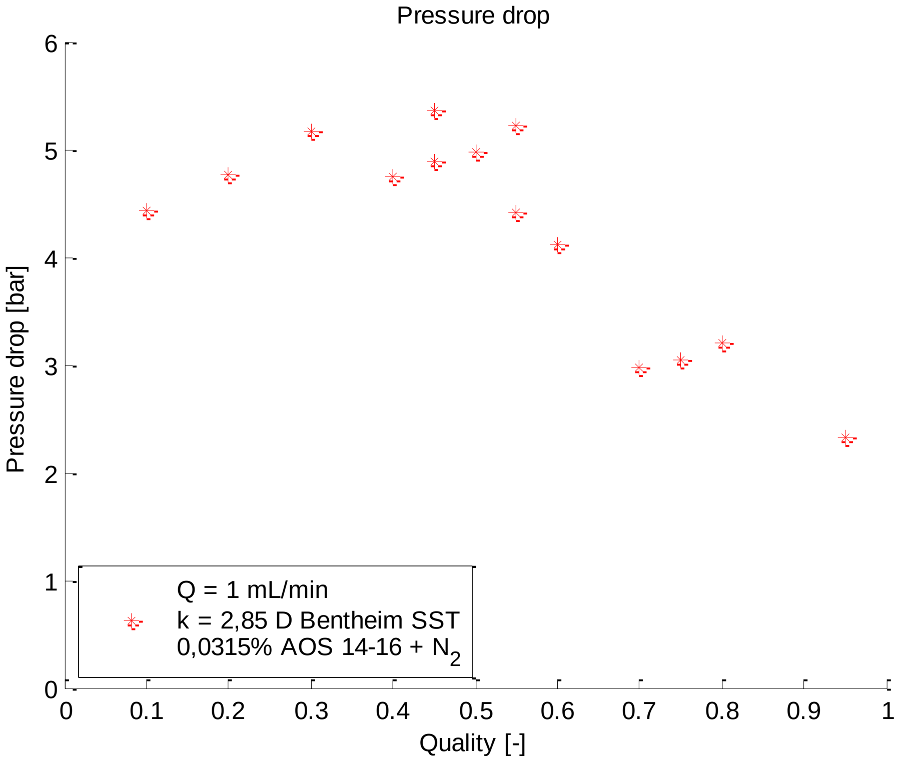

Figure 28: Steady-state pressure drops in experiment A

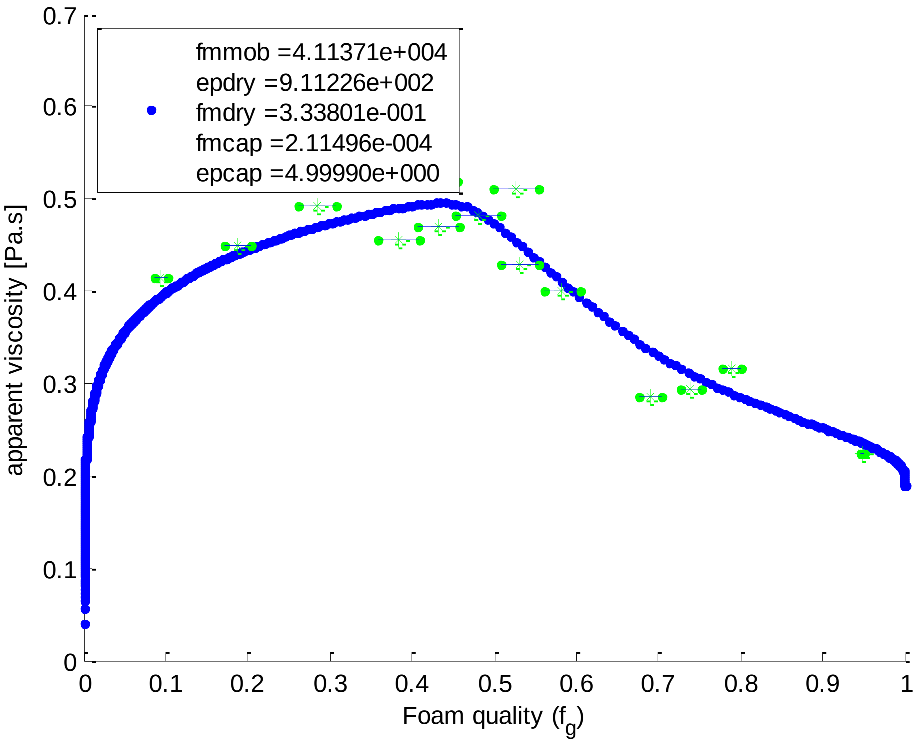

Figure 29: Matching of LE foam model with experiment A

5.2.3 Experiment B: Carbon dioxide + 0,0315 % AOS 14-16 in demi water

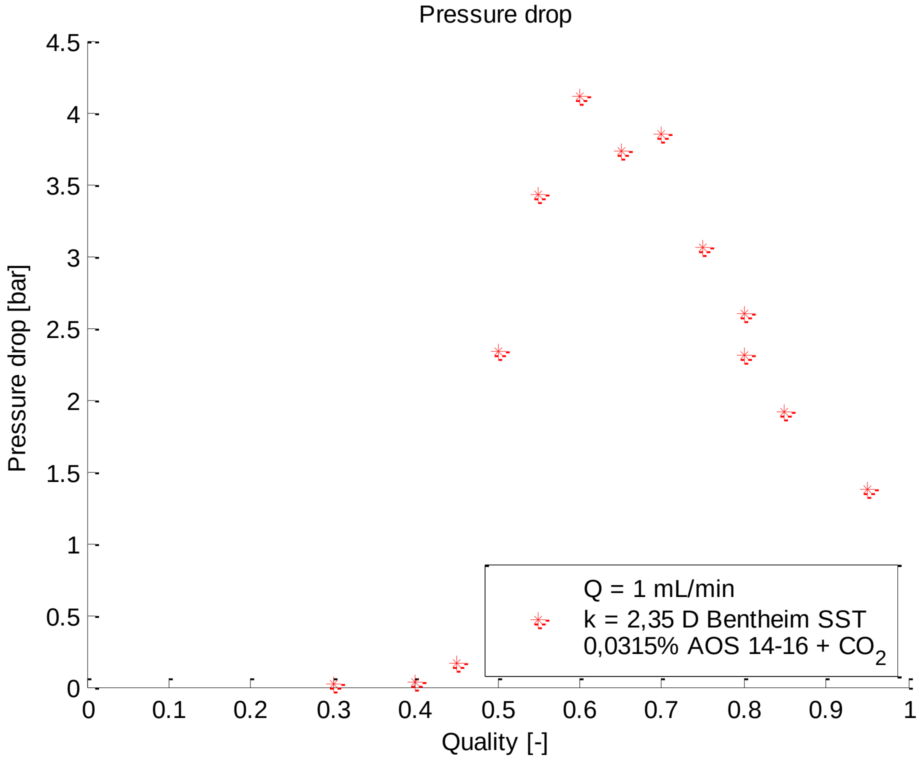

Figure 30: Steady-state pressure drops in experiment B

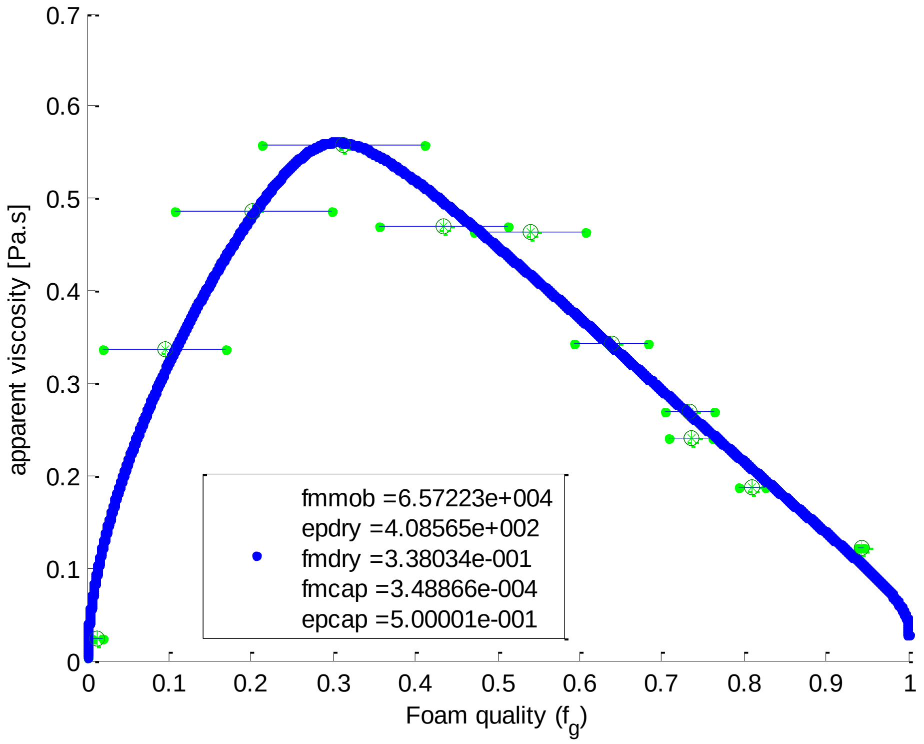

Figure 31: Matching of LE foam model with experiment B

5.2.4 Experiment C: Carbon dioxide + 0,0315% AOS 14-16 in 1% $CaCl_2$ solution

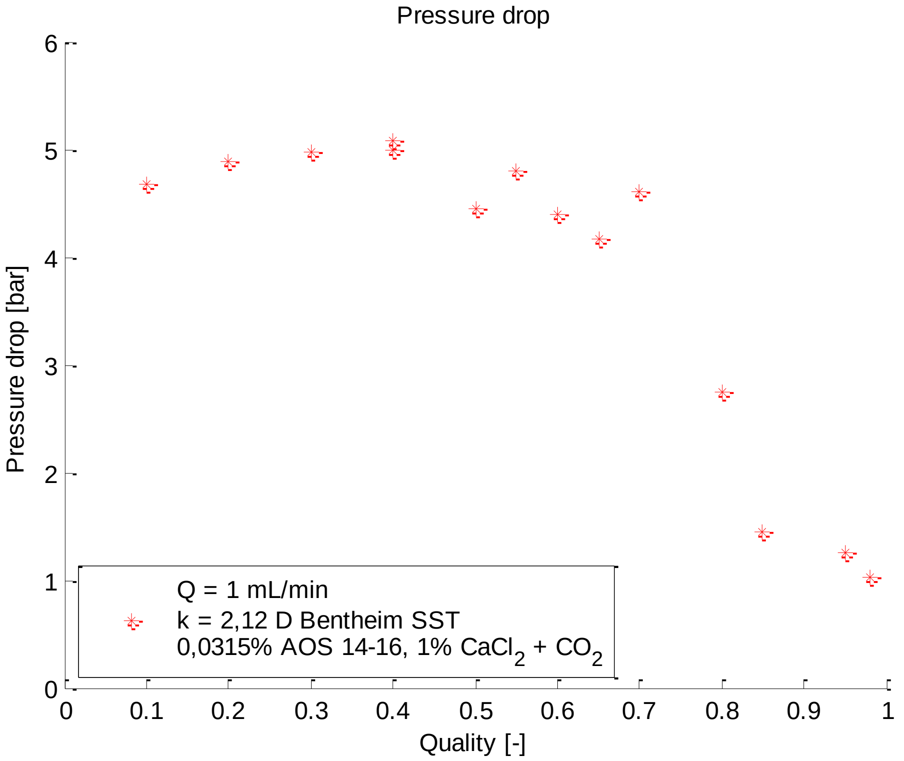

Figure 32: Steady-state pressure drops in experiment C

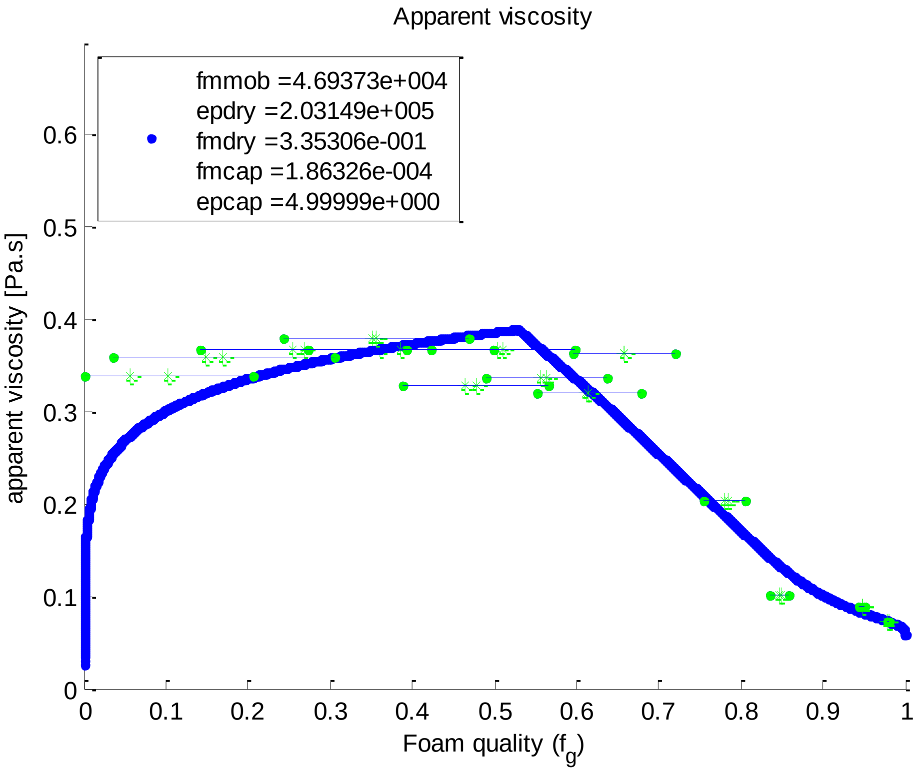

Figure 33: Matching of LE foam model with experiment C

5.2.5 Experiment D: Carbon dioxide + 0,0315% AOS 14-16 in Seawater

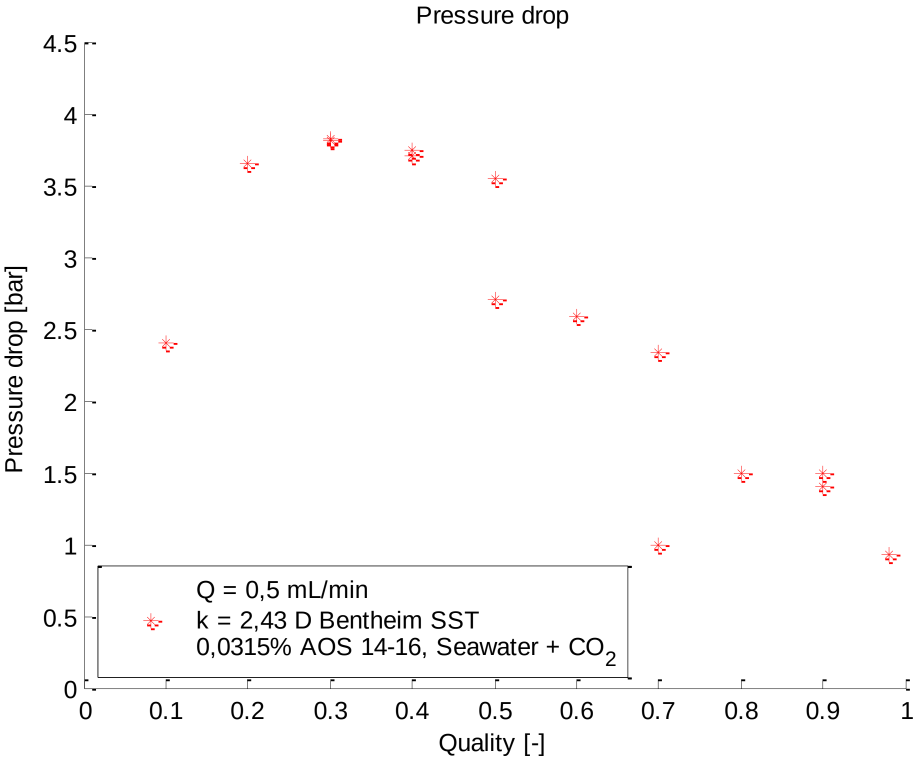

Figure 34: Steady-state pressure drops in experiment D

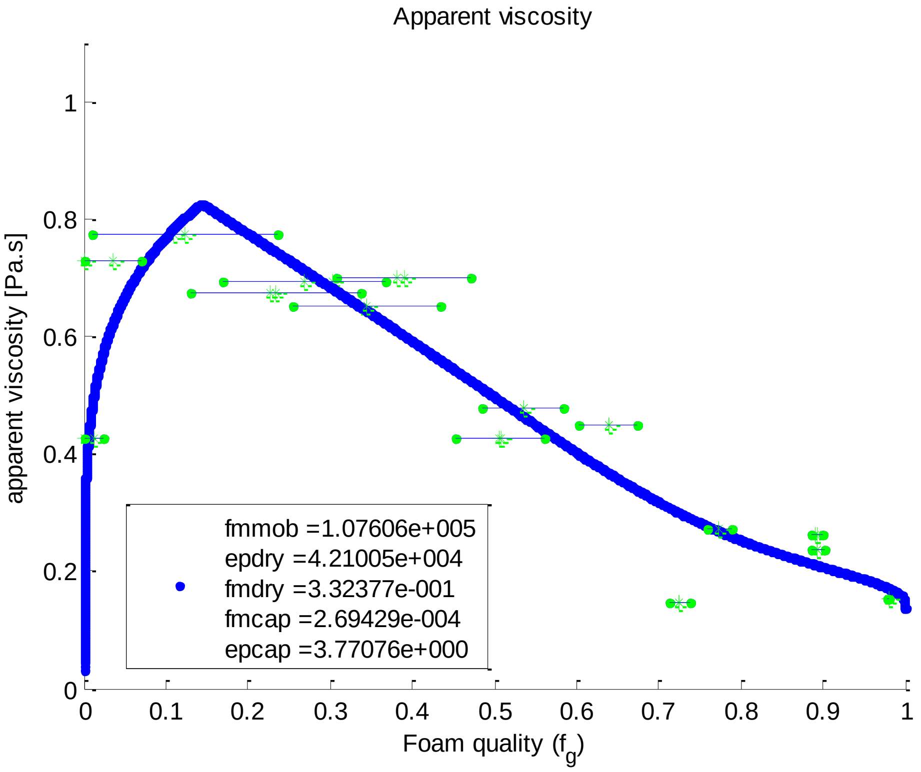

Figure 35: Matching of LE foam model with experiment D

5.2.6 Experiment E: Nitrogen + 0,0315% AOS 14-16 in Seawater

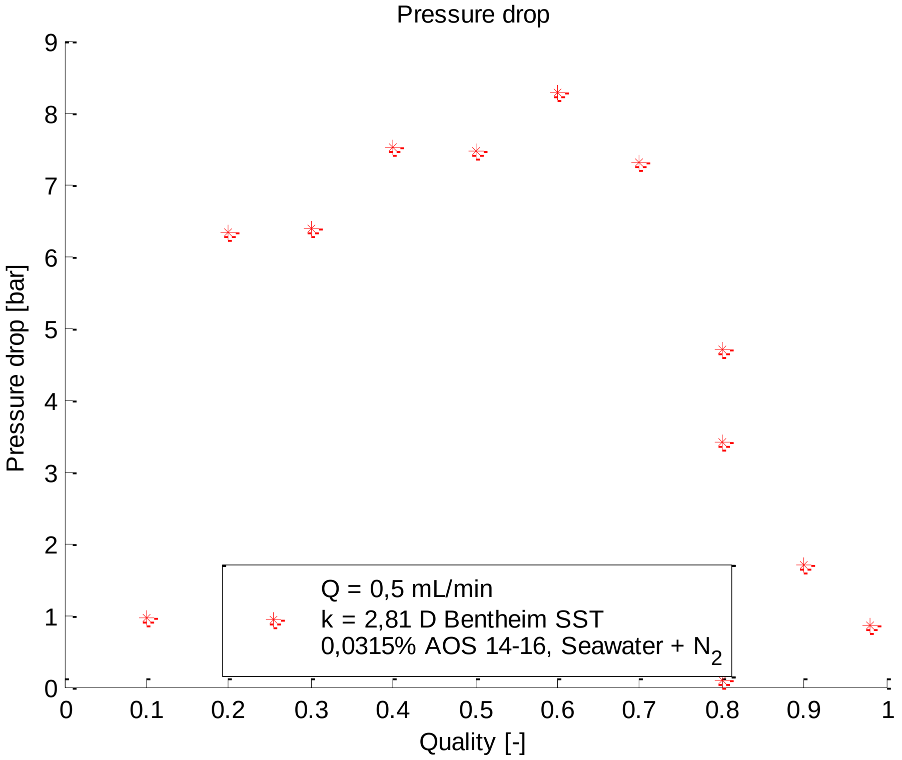

Figure 36: Steady-state pressure drops in experiment E

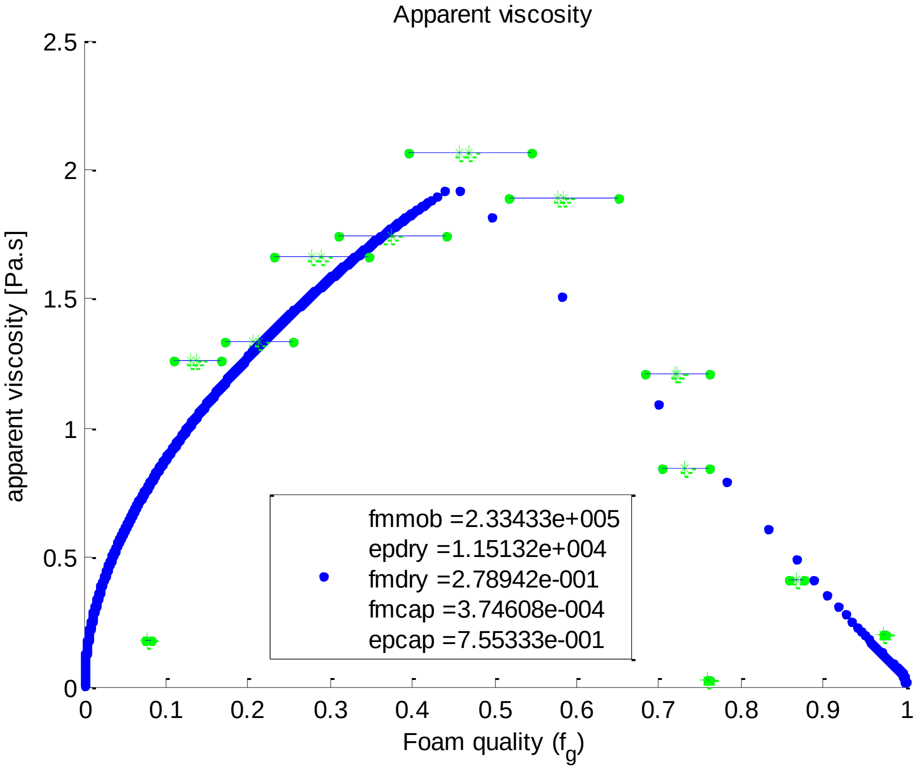

Figure 37: Matching of LE foam model with experiment E

5.3 High pressure core flooding

This chapter provides the results obtained with experimental setup 2. In these experiments the pressure is increased to 80 bar, which causes the quality change over the core to be less than that of the low-pressure experiments. The temperature is either 25C or 80C, as displayed in Table 12.

5.3.1 Experiment F: Nitrogen + 0,0315 % AOS 14-16 in Seawater

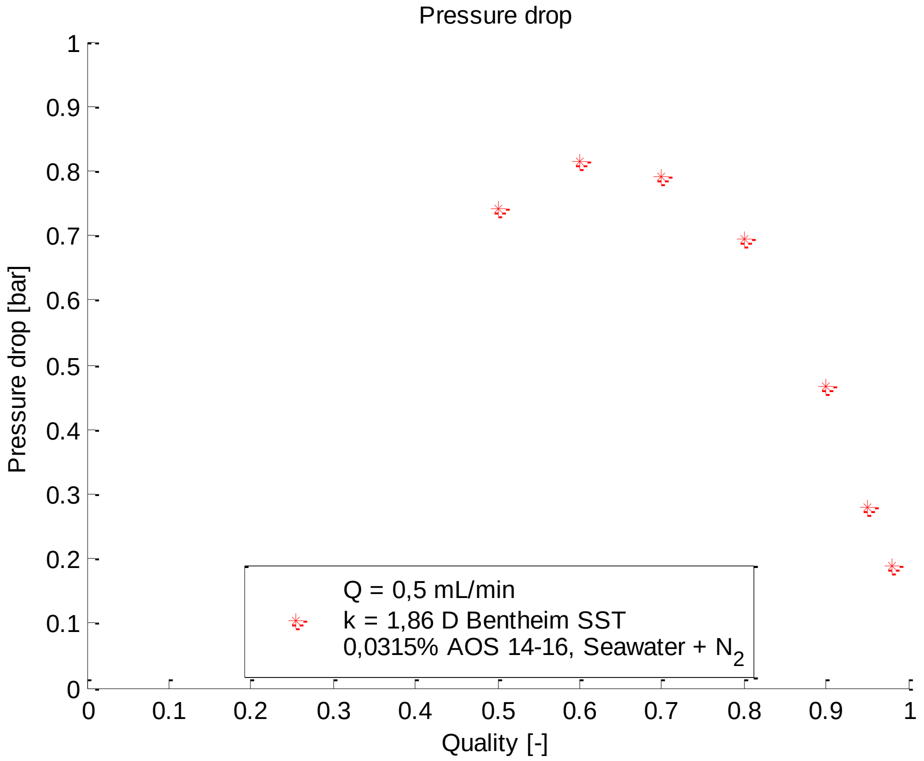

Figure 38: Steady-state pressure drops in experiment F

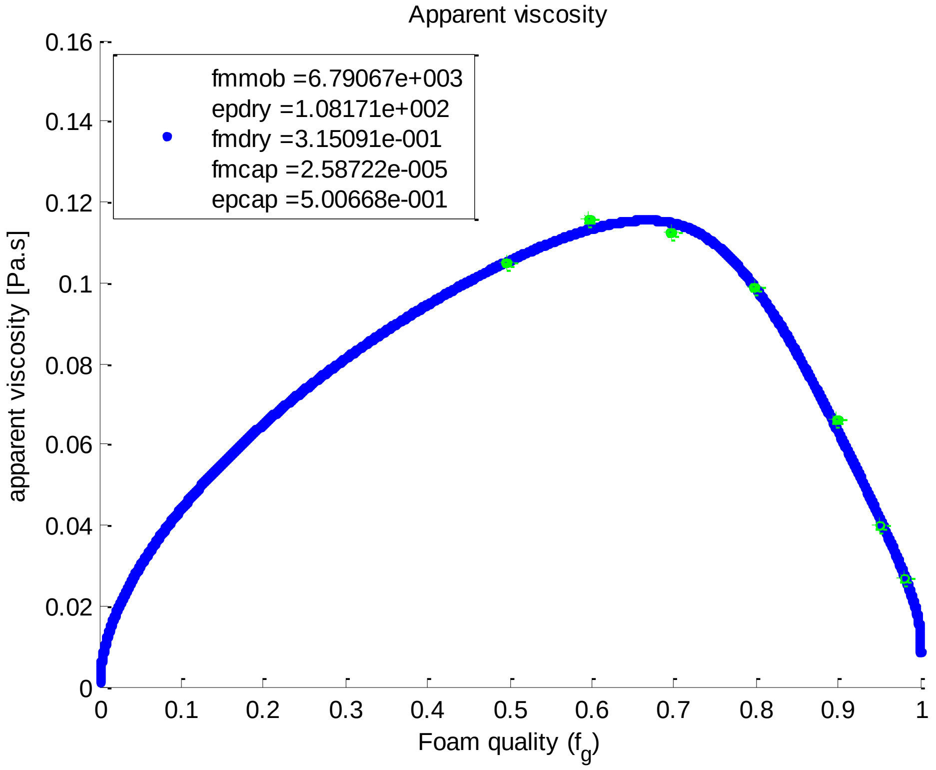

Figure 39: Matching of LE foam model with experiment F

5.3.2 Experiment G: Nitrogen + 0,0315 % AOS 14-16 in Seawater

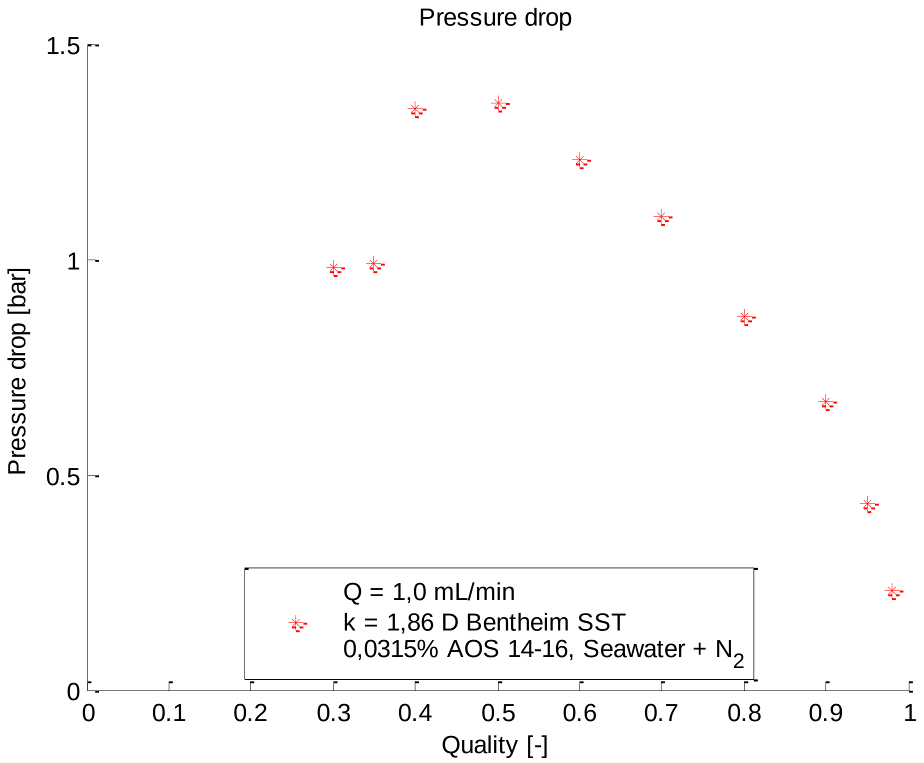

Figure 40: Steady-state pressure drops in experiment G

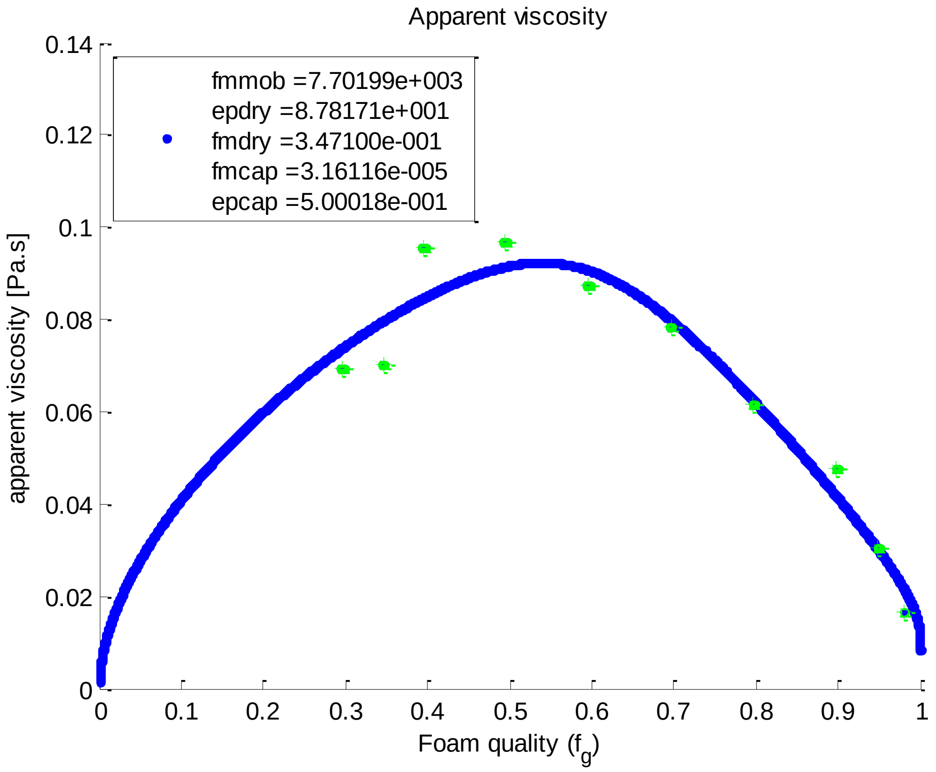

Figure 41: Matching of LE foam model with experiment G

5.3.3 Experiment H: Nitrogen + 0,1 % AOS 14-16 in Seawater

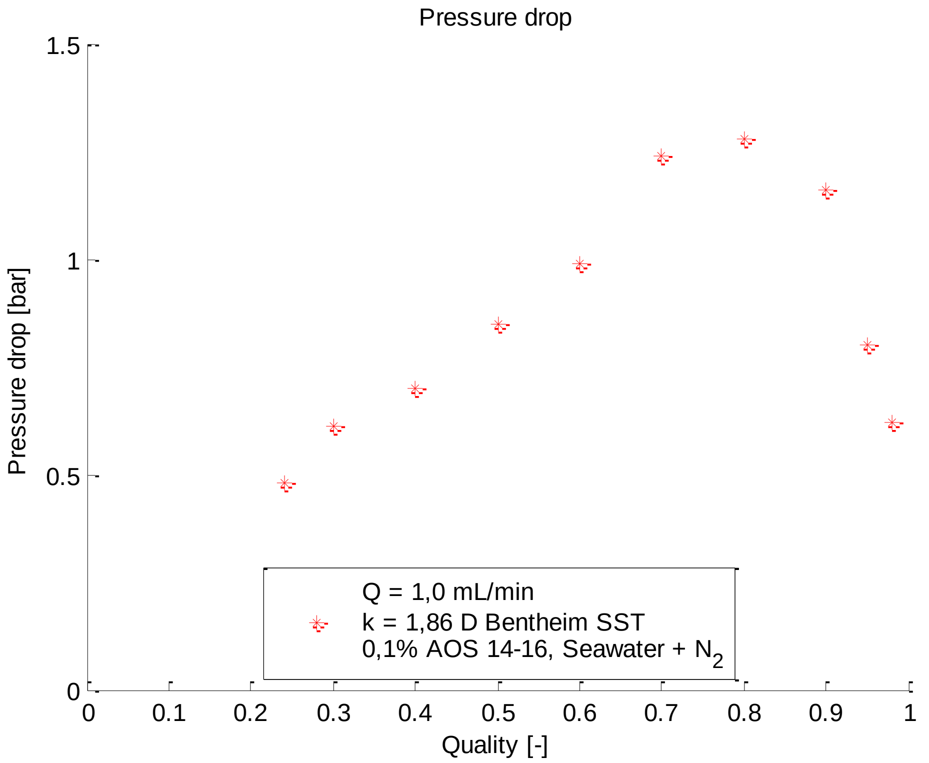

Figure 42: Steady-state pressure drops in experiment H

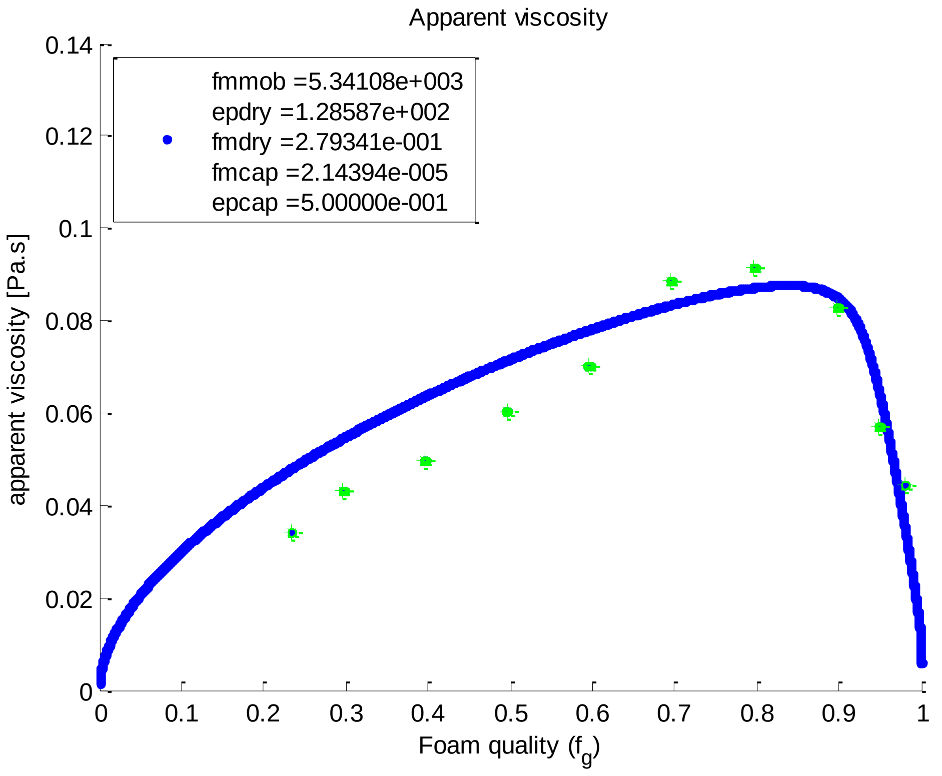

Figure 43: Matching of LE foam model with experiment H

5.3.4 Experiment I: Nitrogen + 0,5 % AOS 14-16 in Seawater

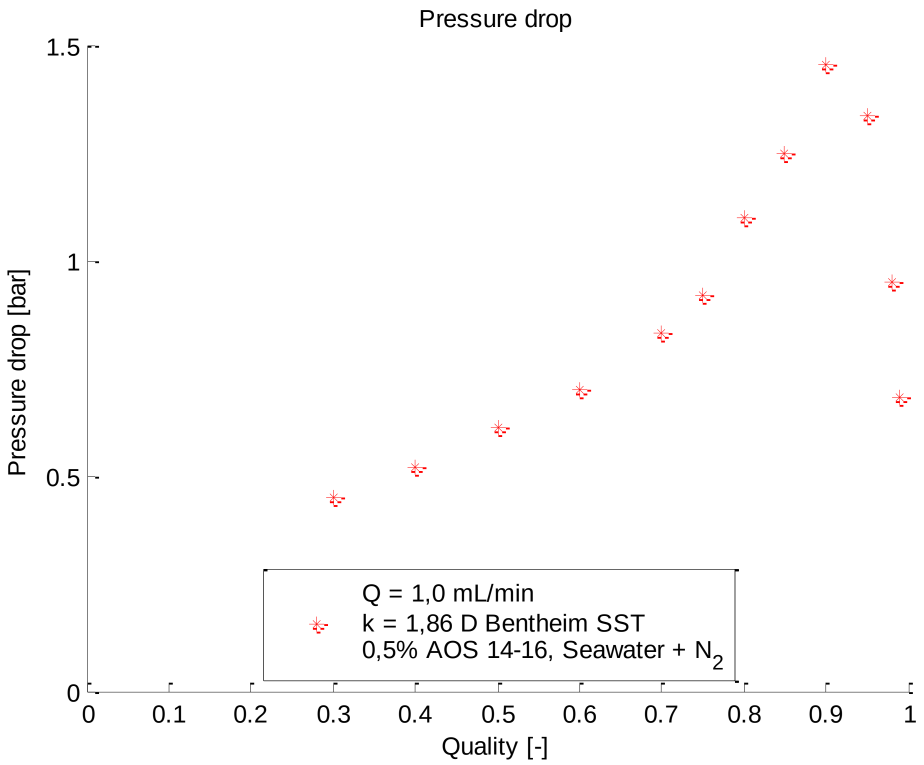

Figure 44: Steady-state pressure drops in experiment I

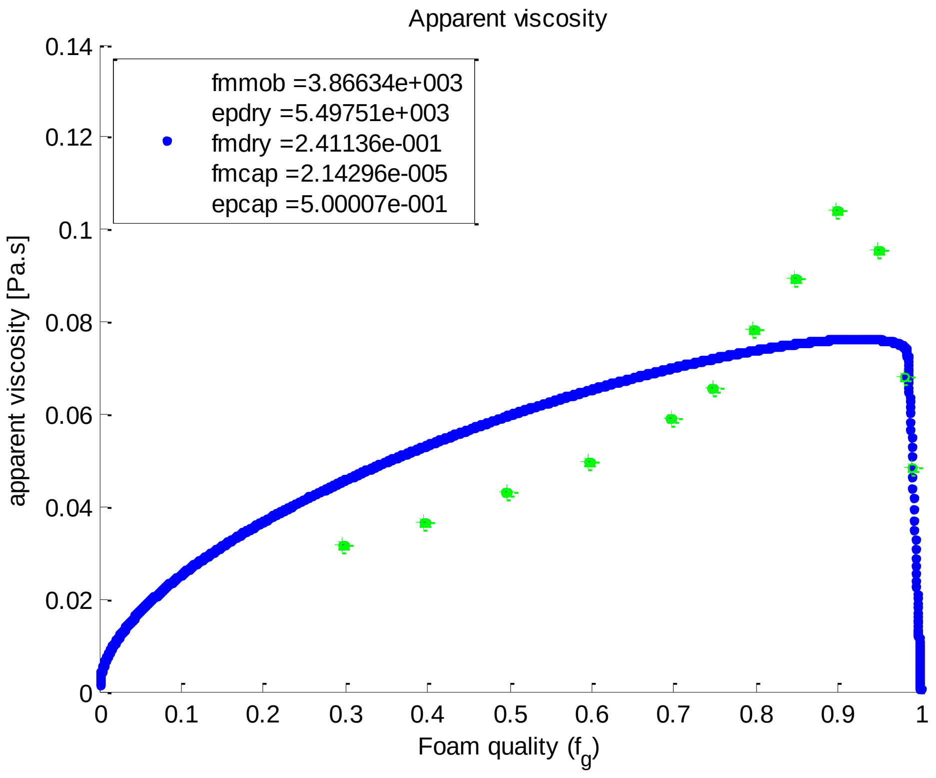

Figure 45: Matching of LE foam model with experiment I

5.3.5 Experiment J: Nitrogen + 0,0315 % AOS 14-16 in Seawater + nanoparticles

The results from this experiment were unsatisfactory. Section 5.4.3 will elaborate on the result and how improvements to the system were made.

5.3.6 Experiment K: Nitrogen + 0,0315 % AOS 14-16 in Seawater

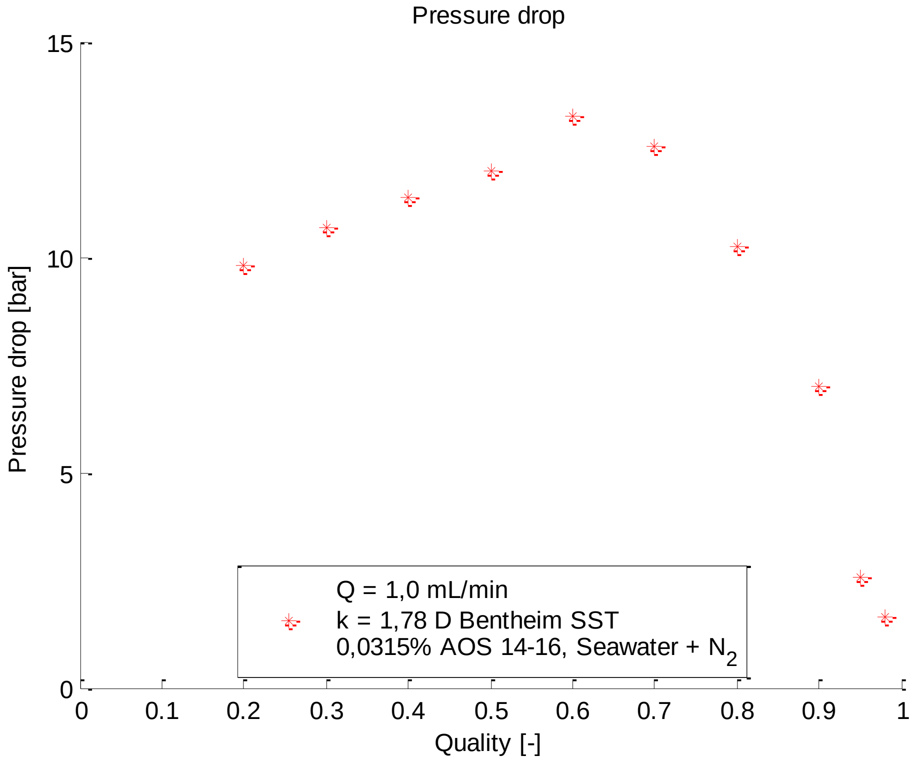

Figure 46: Steady-state pressure drops in experiment K

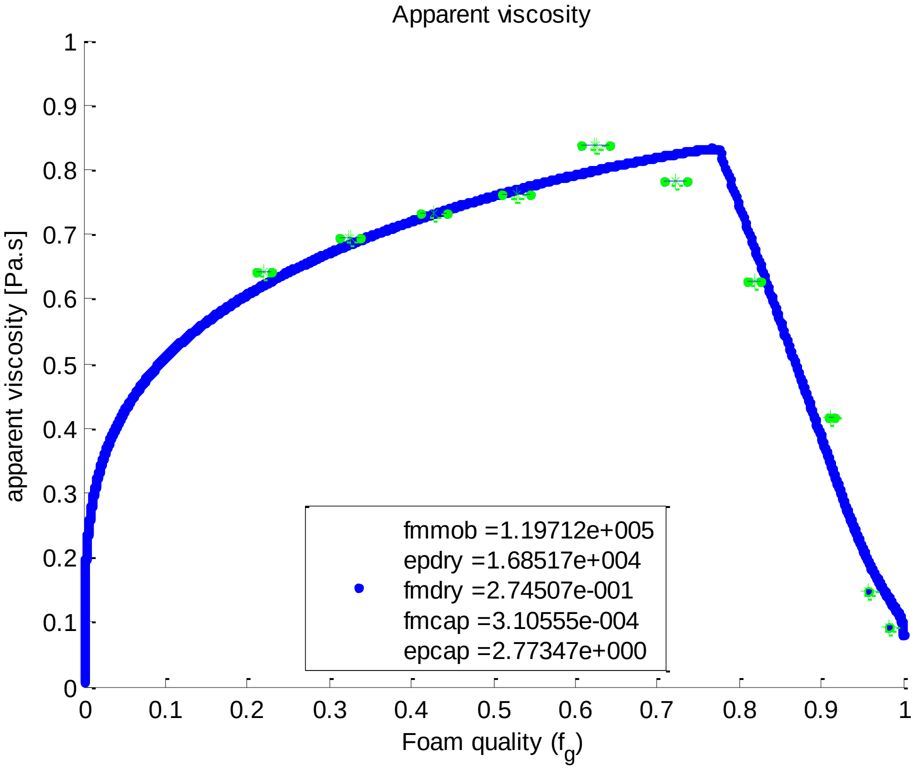

Figure 47: Matching of LE foam model with experiment K

5.3.7 Experiment L: Nitrogen + 0,1 % AOS 14-16 in Seawater

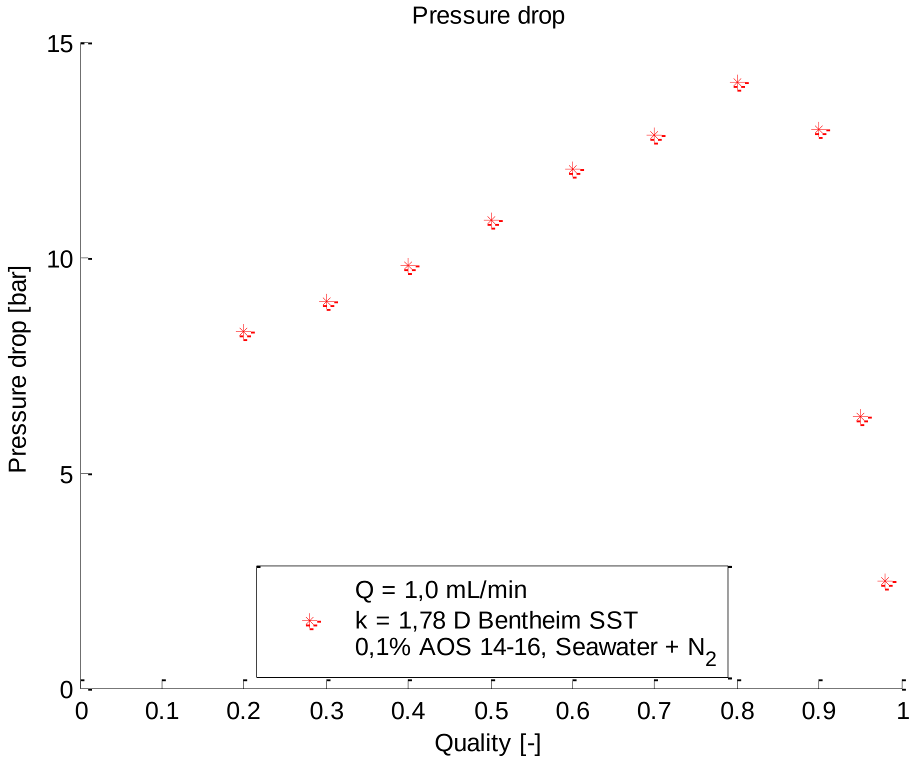

Figure 48: Steady-state pressure drops in experiment L

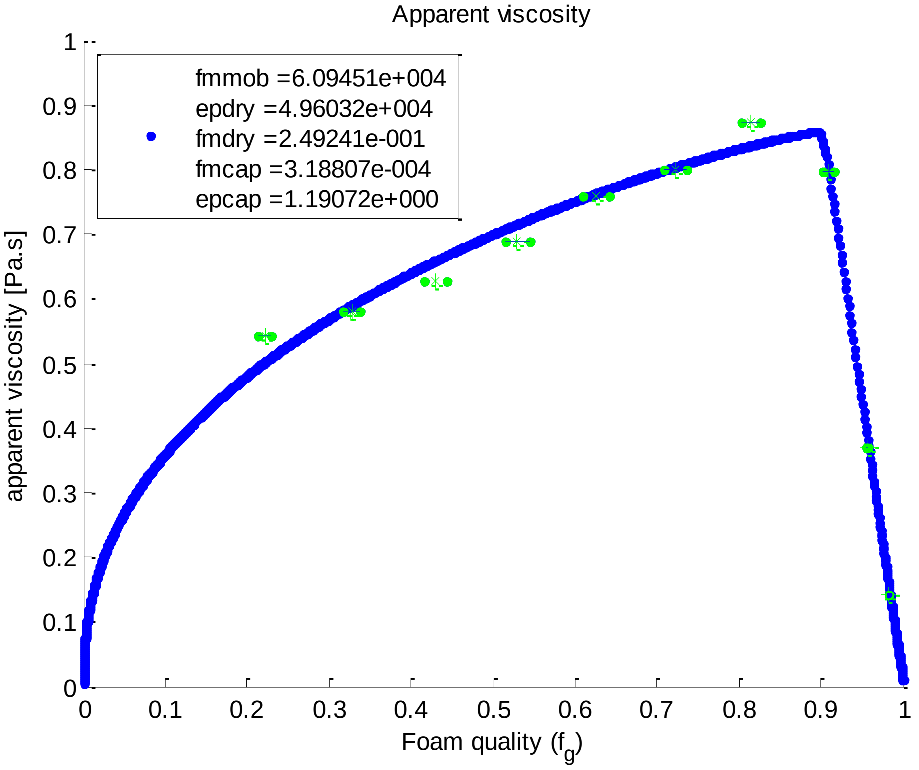

Figure 49: Matching of LE foam model with experiment L

5.3.8 Experiment M: Nitrogen + 0,5 % AOS 14-16 in Seawater

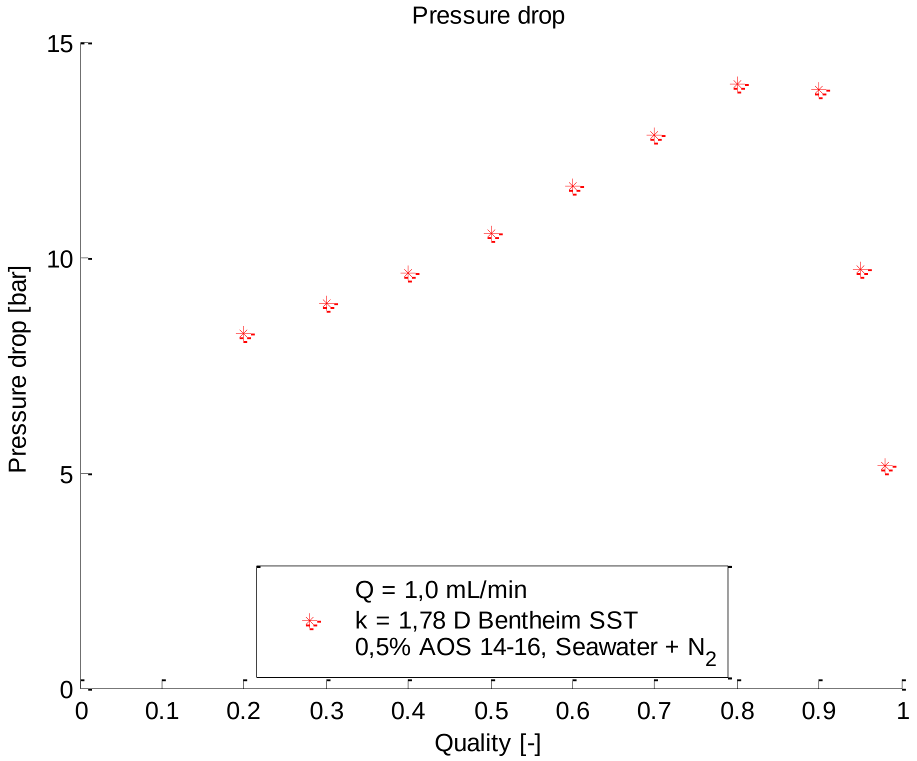

Figure 50: Steady-state pressure drops in experiment M

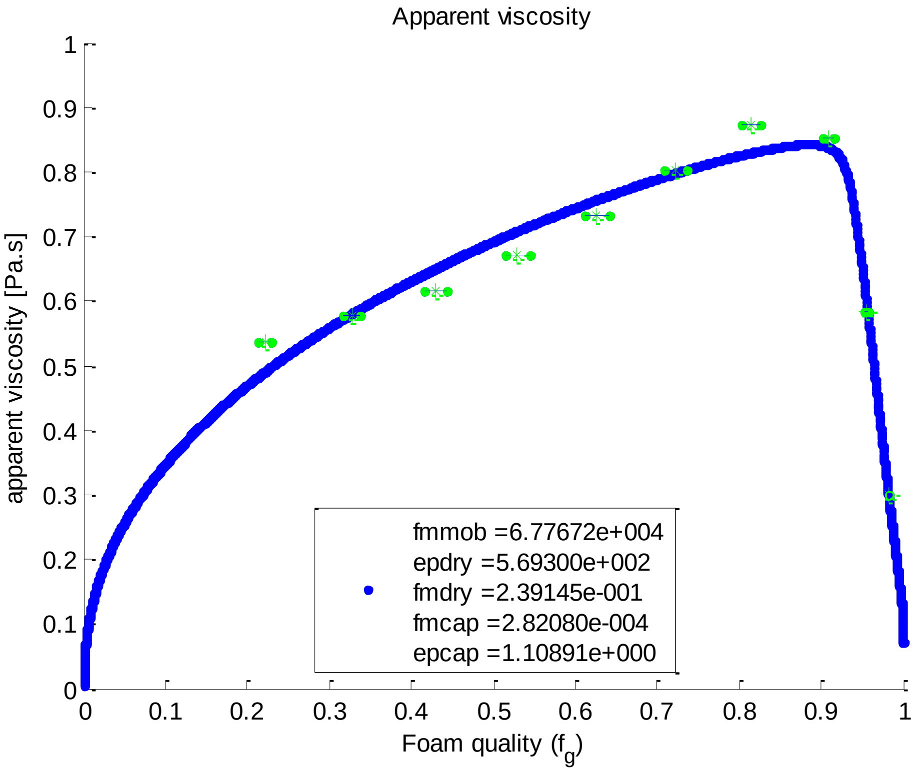

Figure 51: Matching of LE foam model with experiment M

5.3.9 Experiment N: Nitrogen + 0,0315 % AOS 14-16 in demi water + nanoparticles

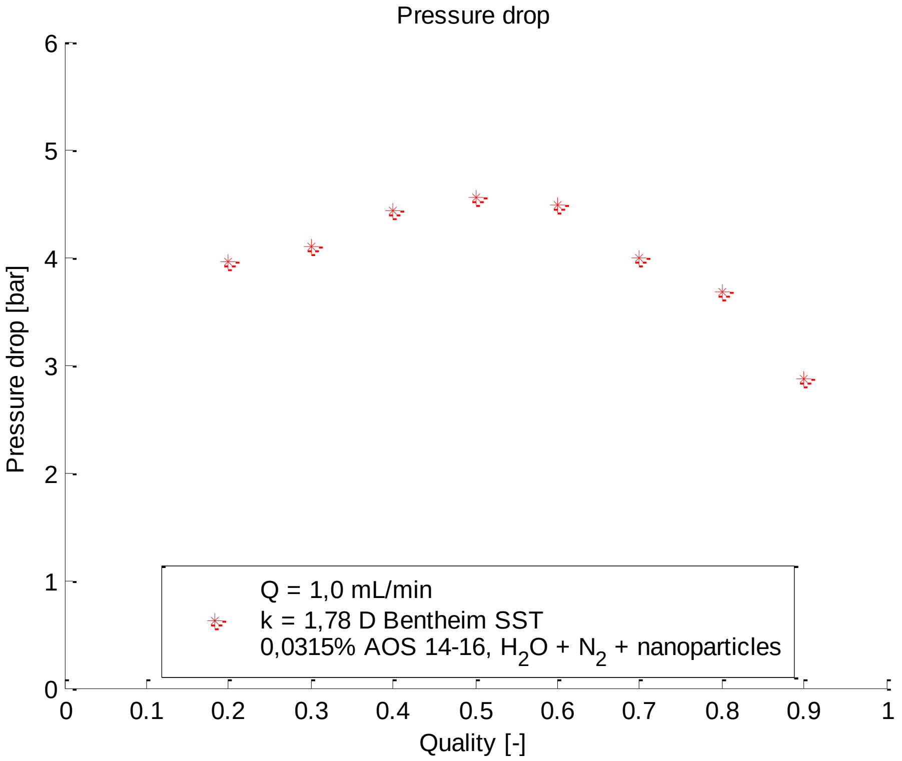

Figure 52: Steady-state pressure drops in experiment N

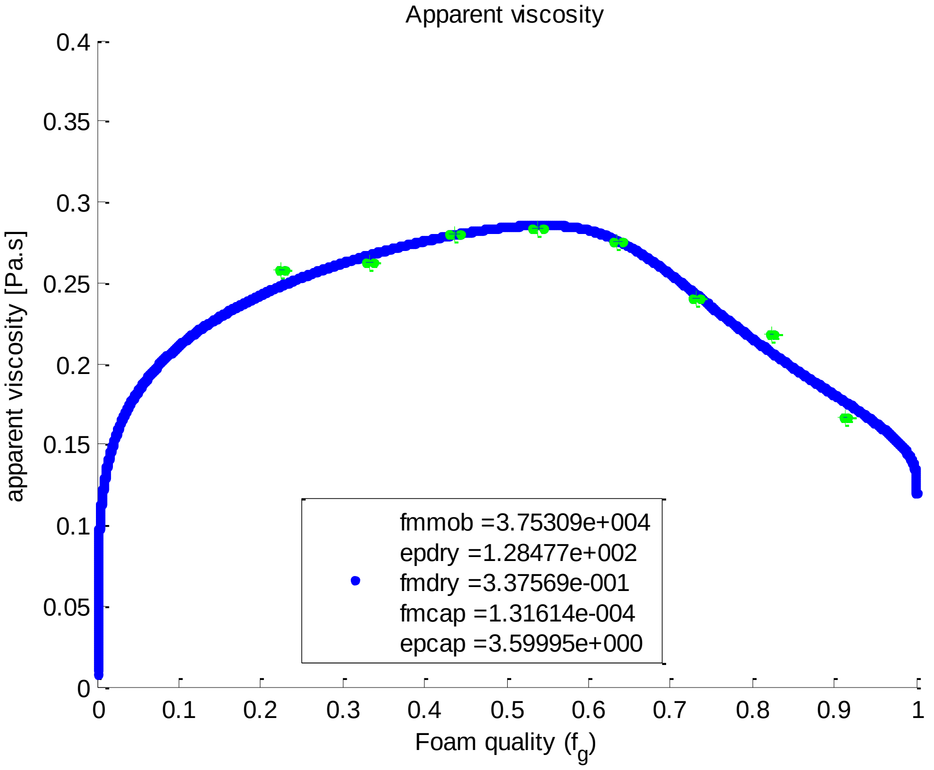

Figure 53: Matching of LE foam model with experiment N

5.3.10 Experiment O: Nitrogen + 0,0315 % AOS 14-16 in H_2O

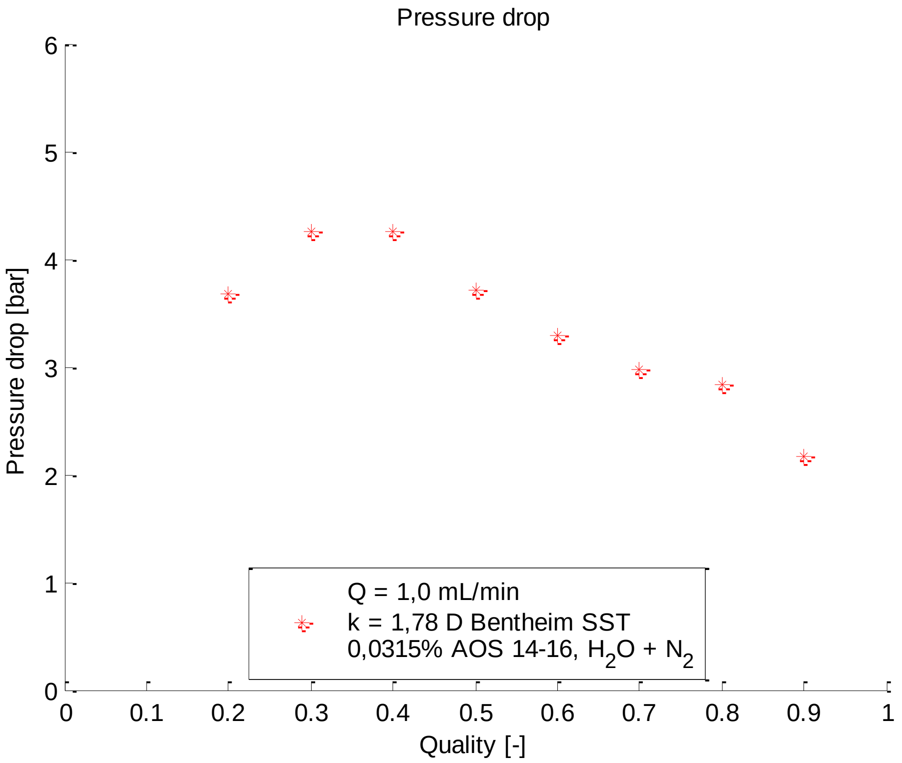

Figure 54: Steady-state pressure drops in experiment O

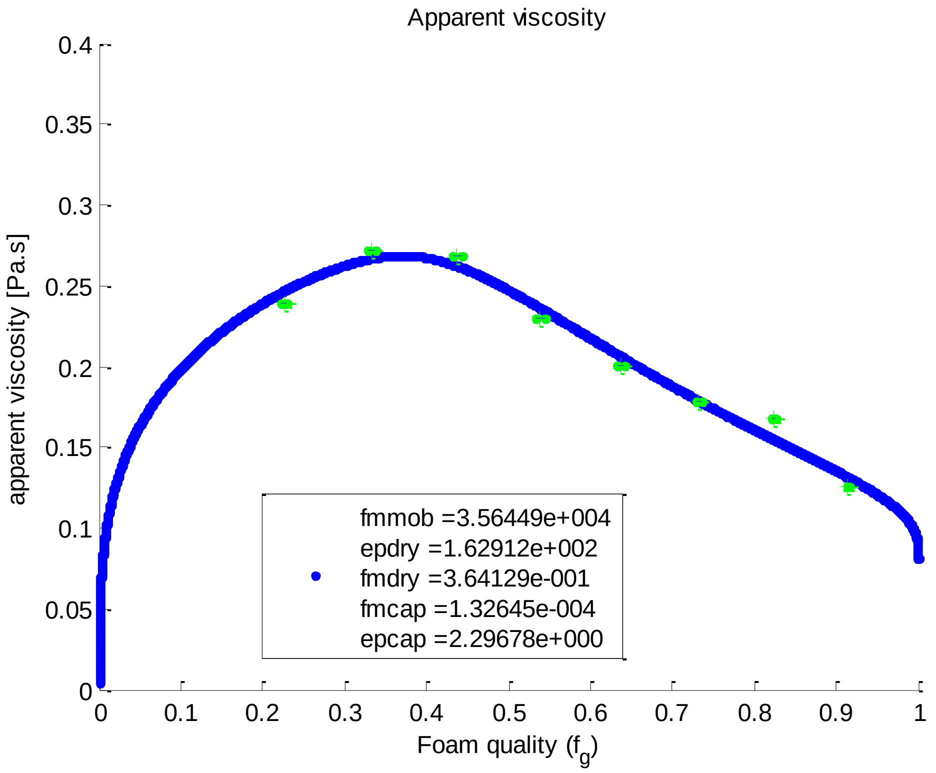

Figure 55: Matching of LE foam model with experiment O

5.3.11 Experiment P: Nitrogen + 0,05% Ammonyx in demi water

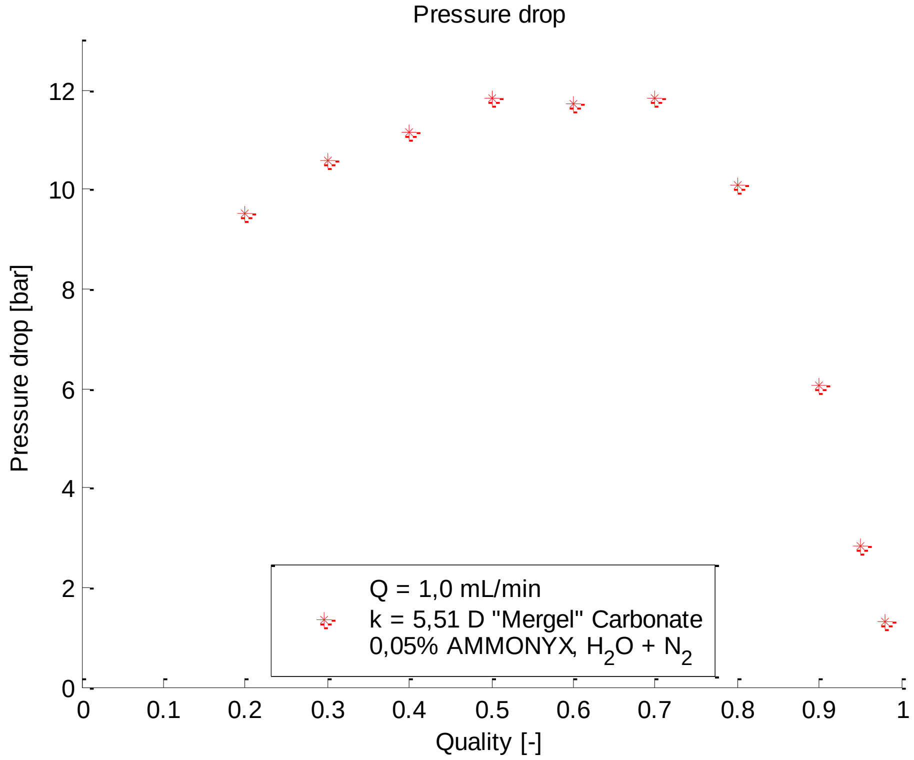

Figure 56: Steady-state pressure drops in experiment P

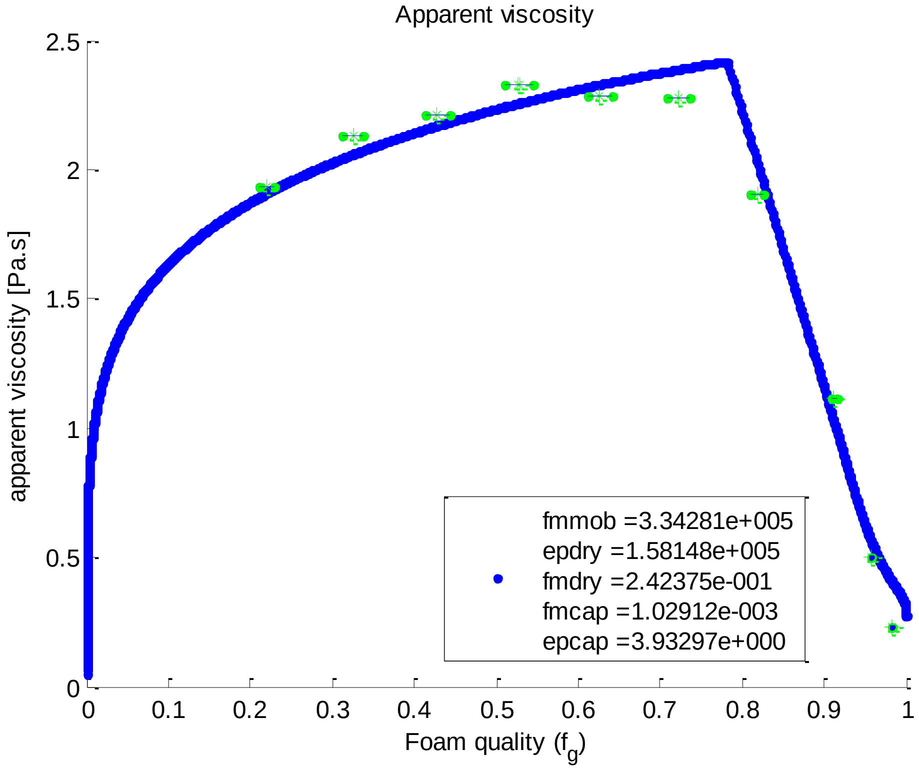

Figure 57: Matching of LE foam model with experiment P

5.3.12 Experiment Q: Nitrogen + 0,05% Ammonyx in demi water + nanoparticles

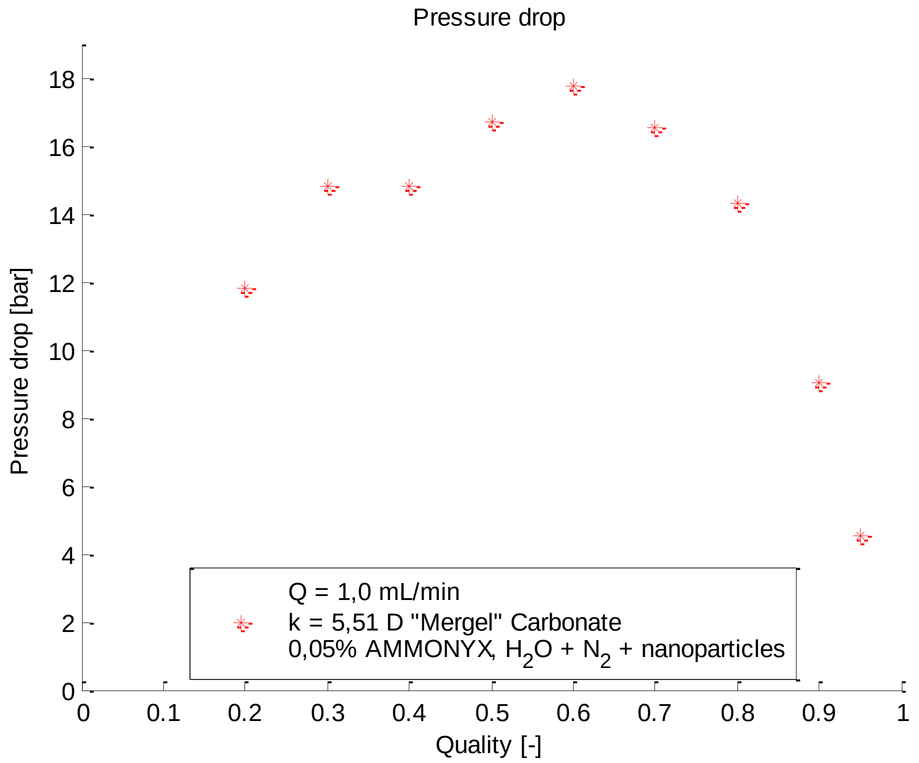

Figure 58: Steady-state pressure drops in experiment Q

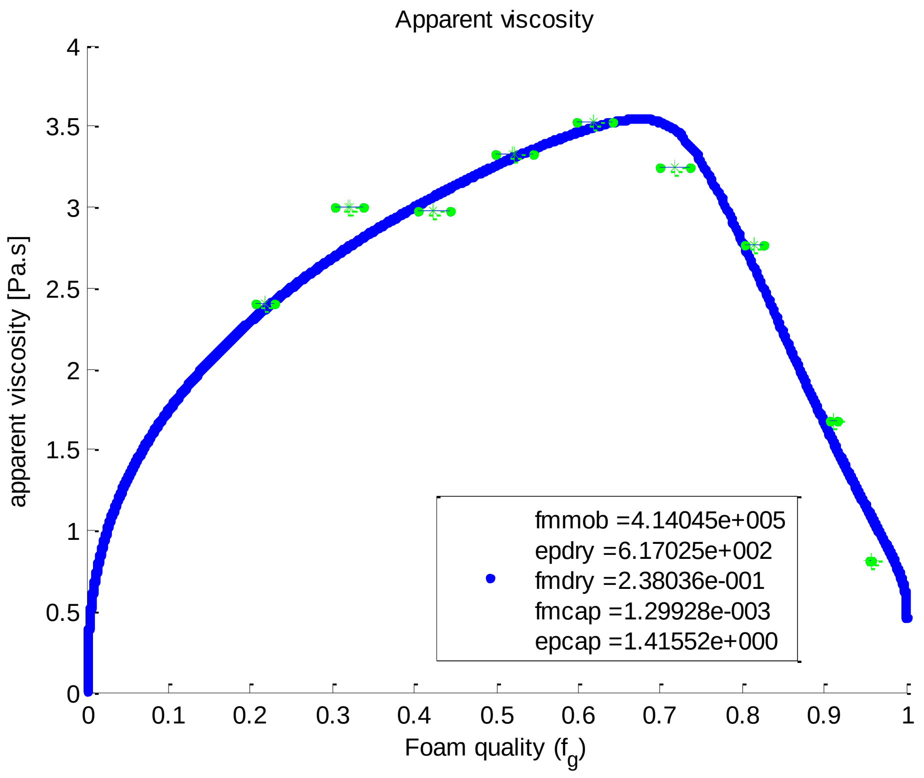

Figure 59: Matching of LE foam model with experiment Q

5.3.13 Experiment R: Nitrogen + 0,05% Ammonyx in demi water

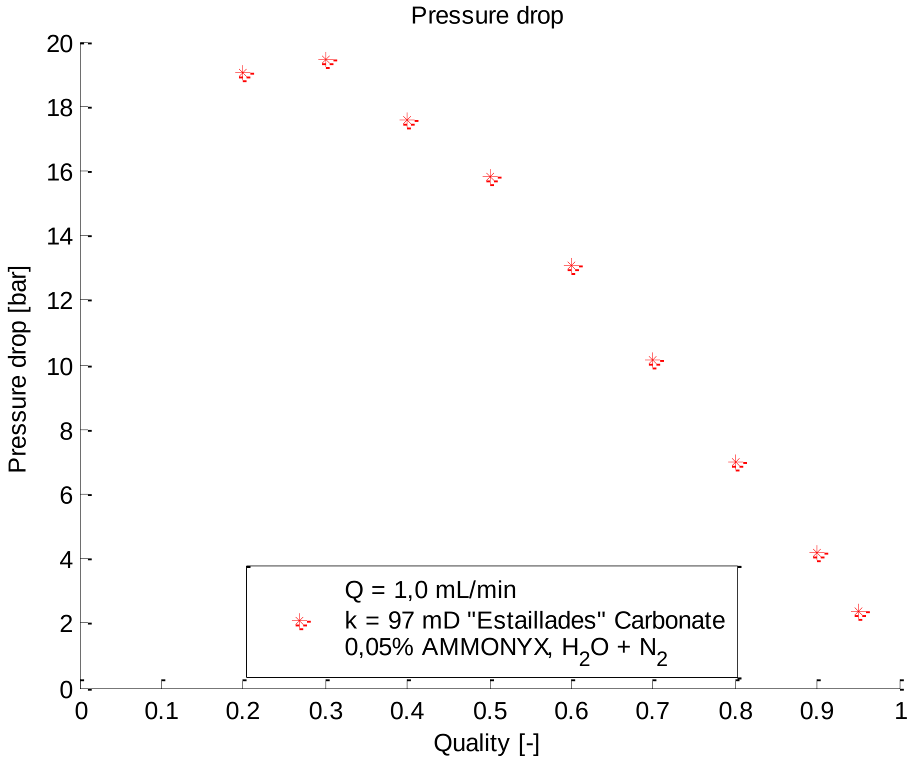

Figure 60: Steady-state pressure drops in experiment R

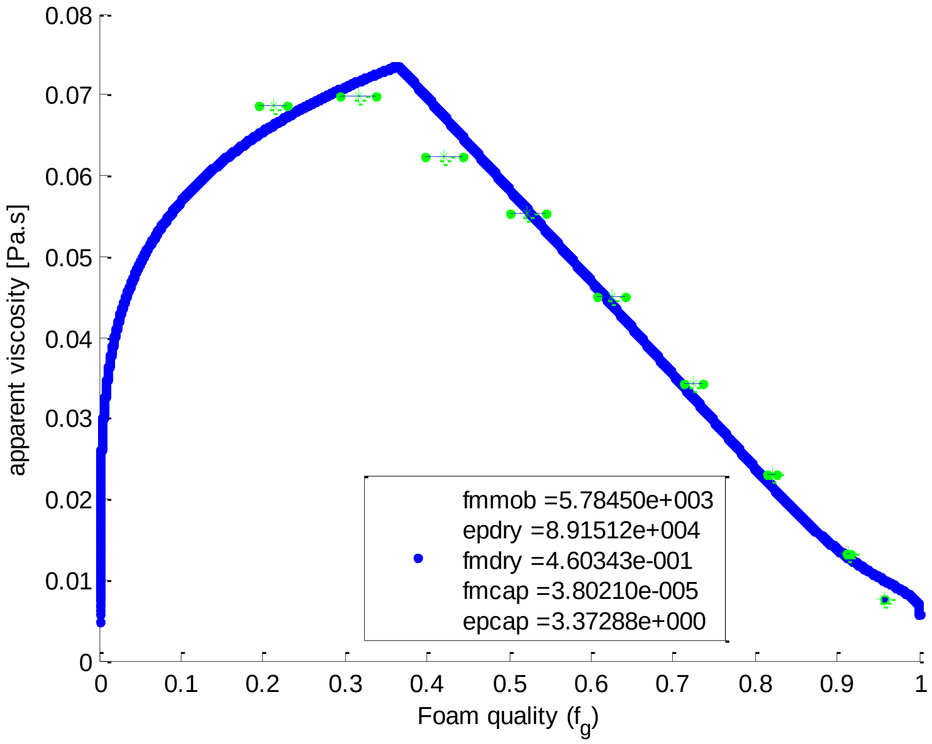

Figure 61: Matching of LE foam model with experiment R

5.3.14 Experiment S: Nitrogen + 0,05% Ammonyx in demi water nanoparticles

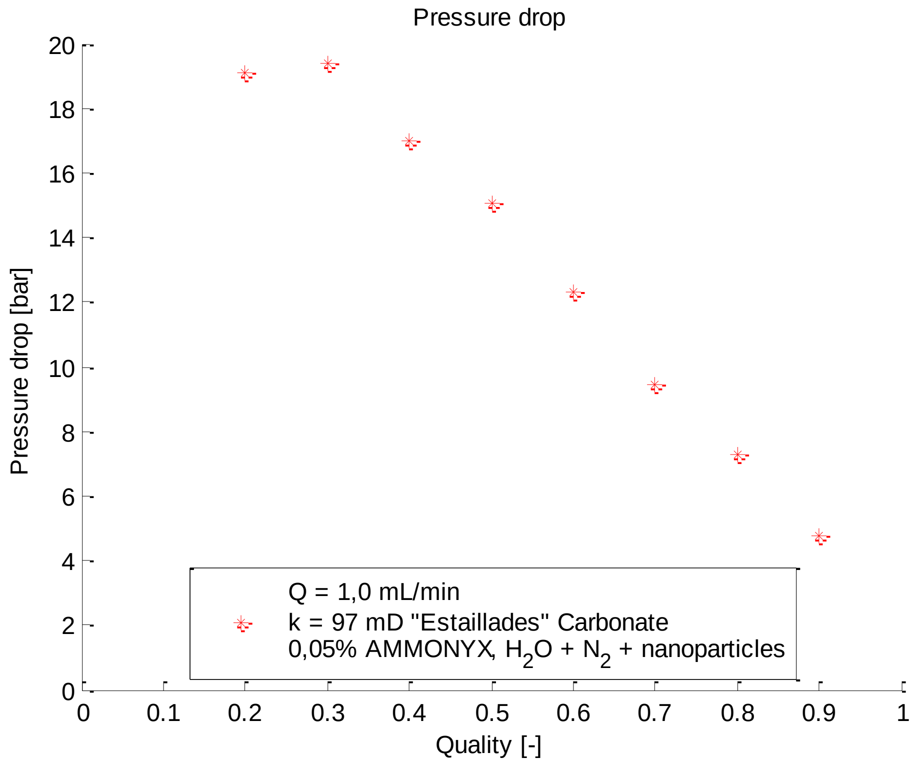

Figure 62: Steady-state pressure drops in experiment S

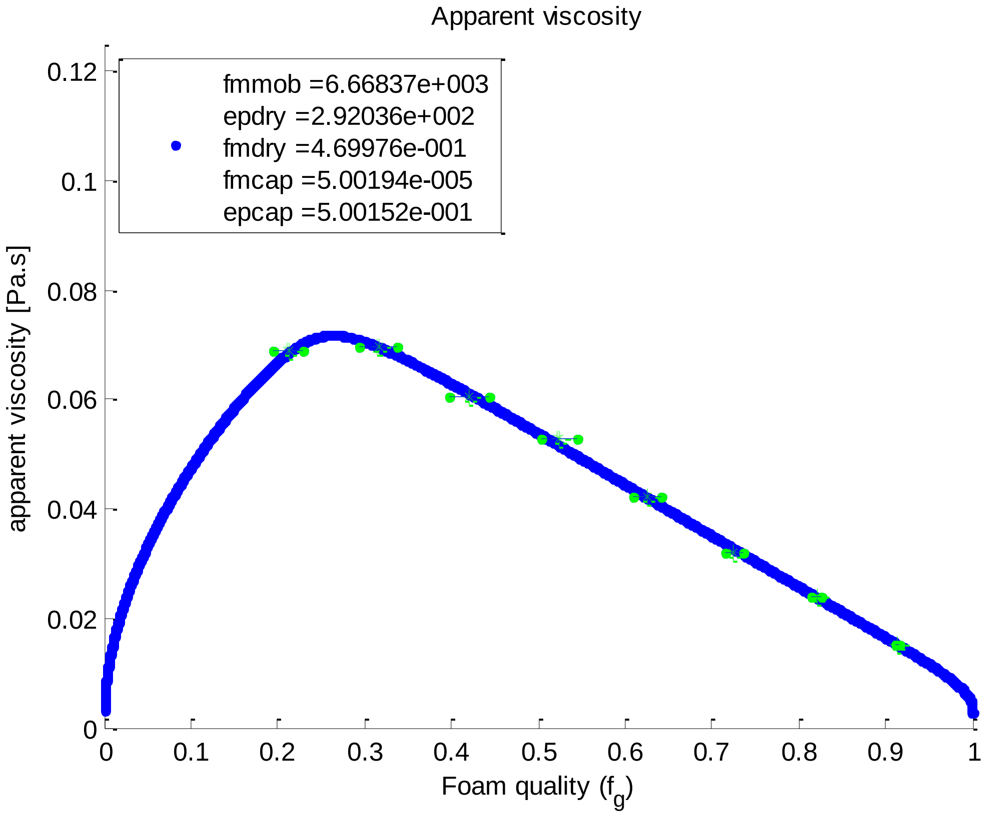

Figure 63: Matching of LE foam model with experiment S

5.4 Nanoparticle flooding

Experiments with nanoparticle-enhanced foam are more difficult than general foam flooding. The presence of nanoparticles introduces multiple challenges. While conducting this research, iterations were required to find a suitable way to deal with the complications nanoparticles introduce as they are typically not reported on. In order to show every effort has been made to correctly interpret results and to reliably conduct nanoparticle experiments, this section shows which issues were encountered and how they were handled. It starts with the initial precautions, followed by the results they yielded and the iterations that were performed afterwards.

5.4.1 Nanoparticle abrasivity

Nanoparticles have a tendency to adhere to surfaces they come in contact with. Therefore, all equipment that is used for their experiments will become 'polluted' over time. This is not necessarily an issue for simple equipment such as tubing. However, more delicate equipment will not be able to sustain a nanoparticle-polluted environment for extended periods of time, as the particles are abrasive. Particles stuck between moving surfaces cause tolerances to change and accuracies to decrease. The liquid pump is one of the most expensive components of the setups used in this study and should not be subjected to a nanoparticle-polluted environment. Therefore, a transfer vessel should be used.

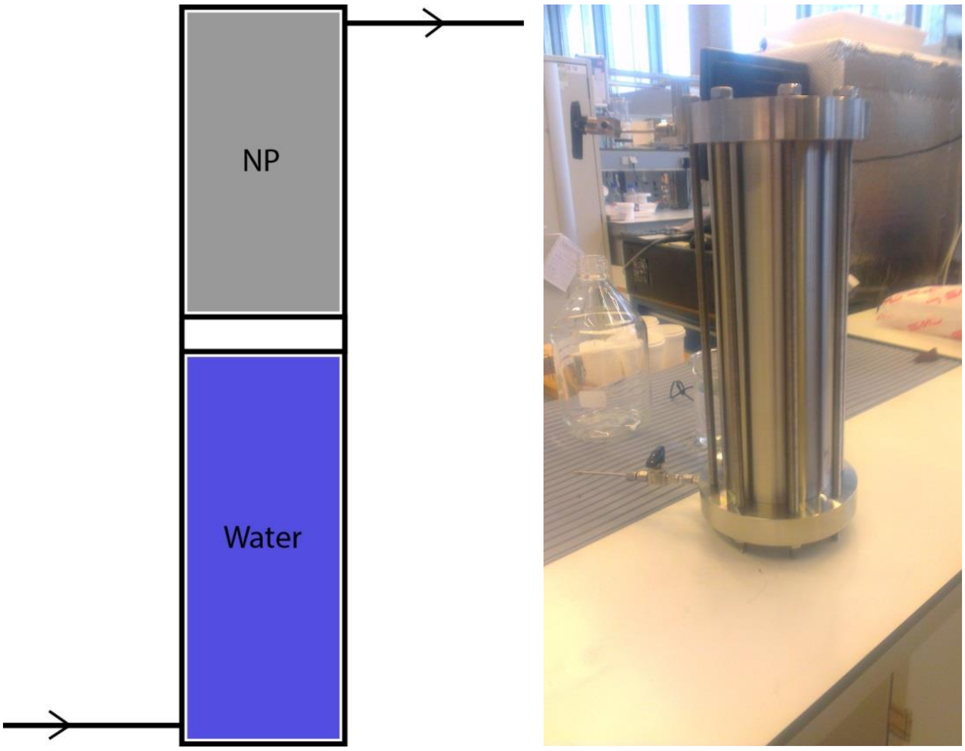

Figure 64: Schematic and photograph of a transfer vessel

Figure 64 displays a schematic drawing of a transfer vessel, and shows a transfer capable of handling high pressures. The pump injects a liquid at one side of the cylinder which displaces a piston. The piston forces the nanoparticle suspension out at the same rate as the liquid is being injected.

5.4.2 Filtration

As particles are injected into the porous medium, there is the possibility that these particles obstruct fluid flow through the core. This effect is known as pore clogging or filtration. The smallest of pores can be blocked by the particles themselves, while larger pores can potentially be blocked by agglomerated nanoparticles, or when several particles arrive to the pore neck simultaneously. Despite these nanoparticles being separated with an ultrasound device, they will slowly agglomerate if their absolute value of zeta potential is not sufficiently high. This is dealt with by injecting fluid from the top of the transfer vessel. The idea behind this is that agglomerated particles are heavier than non-agglomerated particles and will henceforth tend to drop to the bottom of the vessel. The desired non-agglomerated particles reside at the top. Despite injecting from the non-agglomerated part, the experiment is still time-sensitive. Therefore, once the experiment has started all measurements should be taken as quickly as possible.

5.4.3 Experimental results – Experiment J

With the setup adjustments mentioned in the previous two sections being put into place the first nanoparticle experiment was conducted: experiment J. This experiment was conducted at a temperature of 80 ˚C, a pressure of 80 bar, with the nanoparticles and surfactant carried in seawater. As a saline and high temperature environment is expected to have a negative effect on suspension stability, filtration of particles is a primary concern. This was assessed by injecting nanoparticle suspension at a low rate, and comparing the external pressure drop to the internal pressure drop. The pressure increase at the inlet of the core is a sign of formation of external filter cake. Figure 65 is the pressure observation while injecting nanoparticle suspension.

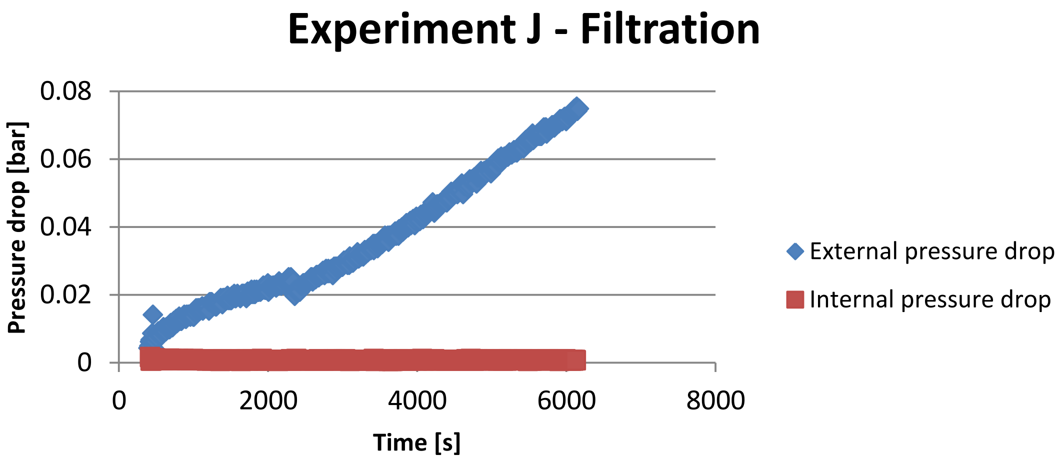

Figure 65: Filtration in experiment J

The interval over which the internal pressure gauge measures the pressure drop is 25% of the total core length. Therefore, the pressure drop should increase with 25% of the total pressure drop, if this pressure drop is uniform. From Figure 65 it can be observed this is not the case. The non-homogeneous resistance increase can be explained by the formation of a filtration cake. Figure 66 schematically depicts this effect. Because the filtration effect was considered to be relatively small compared to the expected overall pressure drop, the experiment was continued.

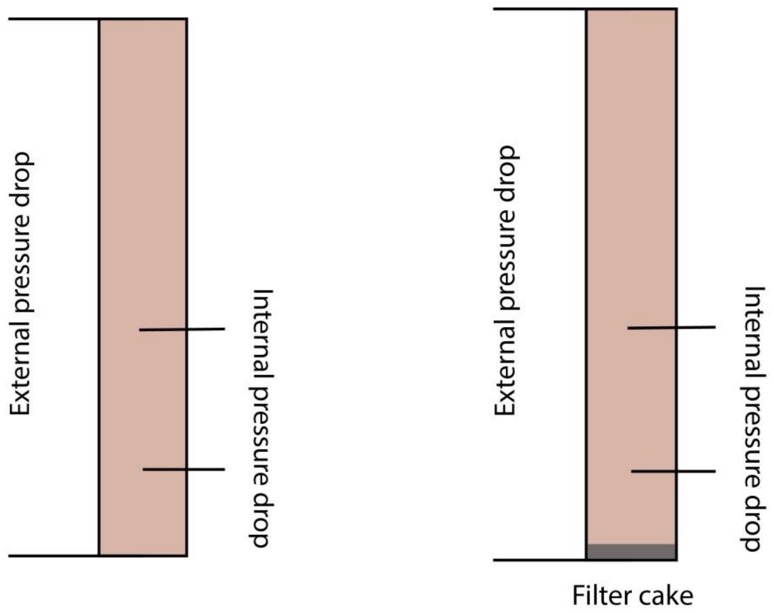

Figure 66: Schematic of filtration cake at core inlet

When conducting a foam-quality scan, the measurements of interest are the steady-state pressure drops. This implies the points are repeatable, and independent from their starting point. Figure 67 shows the external pressure drop over time for this experiment, where the foam qualities from measurement to measurement were done randomly.

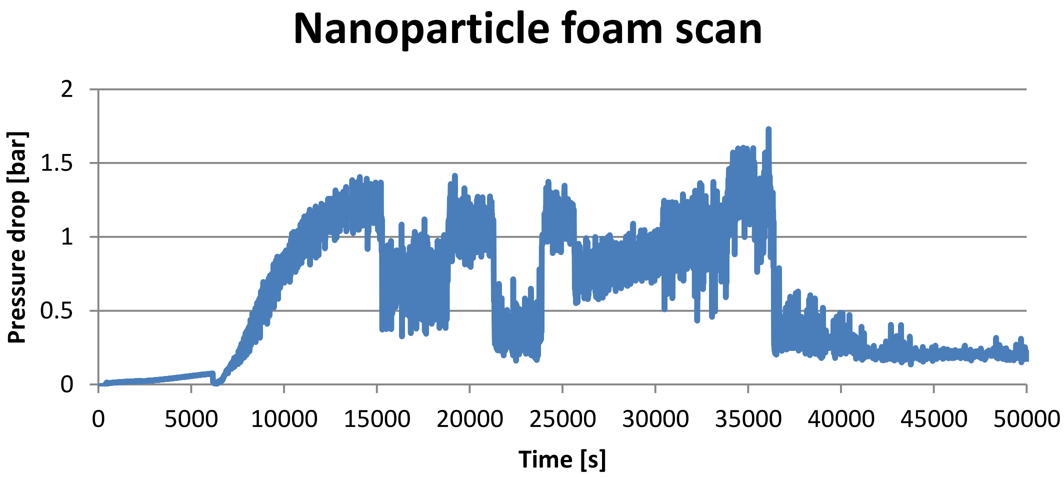

Figure 67: External pressure drop versus time measurement experiment J

From observing this data it is not apparent that any significant filtration cake was forming. However, this changes when the external pressure drops are plotted versus their quality, as done in Figure 68.

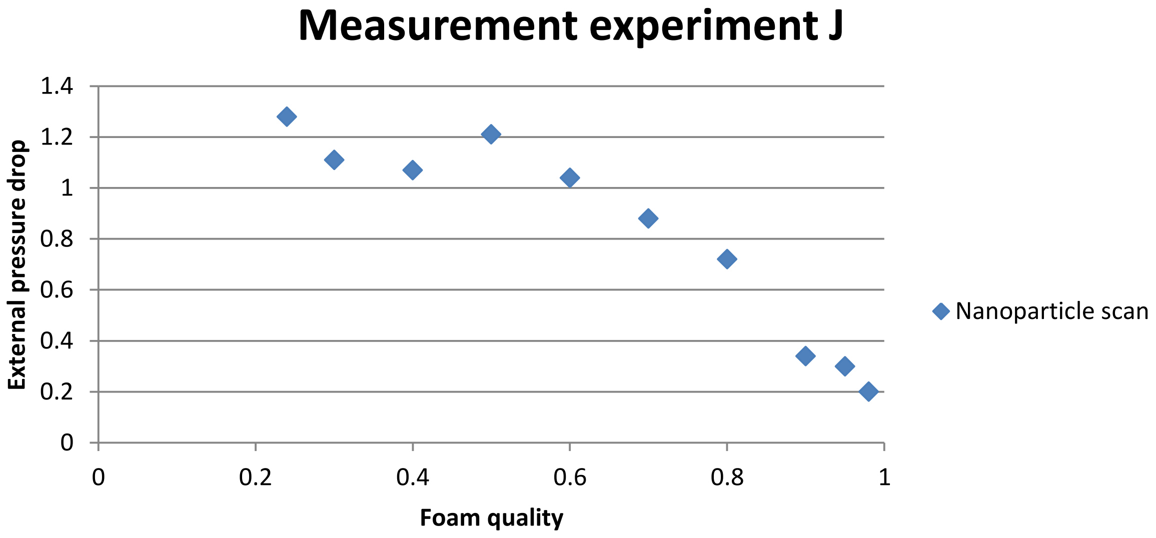

Figure 68: External pressure drop versus foam quality measurement experiment J

Figure 68 shows that the nanoparticle-enhanced foam scan behaviour does not follow the regular foam-scan shape. An increase in pressure drop is visible for foam qualities of 0,3 and 0,4. There are three possible reasons for this pressure drop increase:

- The foam is actually stronger for low qualities because of an effect introduced by nanoparticles
- The filtration cake causes a significant pressure drop
- Nanoparticles block the pores deep inside the core

There are two tools available to assess which of the three situations is the case. The first method is to repeat the experiments and observe the result. If external and internal filtration are an issue, the overall pressure drop will increase when the experiment is repeated. The second method is to compare the internal and external pressure drop. A cake at the entrance will not be picked up by these tabs. If nanoparticles block the inside of the core, the internal pressure drop will increase when the experiment is repeated.

Figure 69 displays the result when the experiment is repeated. The external pressure drop continues to increase, while the internal drop does not show different behaviour. Therefore it can be concluded that nanoparticles do not block pores deep inside the core. However, it does become clear the cake formation is a large contributor to friction.

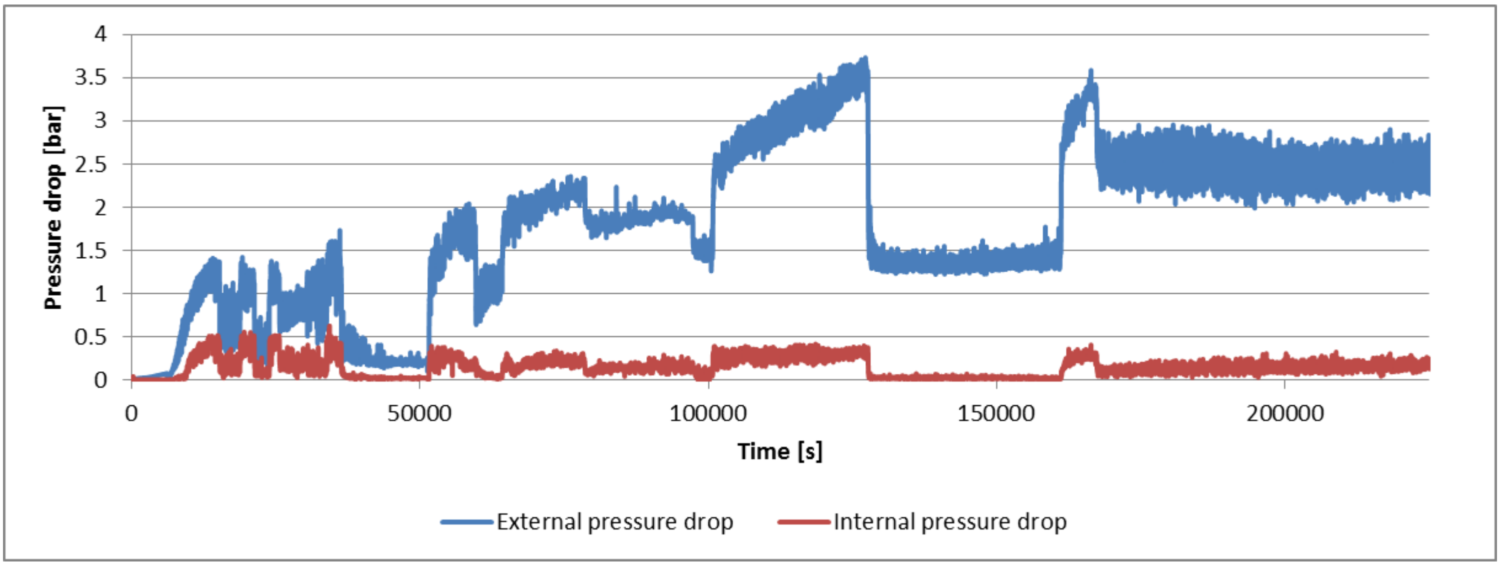

Figure 69: Experiment J - extended duration

The effect of cake formation can be visualized using the 'layer cake ratio' R_c, which is given in equation (33):

$$R_c = \frac{\Delta P_{ex}}{\Delta P_{in}} \frac{L_{in}}{L_{ex}} \tag{33}$$

Where ΔP_{ex} and ΔP_{in} are the pressure drops over the whole core and inner interval, with their corresponding lengths L_{in} and L_{ex}. $R_c > 1$ means the overall pressure drop is larger than what is expected by observing the internal pressure drop. The visualization shows the increase of the filtration effect over time, given in Figure 70. From this figure it become clear that there is indeed significant filtration.

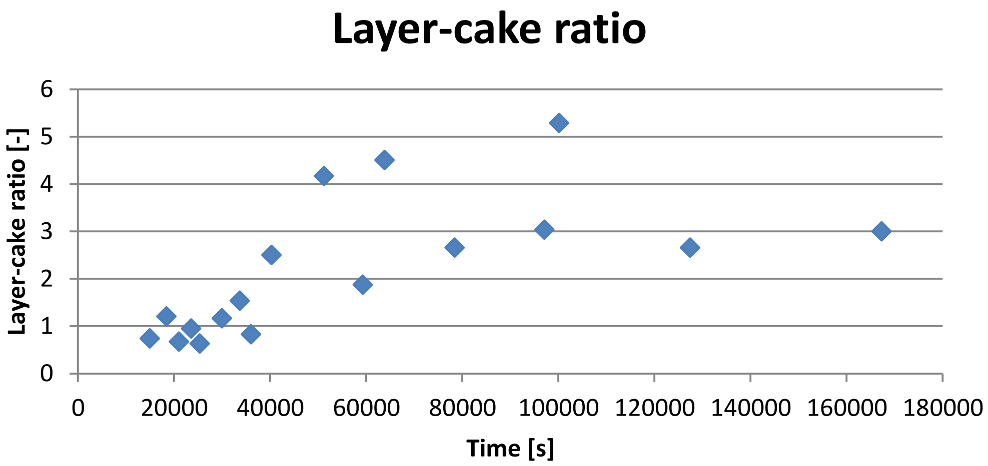

Figure 70: Layer-cake ratio for experiment J

5.4.3.1 Nanoparticles in outlet vessel

During the continuation of this experiment it was observed that no nanoparticles were exiting the system. There are two scenario's that can cause the absence of nanoparticles in the outlet vessel:

- Filtration of nanoparticles
- No nanoparticles being injected

The first scenario synergizes well with the formation of a layer cake caused by filtration. When starting the experiment with a clean core, only the largest (agglomerated) particles will be filtered. However, these large particles are effectively reducing the pore sizes at the entrance. The result is a reduction in the size of particles that is able to enter the core. Therefore, more particles will be filtered, which will further reduce the amount of particles able to enter the core. This is an iterating process that will eventually lead to the filtration of (almost) all particles.

For the second scenario the behaviour of particles in their suspension has to be observed. The particle size is too small for their motion to be influenced by gravity effects, but gravity still affects their behaviour to a small extent. Sorting may occur due to gravity pulling larger particles down more than light particles. Therefore, the lower part of the suspension will have a larger fraction of larger particles, while the light particles reside at the top. A concentration gradient may form due to gravity, which may cause the concentration at the top side of the vessel, from which they are injected into the core, to be very low. This is shown in Figure 71. This effect can cause nanoparticles to be injected in the initial stage of the project, but can cause a decreased nanoparticle concentration in the injectant over time.

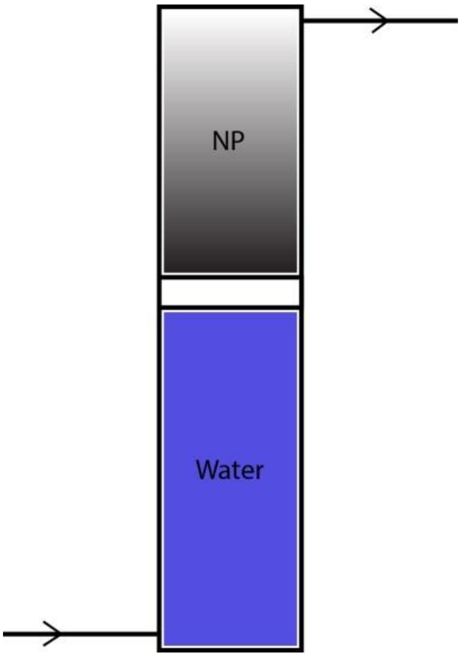

Figure 71: Gravity sorting of nanoparticles in transfer vessel

5.4.3.2 *Filtration evidence*

Prior to the next experiment the core was removed from the core holder for further investigation. If filtration is an issue it will be visible on the injection side of the core due to the dark colour of the injected particles. After removal the core was cut in half over the length of the core. After cutting, the sides were cleaned with high-pressure air to remove cutting debris. The result is shown in Figure 72.

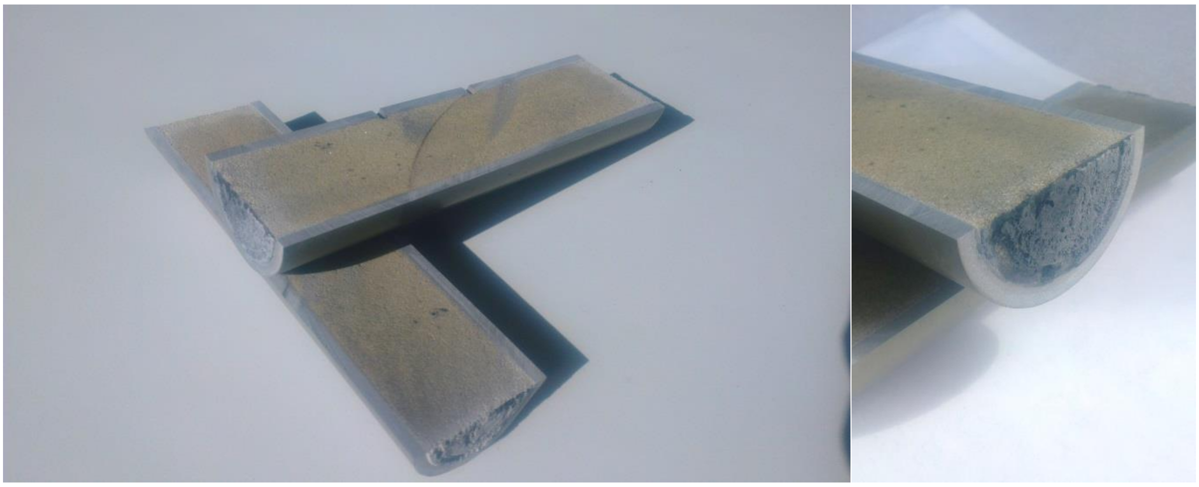

Figure 72: Photograph of filtration after experiment J

On the photographs the dark grey substance at the head of the core is visible. This is the filter cake consisting of filtered nanoparticles. Inside the core only a very limited number of nanoparticles are visible.

5.4.4 Setup enhancements

The setup was improved to handle the effects described in the previous section. Three improvements were required:

- Prevention of filter cake formation
- Uniform particle distribution in transfer vessel
- Increase of distance between internal pressure gauge connections

These improvements aid in the detection of any filter cake. By increasing the distance over which the internal pressure drop is measured, a better representation of the core is achieved while still being able to avoid any false measurement interpretations due to cake formation.

5.4.4.1 First improvements

The enhanced setup is displayed in Figure 73. Filtration of large particles is done right after the transfer vessel by leading the particles through a core. Maintaining a uniform particle distribution is done by placing the transfer vessel on a magnetic stirrer. A photograph is shown in Figure 74.

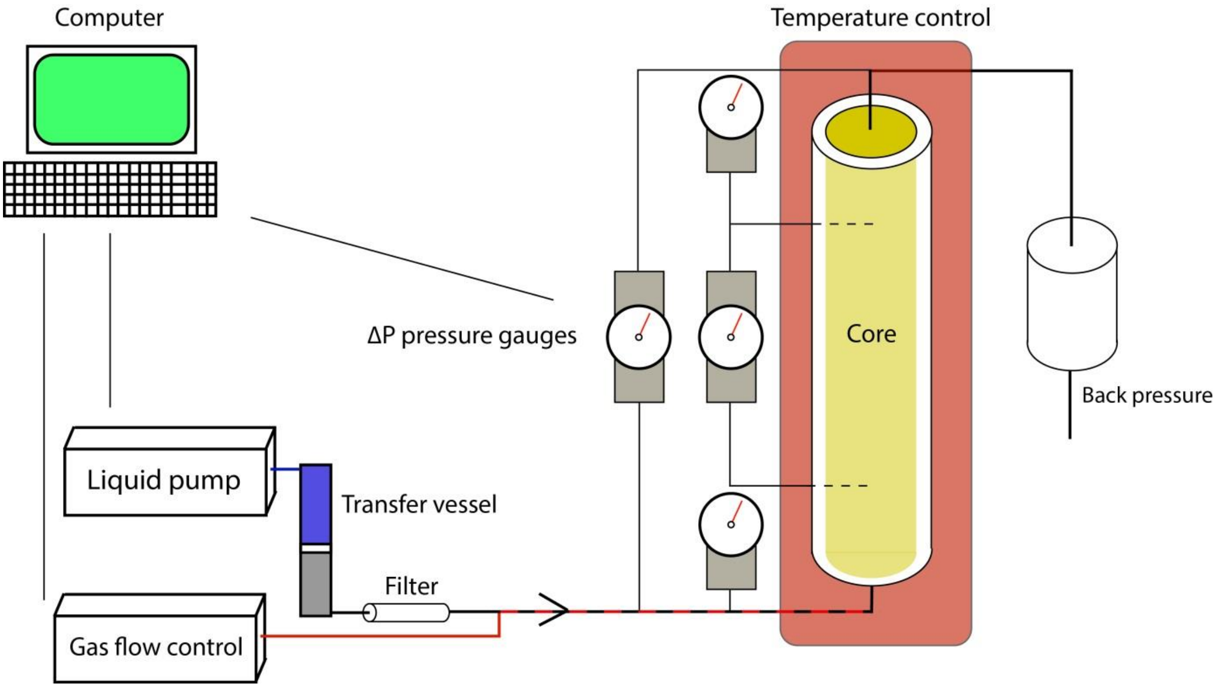

Figure 73: setup 2 with improvements

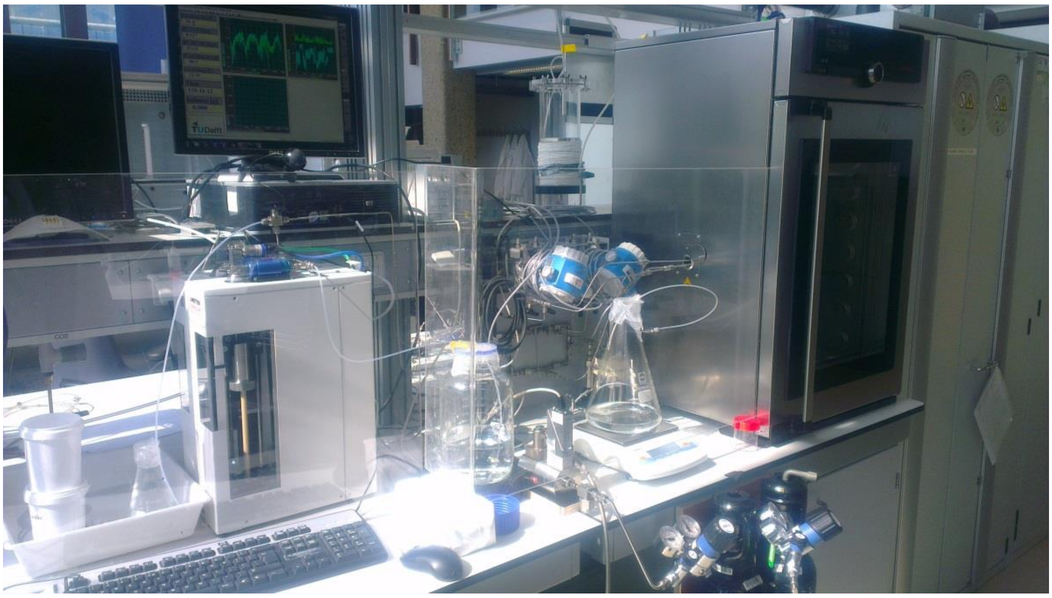

Figure 74: photograph of setup 2 with improvements

5.4.4.2 Further improvements

When the setup shown in Figure 73 was tested, the pressure differential over the filter increased rapidly. As the cross-sectional area of the filter was limited it became blocked by particles very fast. The pressure drop over the filter exceeded 40 bar when the experiment was cancelled. A new method to prevent formation of filtration cake was invented, which is shown in Figure 75.

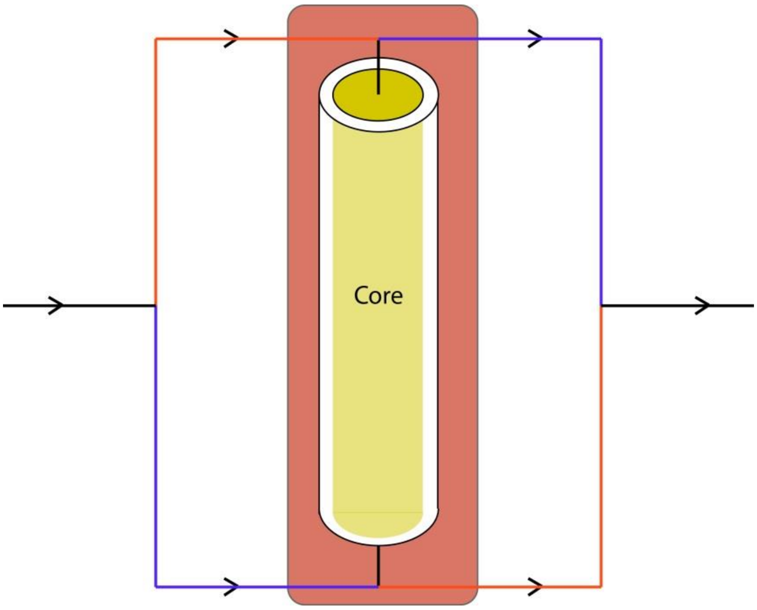

Figure 75: Core flooding - alternating injection sides route 1 in blue, route 2 in red

In this method, the filter was removed from the setup. Instead, after preparation of the suspension it was 'rested' overnight, to let the largest particles settle. Then the top 80% of the liquid was used for injection in the core. Despite removal of the largest particles, it is still expected that a filtration cake will form. To remove the debris the flow direction in the core was changed after every measurement. There was a pressure gradient through the core, which caused the pressure at the inlet (where cake forms) to be higher than the outlet. When the pressure at the inlet was connected to the regulated outlet pressure, the gasses rapidly escaped through the core inlet, taking away filtered nanoparticles in the process.

In further nanoparticle-injection experiments it was confirmed that this method indeed prevented the formation of a filter cake. Figure 76 is a photograph from a chalk core after the nanoparticle experiment (the damage to the core was done when the core was removed from the core holder).

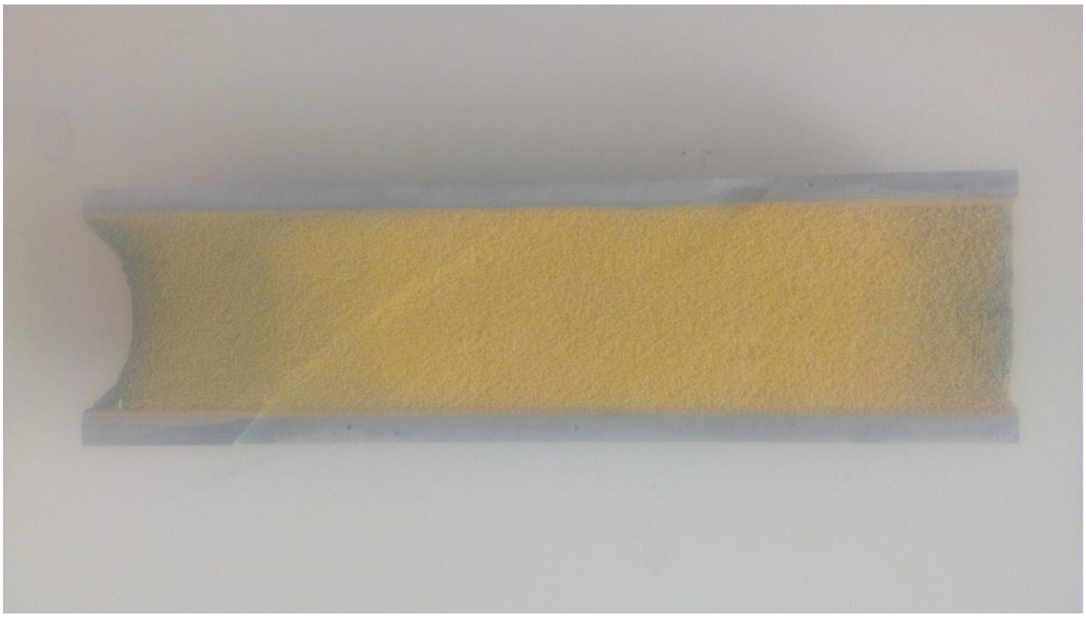

Figure 76: Carbonate (chalk) core after nanoparticle experiment

The picture was taken after washing the core with water to remove the cuttings. The dark color at both ends of the core is an indication of clogging due to particles. Visual inspection did not reveal particles stuck in the inner core section. The internal pressure gauge takes the measurement over this inner clean section. Therefore it is assumed the permeability over which the (internal) measurement is taken is not altered by particle clogging. In addition, Figure 77 shows a constant layer-cake ratio in experiment Q, where this method was applied. This implies the permeability at the ends is also not reduced significantly as a result of filtration, despite the grey color. The alternating-flow method is therefore suitable for avoiding filtration-related measurement errors.

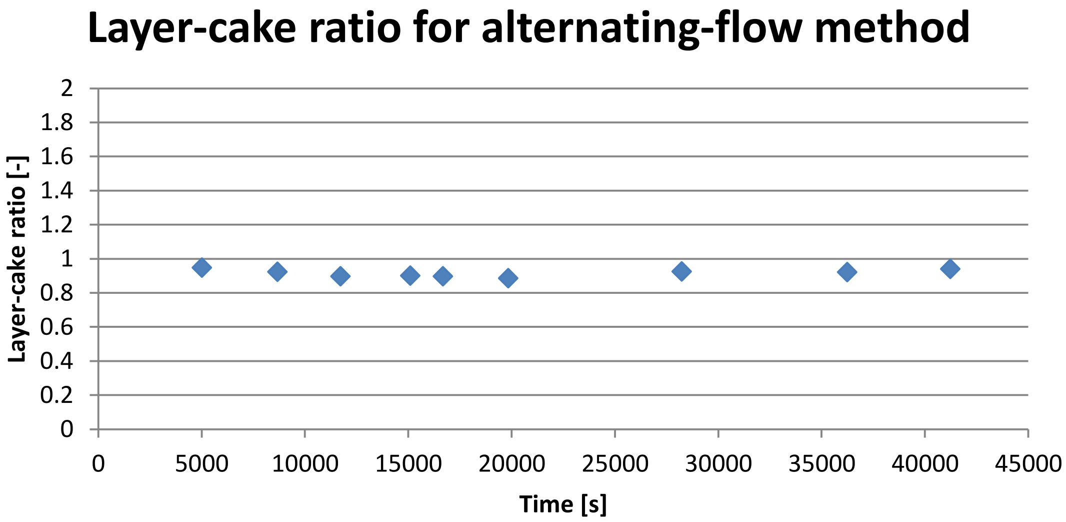

Figure 77: Layer-cake ratio for experiment Q

5.5 Bulk foam experiment

Reducing the drainage rate is one of the mechanisms of increased foam stability by nanoparticles. The effect of lamella drainage can be measured in bulk foam, using the setup explained in section 4.1.3. In this experiment, foam is continuously generated while the fluid levels are measured. The important parameters for this experiment are displayed in Table 13.

Parameter	Value
Initial amount of surfactant solution	50 cc
Surfactant concentration	0,0315 wt% AOS 14-16
Gas flow rate (N_2)	10 cc/ minute

Table 13: experimental parameters foam column experiment

Two fluid levels are measured: the height of the liquid-foam interface, and the elevation of the foam-air interface. These are displayed in Figure 78. By subtracting the two, the height of the foam column can be determined. With foam generation, the liquid level drops. During the experiment foam lamellae start to drain, causing liquid to flow back to the bottom which in turn increases the liquid level. To compare data from experiments with and without nanoparticles, the amount of liquid inside the foam is determined. The amount the liquid level has dropped can be divided directly by the height of the foam column to obtain the average foam quality (amount of liquid in foam phase).

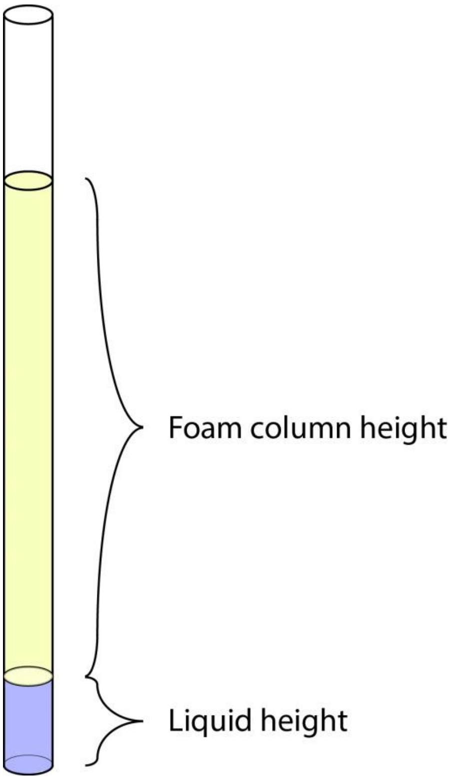

Figure 78: schematic of important variables in bulk foam experiment

5.5.1 Performed bulk foam experiments

Four experiments are conducted. Two experiments are performed with only surfactant, and two experiments have nanoparticles added to the surfactant solution. In all cases, the duration over which the experiment is performed is approximately 60 minutes. At regular intervals the fluid height is measured. This results in the graph shown in Figure 79.

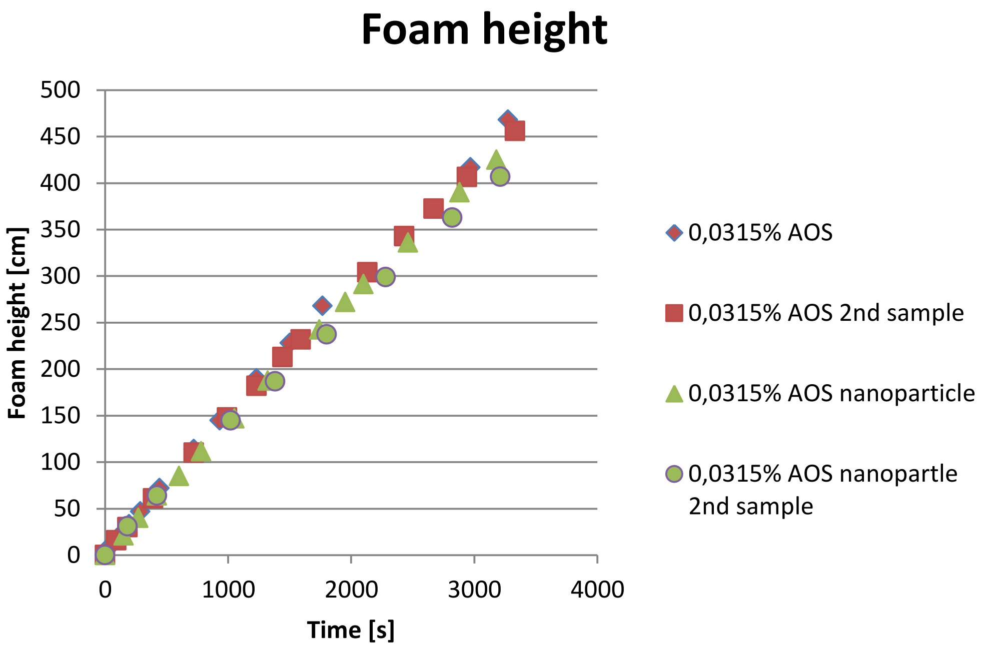

Figure 79: foam height of bulk foam experiment, at a N_2 injection rate of 10 cc/min

As can be seen in this figure the foam height is approximately equal for all cases and the rate at which foam is generated is linear during the 60 minute testing interval. This means the rate of foam generation is equal for all experiments.

The liquid level measurements are given in Figure 80. For the non-nanoparticle case, the liquid height is around 19 cm at the end of the experiment. For the case where nanoparticles were added to the setup the liquid level is significantly lower. This indicates presence of more liquid in the foam phase.

Another observation is the minimum in liquid height during the experiment, followed by an increase in liquid height during foam generation. This is due to the drainage effect. Surfactant molecules are used to generate foam bubbles. Those molecules are adsorbed at the gas-liquid interface and are immobile. Water inside the foam lamella (with a lower concentration of surfactant molecules compared to the original bulk concentration) is free to move around, and will be pulled downward due to gravity. The surfactant concentration in the liquid phase a the bottom of the column decreases, which causes the newly generated foam bubbles to be coarser in size.

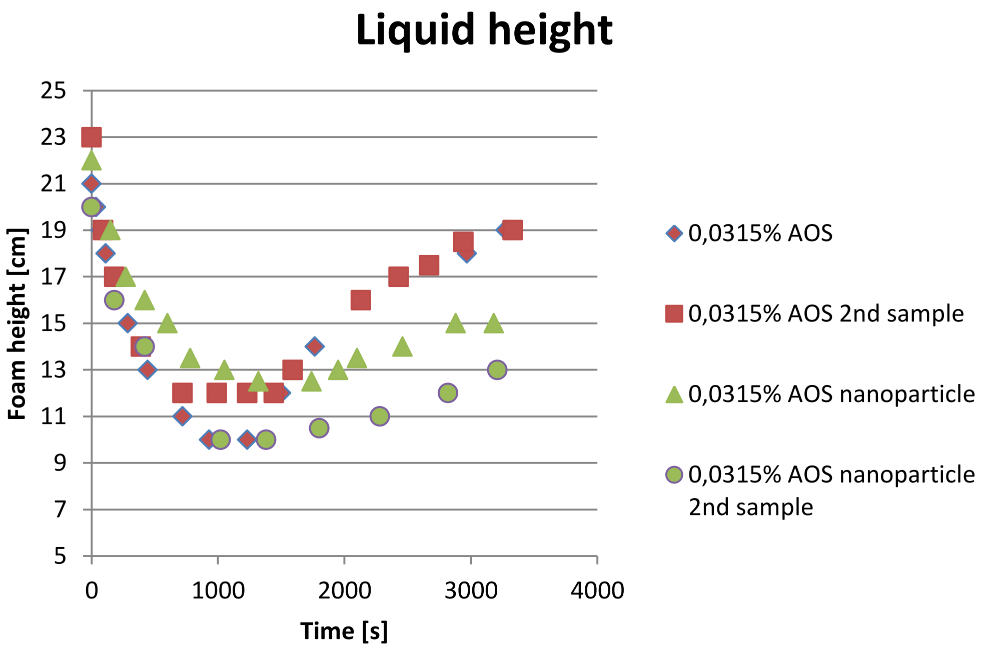

Figure 80: liquid height of bulk foam experiment, at a N_2 injection rate of 10 cc/min

5.5.2 The liquid/ foam ratio

The measurements presented in the previous section can be combined to obtain the liquid to foam ratio. This is obtained by dividing the amount of liquid in the foam by the foam height. This leads to the result given in Figure 81.

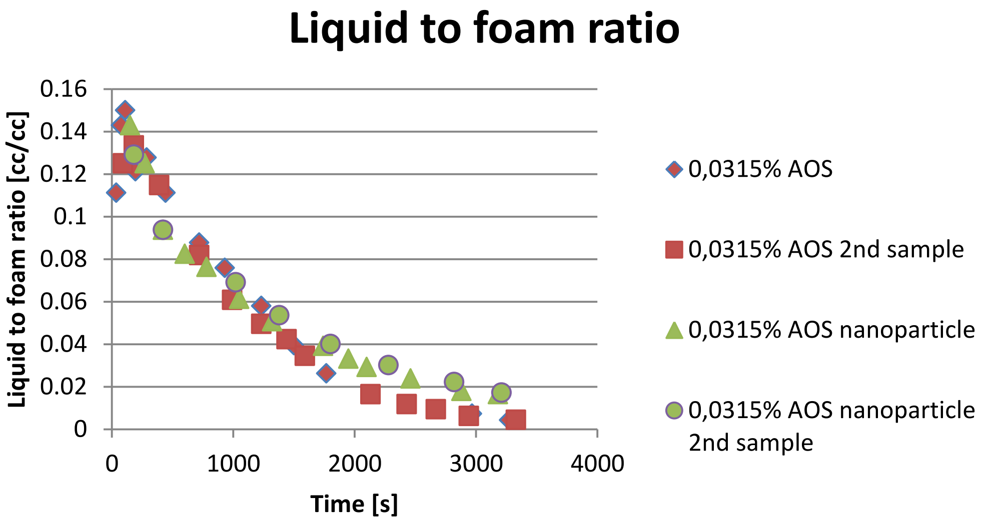

Figure 81: liquid to foam ratio of bulk foam experiment, at a N2 injection rate of 10 cc/min

As can be seen in the figure, nanoparticle foam appears to be 'wetter' after roughly 1400 seconds, or approximately 25 minutes. Prior to that point, the difference is small. The visualization of this effect can be enhanced by plotting the y-axis on a logarithmic scale. This is done in Figure 82.

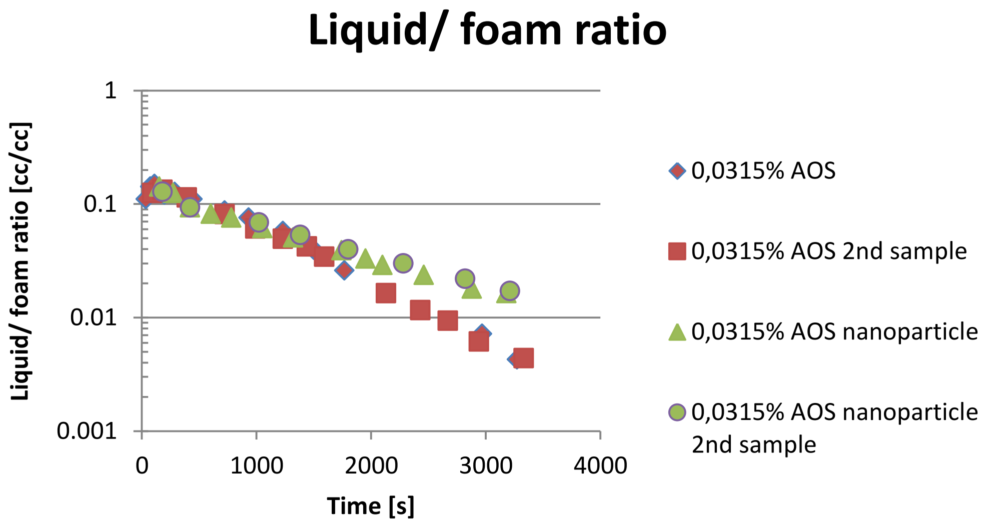

Figure 82: liquid to foam ratio of bulk foam experiment plotted on a logarithmic y-axis, at a N2 injection rate of 10 cc/min

From this graph it becomes clear that there is a large difference in the foam quality after 60 minutes of foam injection. Nanoparticle-enhanced foam appears to be 3-4 times more wet than non-enhanced foam. This is an indication that nanoparticles do indeed have a preventive effect on foam drainage. The mechanics behind this effect will be discussed in Chapter 6, where the observations will be related to the theory presented at the beginning of this study.

5.6 Summary

In this chapter data is presented on dynamic experiments, steady-state core flooding experiments and bulk foam experiments. The evaluation of the measurements can now be done by comparing the conducted experiments. The core-flooding experiments have many parameters influencing the outcome, and the effect of each of those parameters will be isolated.

The next section discusses the observed effect of nanoparticles with use of the data presented in this section. It is attempted to create a coherent story on the effect of nanoparticles based on the observations. By combining the knowledge gained by these experiments the strengths and limitations of the nanoparticle can be determined.

6 Discussion

This chapter discusses the experimental observations. The theoretical background provided in the earlier chapters is used to explain results and findings when multiple experiments are compared with each other. The effectiveness of adding nanoparticles to the foam solution will be investigated.

6.1 Model fit to experimental data

In chapter 5 the experimental data is fitted to the CMG-STARS foam model. In most cases this fit is satisfactory, but in some cases the observed data shows different behaviour than what is observed. An example are the processed results from experiment H:

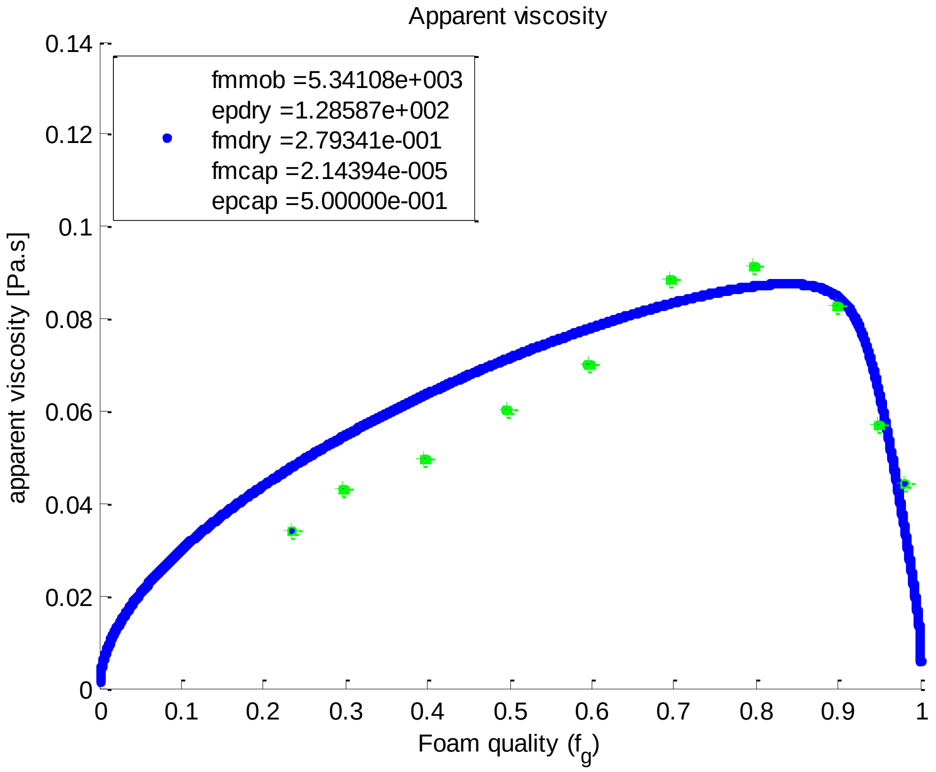

Figure 83: Processed results experiment H, an example of how the CMG-STARS model interpretation does not agree with the measurements.

The curvature in the low-quality regime does not match the experimental data. This is caused by the F5 component of the foam model, which represents the effects of the capillary number. The parameter *epcap* within F5 captures shear thinning behavior as given in (34):

$$F5=\left(\frac{fmcap}{N_{ca}}\right)^{epcap} \tag{34}$$

By changing the way F5 depends on *epcap*, the effect of epcap can be changed from shear thinning to shear thickening, as shown in equation (35):

$$F5=\left(\frac{fmcap}{N_{ca}}\right)^{-epcap} \tag{35}$$

This can now be used to capture the experimental behaviour. The new, improved fits are shown in Figure 84 for experiment H, and in Figure 85 for experiment I. This enhanced fits will be used for the experimental comparisons.

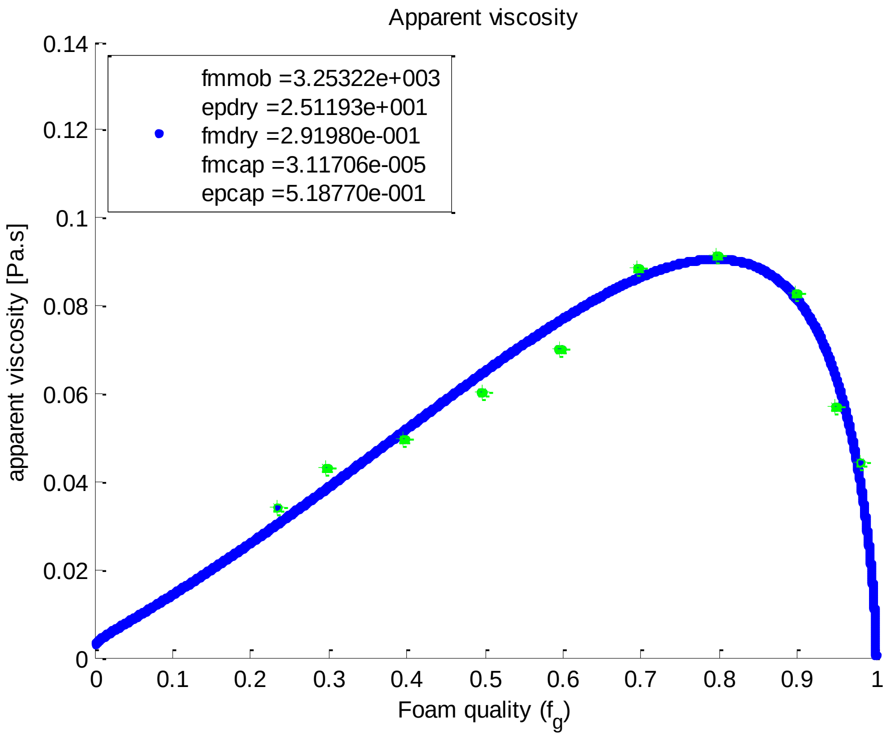

Figure 84: Improved fit for experiment H, including shear thickening

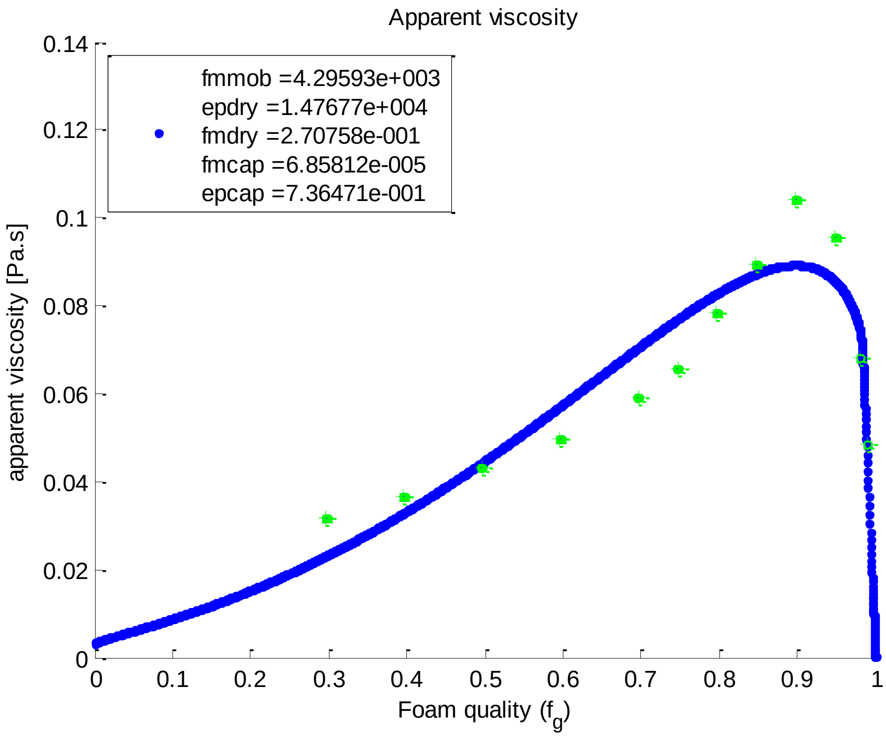

Figure 85: Improved fit for experiment I, including shear thickening

6.2 Effect of pressure

The effect of pressure can be examined by comparing experiment A with experiment O. Both used de-mineralized water as the surfactant carrier, and used the same concentration (0.0315 wt%) of the same surfactant (AOS 14-16). The temperature varied slightly between both experiments. Where experiment A was conducted at room temperature, experiment N was conducted at a fixed temperature of 25C.

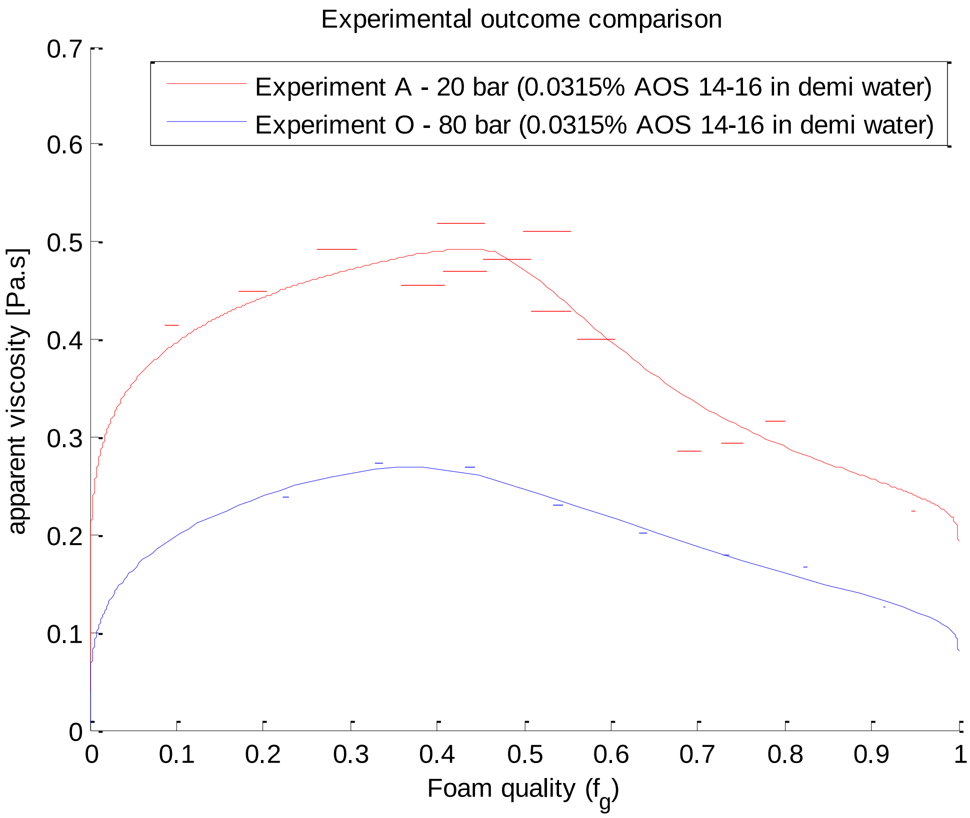

Figure 86: Effect of pressure. Experiment A – 20 bar, Experiment O – 80 bar

As is visible in Figure 86 and Table 14, the high-pressure gas has a lower viscosity or lower mobility reduction factor. This is unexpected as the elevated pressure is believed to increase chemical and mechanical interaction between bubbles, increasing foam viscosity. Apparently this effect is not dominant in porous media.

The unexpected observation can partially be explained by the temperature difference, as a higher temperature will decrease viscosity. This is not the only contributing factor. The effect of foam compressibility on the required pressure gradient to mobilize foam lamellae has been studied previously (Rossen, 1988). That study showed a more compressible foam requires a higher pressure gradient for mobilization. However, the difference in compressibility of the foams in experiment A and O should change with foam quality. If this is the main drive for elevated foam viscosity, this trend should be more pronounced. A third contributor could be the efficiency with which the lamella train is displaced. For lower pressures the relative pressure differential over a foam lamella is larger. When the lamella jumps from one pore throat to another it is subjected to a- and deceleration. The extent to which this happens is larger for a low-pressure environment. This causes foam displacement to be less efficient and therefore apparent viscosity to increase.

	Experiment A (low pressure)	Experiment O (high pressure)
fmmob	$4.11\cdot10^{4}$	$3.56\cdot10^{4}$
epdry	$9.11\cdot10^{2}$	$1.63\cdot10^{2}$
fmdry	$3.34\cdot10^{-1}$	$3.64\cdot10^{-1}$
fmcap	$2.11\cdot10^{-4}$	$1.33\cdot10^{-4}$
epcap	4.99	2.30

Table 14: Estimated parameter comparison experiment A & O

6.3 Effect of temperature

The effect of temperature can be determined by comparing experiment G with experiment K. Both used seawater as a carrier., and used the same concentration (0.0315 wt%) of the same surfactant (AOS 14-16). The back pressure of both experiments is equal at 80 bar.

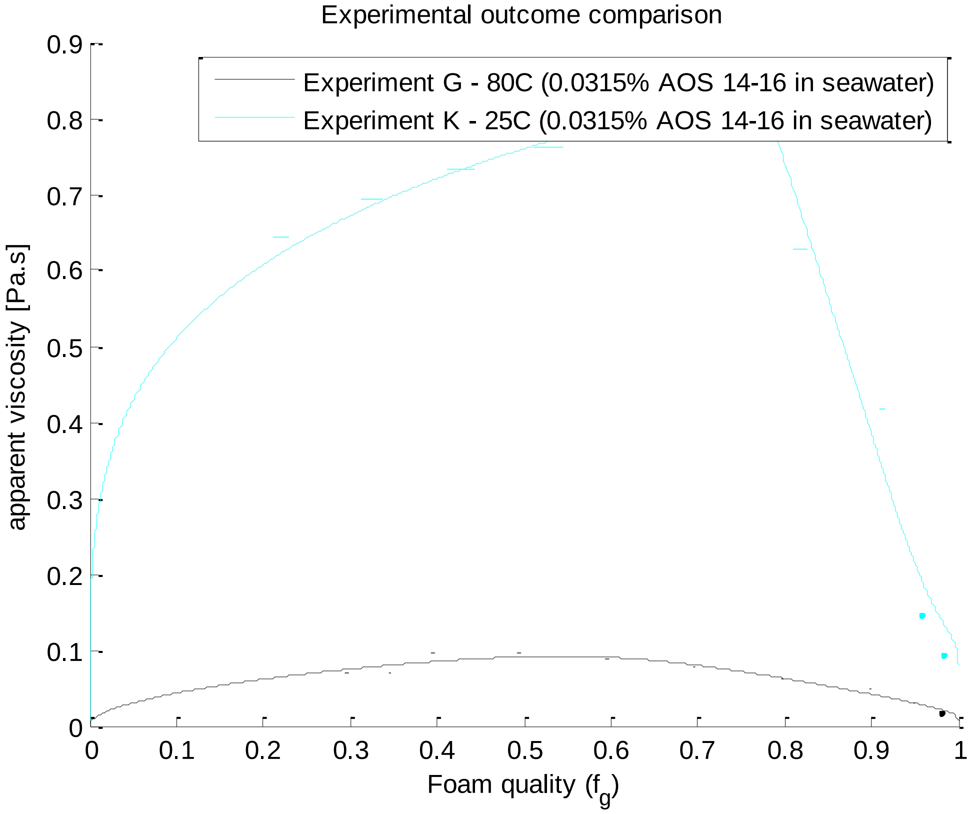

Figure 87: Effect of temperature. Experiment G – 0.0315% AOS 14-16 in seawater at 80˚C, Experiment K – 0.0315% AOS 14-16 in seawater at 25˚C

The gas- and liquid phase viscosities decrease when temperature increases. This directly affects foam viscosity as can be seen in Figure 87. From Table 15 it can be observed the mobility reduction factor for experiment K is much lower than for experiment G. As the liquid viscosity decreases, the surface tension may decrease, accelerating drainage and increasing diffusion. There are more mechanisms affecting foam flow, however. The CMC of a surfactant increases with increasing temperature. When dropping below CMC the foam texture is altered. Coarser foam means a smaller mobility reduction.

Increasing the temperature means the surfactant molecules obtain a higher thermal (kinetic) energy. The surfactant molecules are less easily adsorbed on the foam lamella interfaces, which further decreases foam stability.

	Experiment G (high temperature)	Experiment K (low temperature)
fmmob	$7.70 \cdot 10^{3}$	$1.19 \cdot 10^{5}$
epdry	$8.78 \cdot 10^{1}$	$1.68 \cdot 10^{4}$
fmdry	$3.47 \cdot 10^{-1}$	$2.74 \cdot 10^{-1}$
fmcap	$3.16 \cdot 10^{-5}$	$3.11 \cdot 10^{-4}$
epcap	$5.00 \cdot 10^{-1}$	2.77

Table 15: Estimated parameter comparison Experiment G & K

The dry-out process for hot foam is more smooth compared to that for cold foam in this occasion. The model fit confirms this by returning a large value for epdry for experiment K, indicating an abrupt transition.

6.4 Effect of gas

The effect of the type of gas can be determined by comparing experiment A and B. Both used pure H_2O as a surfactant carrier, with the same concentration (0,0315%) of the same surfactant (AOS 14-16). The back pressure of experiment A is set at 20 bar, while the back pressure of experiment B is set at 10 bar. This had to be done to allow the gas flow controller to deliver enough gas to get high foam qualities at core conditions. CO_2 is heavier than N_2, which means the same mass throughput through the flow controller results in a smaller volumetric gas flow rate.

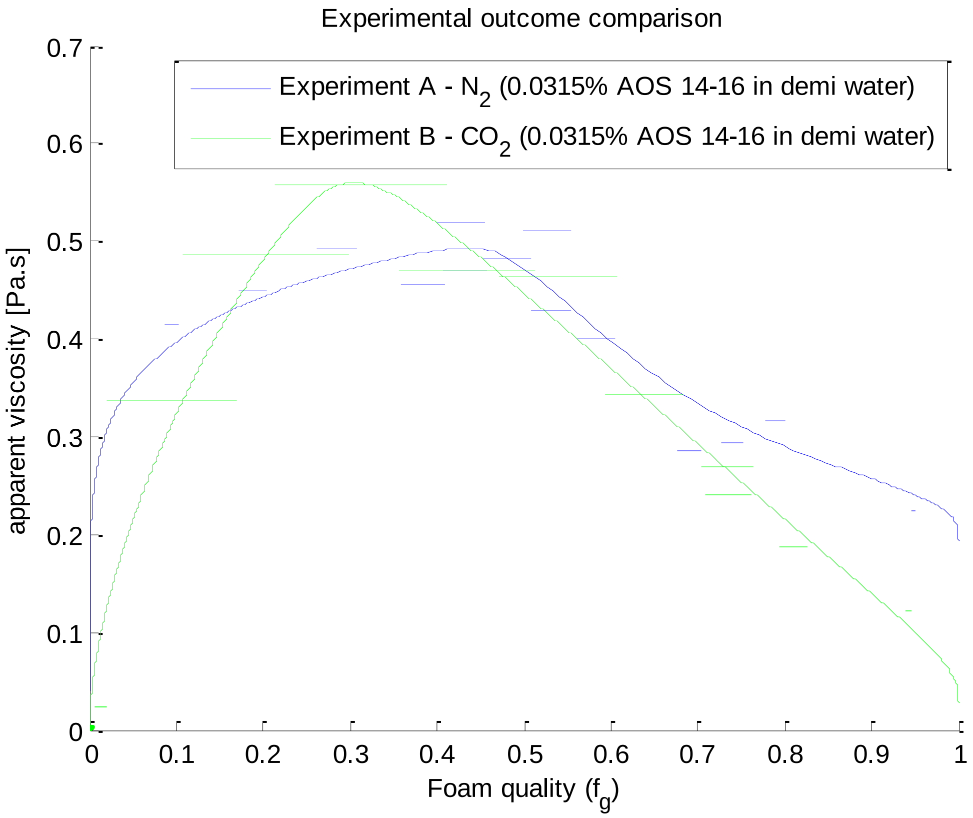

Figure 88: Effect of gas. Experiment A – 0.0315% AOS 14-16 in H_2O with N_2, Experiment B – 0.0315% AOS 14-16 in H_2O with CO_2

Slight variations between the two fitted curves are visible. Experiment B was the first experiment to be conducted with CO_2. The effect of CO_2 solubility was not taken into account while performing this experiment. Because CO_2 dissolved in the liquid phase, the gas flow rate decreased and therefore the total flow rate was lower than the desired 1 mL/min. This deviation is larger for the lowest foam qualities. The script calculates the viscosity of the foam based on the (deviated) flow rate. Due to the shear thinning effect however, the foam viscosity for an equal flow rate will be slightly higher.

The result of this comparison would be that CO_2 foam is stronger in the low-quality regime, and N_2 foam is stronger in the high-quality regime, but overall the outcome is comparable. However, there is a shear-thinning uncertainty in experiment B. Therefore, the comparable outcome can also be coincidental.

	Experiment A (N_2)	Experiment B (CO_2)
fmmob	$4.11 \cdot 10^{4}$	$6.57 \cdot 10^{4}$
epdry	$9.11 \cdot 10^{2}$	$4.09 \cdot 10^{2}$
fmdry	$3.34 \cdot 10^{-1}$	$3.38 \cdot 10^{-1}$
fmcap	$2.11 \cdot 10^{-4}$	$3.49 \cdot 10^{-4}$
epcap	4.99	$5.00 \cdot 10^{-1}$

Table 16: Estimated parameter comparison experiment A & B

6.5 Effect of salt

The effect of salts added to the surfactant solution can be determined by comparing experiment B and C. Both used H_2O as carrier, but in experiment C this had 1 weight percent calcium chloride added to it, to mimic seawater concentrations of calcium. The back pressure is equal at 10 bar, and the gas is CO_2 for both experiments. In experiment B the solubility effects of carbon dioxide were not taken into account, but this effect was accounted for in experiment C.

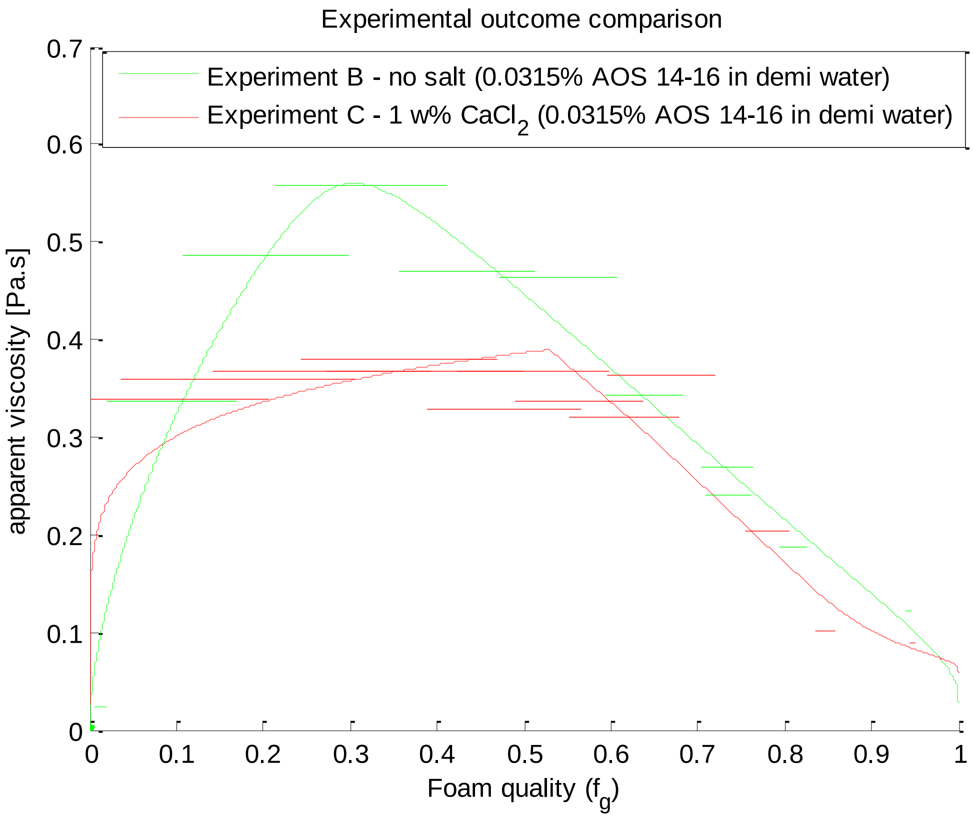

Figure 89: Effect of salt. Experiment B – 0.0315% AOS 14-16 in H_2O, Experiment C – 0.0315% AOS 14-16 in H_2O with 1w% $CaCl_2$

As explained in section 4.4.2 it is believed calcium ions can replace sodium ions present in the AOS surfactant. Sodium has one positive charge, but calcium has two. This means one calcium ion can be bound to two surfactant tails, which reduces the surfactant effectiveness. In the comparison shown in Figure 89 it can indeed be observed that the experiment without $CaCl_2$ produced a stronger foam for low to medium foam qualities, while there appears to be very little or no difference for high foam qualities.

If it is assumed the foam films are thin, a speculative theory explaining this behavior could be the stabilization of the interfaces in close proximity. The added surfactant tail to the surfactant molecule causes steric repulsion to increase, which is a dominant stabilization force for common black films. For both experiments fmdry is approximately equal as shown in Table 17. This is unexpected as it can be observed in Figure 89 the quality below which foam collapses is different in both experiments.

	Experiment B (no salt)	Experiment C (1w% $CaCl_2$)
fmmob	$6.57\cdot10^{4}$	$4.69\cdot10^{4}$
epdry	$4.09\cdot10^{2}$	$2.03\cdot10^{5}$
fmdry	$3.38\cdot10^{-1}$	$3.35\cdot10^{-1}$
fmcap	$3.49\cdot10^{-4}$	$1.86\cdot10^{-4}$
epcap	$5.00\cdot10^{-1}$	4.99

Table 17: Estimated parameter comparison experiment B & C

At high pressure, experiments have been performed that allow seawater to be compared to pure H_2O. This is shown in Figure 90.

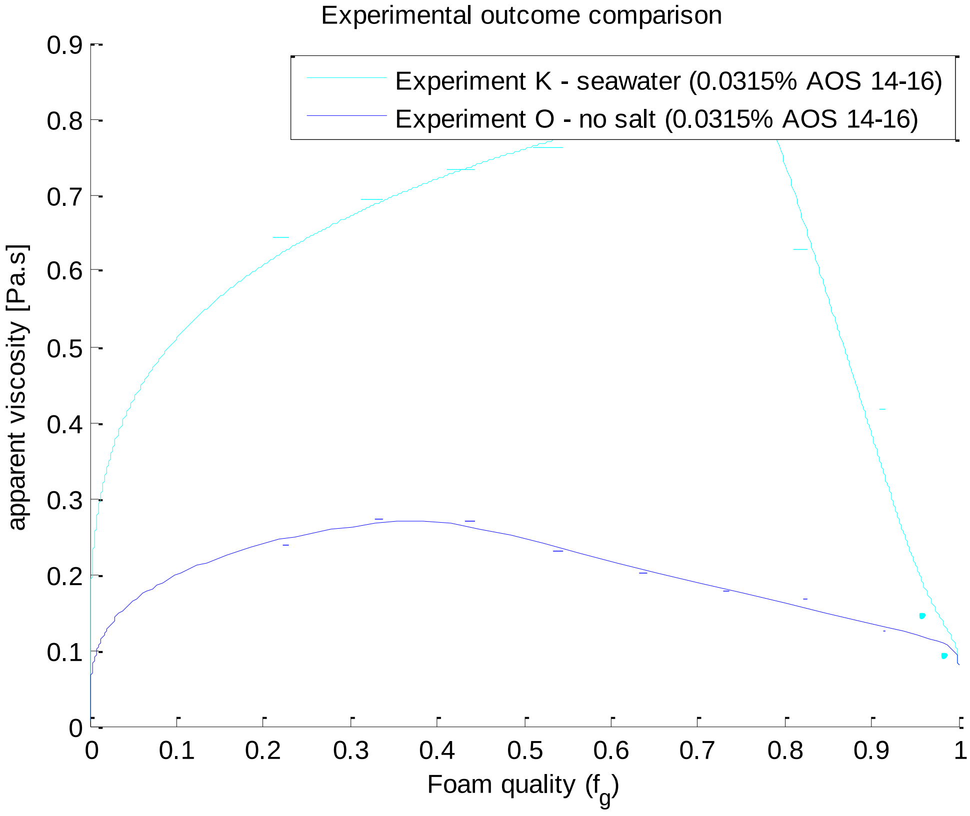

Figure 90: Effect of salt. Experiment K – 0.0315% AOS 14-16 in Seawater, Experiment O – 0.0315% AOS 14-16 in H_2O

Seawater created a much stronger foam than H_2O. This is opposite to what was observed before, however the sharp decline in viscosity after a certain gas fraction is equal for both salt-containing solutions. The addition of more ions has a positive effect on foam strength.

A possible explanation is the decreased IFT when adding salts (Figure 25 on page 67). Furthermore, CMC shifts to a lower concentration. A decrease in IFT means a higher bubble density which causes a higher foam viscosity. Calcium ions in the solution can cause increased foamability. Why Calcium enhances foamability is not exactly understood.

	Experiment K (seawater)	Experiment O (no salt)
fmmob	$1.19 \cdot 10^{5}$	$3.56 \cdot 10^{4}$
epdry	$1.68 \cdot 10^{4}$	$1.63 \cdot 10^{2}$
fmdry	$2.74 \cdot 10^{-1}$	$3.64 \cdot 10^{-1}$
fmcap	$3.11 \cdot 10^{-4}$	$1.33 \cdot 10^{-4}$
epcap	2.77	2.30

Table 18: Estimated parameter comparison experiment K & O

Another set of experiments that can be compared are experiments A and E. They are both conducted at room temperature, with a back pressure of 20 and 10 bar respectively. The flow rate for Experiment A is 1 mL/min, and for Experiment E is 0,5 mL/min. The comparison is visualized in Figure 91.

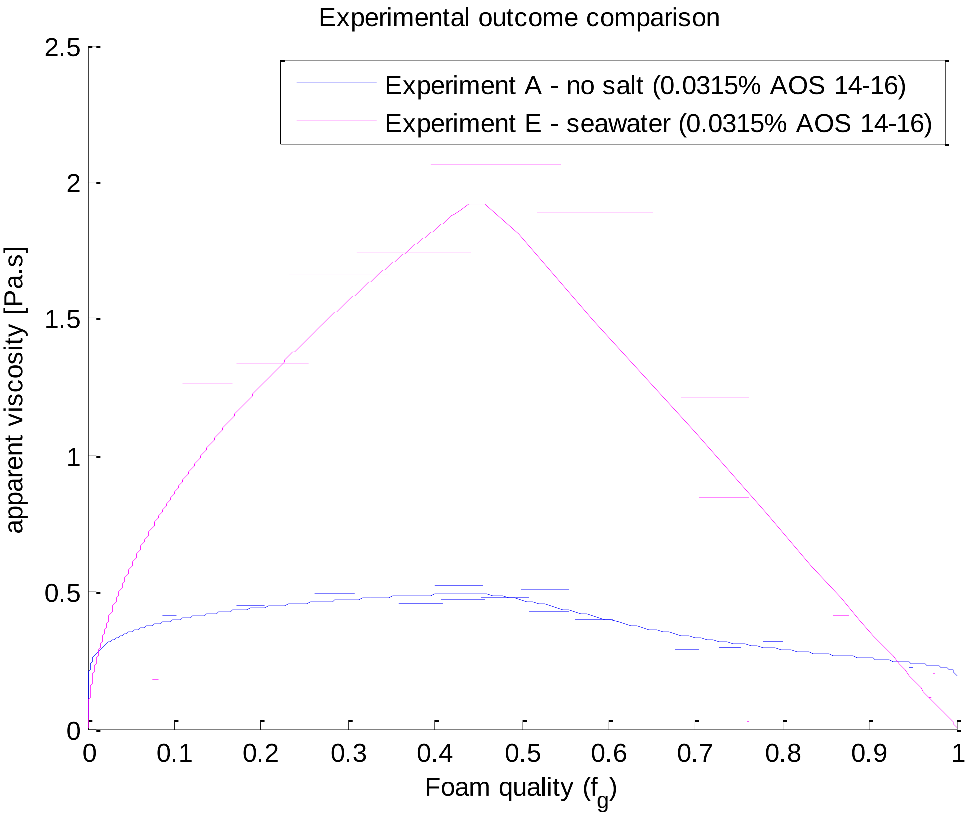

Figure 91: Effect of salt. Experiment A – H_2O, Experiment E – Seawater

Similar to the previous comparison the seawater foam is stronger in this case as well. Especially when considered the seawater experiment is conducted at a flow rate of 0,5 mL/min and shear thinning might occur, the difference becomes even larger. The fitted foam behavior is similar to that of experiment K, with a curved incline until a maximum is reached, followed by a fairly sharp decrease.

	Experiment A (no salt)	Experiment E (seawater)
fmmob	$4.11 \cdot 10^{4}$	$2.33 \cdot 10^{5}$
epdry	$9.11 \cdot 10^{2}$	$1.15 \cdot 10^{4}$
fmdry	$3.34 \cdot 10^{-1}$	$2.79 \cdot 10^{-1}$
fmcap	$2.11 \cdot 10^{-4}$	$3.75 \cdot 10^{-4}$
epcap	4.99	$7.55 \cdot 10^{-1}$

Table 19: Estimated parameter comparison experiment A & E

6.6 Effect of surfactant concentration

The first comparison which shows the effect of changing concentration is done by comparing experiments G, H and I. These tests are performed with a seawater carrier at a temperature of 80 degrees Celsius and a back pressure of 80 bar. The fits of experiments H and I have been improved as explained in section 6.1. Figure 92 shows the comparison of the processed results.

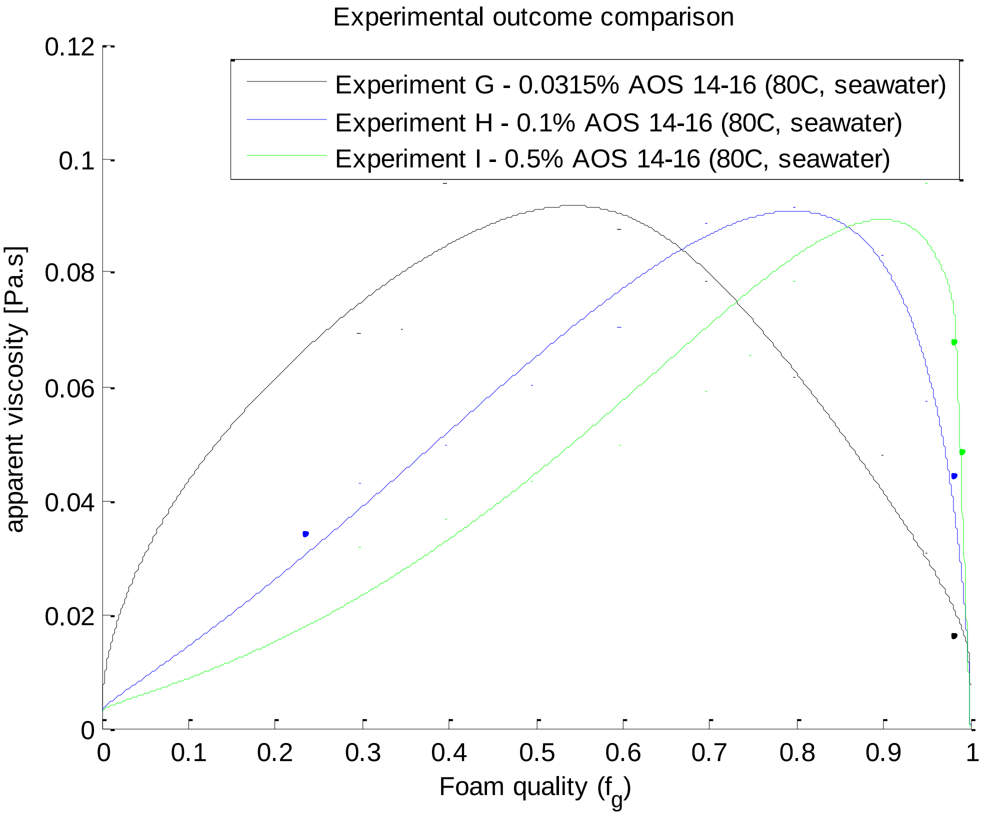

Figure 92: Effect of surfactant concentration. Experiment G: 0.0315% AOS 14-16 – Experiment H: 0.1% AOS 14-16 – Experiment I, 0.5% AOS 14-16, all at 80˚C

The main observation is that the maximum steady-state pressure drop does not increase with increasing concentration. The quality at which this maximum viscosity is achieved, increases with increasing surfactant concentration. All concentrations are above CMC at room temperature (Figure 25, page 67). If the surfactant concentration is below CMC, bubble density is strongly reliant on surfactant concentration. Above CMC this effect is less pronounced (Simjoo, 2012). The elevated temperature has shifted CMC towards a higher concentration, which could have caused this effect to be more pronounced in these experiments.

At increased surfactant concentration the foam gains stability at higher foam qualities. There is only a limited amount of liquid phase present for high quality foams. This means the ratio of gas-liquid interface to liquid volume is high if the bubble density stays the same. An increased surfactant concentration allows a larger interfacial area to be saturated with surfactant. In addition, steric repulsion increases with surfactant concentration.

	Experiment G (0.315%)	Experiment H (0.1%)	Experiment I (0.5%)
fmmob	$7.70\cdot10^{3}$	$3.25\cdot10^{3}$	$4.30\cdot10^{3}$
epdry	$8.78\cdot10^{1}$	$2.51\cdot10^{1}$	$1.48\cdot10^{4}$
fmdry	$3.47\cdot10^{-1}$	$2.92\cdot10^{1}$	$2.71\cdot10^{-1}$
fmcap	$3.16\cdot10^{-5}$	$3.12\cdot10^{-5}$	$6.86\cdot10^{-5}$
epcap	$5\cdot10^{-1}$	$5.19\cdot10^{-1}$	$7.37\cdot10^{-1}$

Table 20: Estimated parameter comparison experiment G, H & I

The explanation for foam behaviour at high liquid fractions is less straightforward. For a certain foam quality, the high-concentration surfactant causes a weaker foam. It is difficult to confidently describe why this is the case, as there is only very limited data available for this phenomenon. If above CMC, the micelles might have a destabilizing effect on the lamellae. However, this is not likely because the micelles are smaller than even very thin lamellae. A plausible explanation could be a decrease in surface viscosity because of the surfactant concentration increase. This causes lamellae to experience less drag, and can allow for more lamellae to be mobilized.

The effect of changing concentration has also been observed at 25 degrees Celsius. The results are compared in Figure 93.

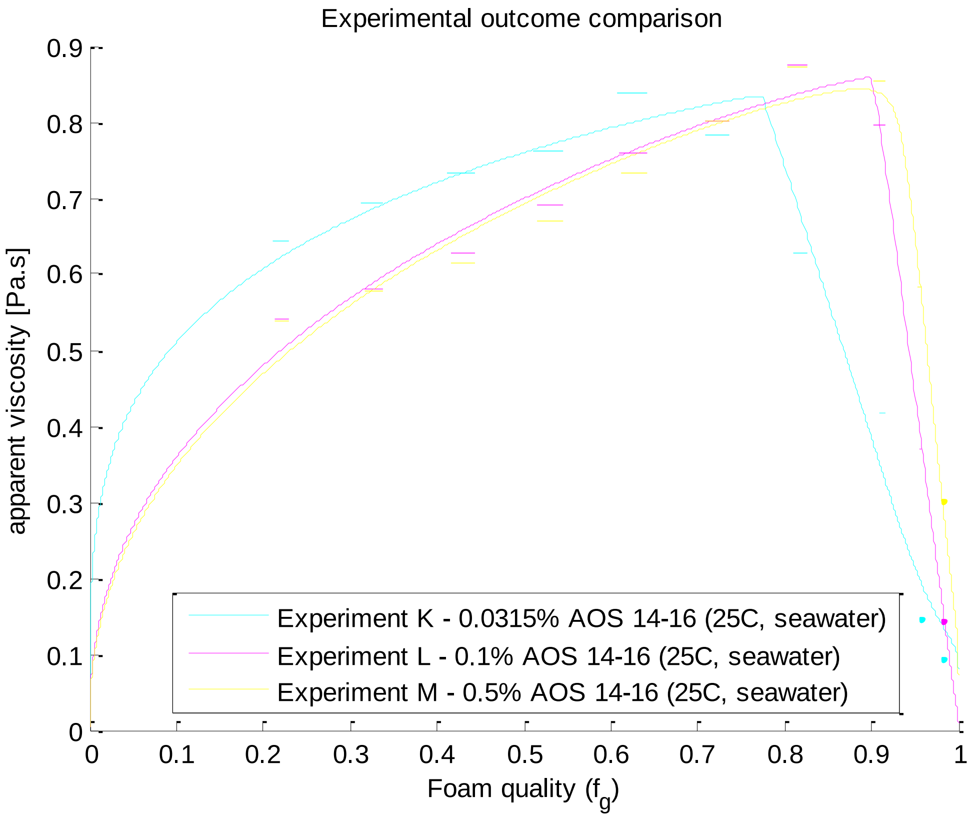

Figure 93: Effect of concentration. Experiment K: 0,0315% AOS 14-16 – Experiment L: 0,1% AOS 14-16 – Experiment M: 0,5% AOS 14-16

The differences in the results for different concentrations appear to be smaller than for those conducted at high temperature. As this experiments use AOS 14-16 in pure water, it is known that the surfactant concentration of experiment K (0,0315%) is slightly below CMC, while the concentrations of experiments L and M are above CMC. It is observed there is almost no difference between the viscosities of the latter two experiments, which confirms the theory that the relationship between surfactant concentration and CMC is very important.

The last observation from the comparison of experiments L and M, is that increasing the surfactant concentration beyond CMC does not significantly change foam behaviour.

	Experiment K (0.0315%)	Experiment L (0.1%)	Experiment M (0.5%)
fmmob	$1.20 \cdot 10^{5}$	$6.09 \cdot 10^{4}$	$6.78 \cdot 10^{4}$
epdry	$1.69 \cdot 10^{4}$	$4.96 \cdot 10^{4}$	$5.69 \cdot 10^{2}$
fmdry	$2.74 \cdot 10^{-1}$	$2.49 \cdot 10^{-1}$	$2.39 \cdot 10^{-1}$
fmcap	$3.11 \cdot 10^{-4}$	$3.19 \cdot 10^{-4}$	$2.82 \cdot 10^{-4}$
epcap	2.77	1.19	1.11

Table 21: Estimated parameter comparison experiment K, L & M

6.7 Difference between carbonate and sandstone

It is not possible to properly compare carbonate and sandstone experiments, as the surfactants and surfactant concentrations used for sandstone and carbonate experiments are not equal. Figure 94 compares the sandstone experiment (O), with the Chalk (P) and Limestone (R) experiment. The obtained results are very different. The foam viscosity in Chalk is far above that of the other experiments, as is also shown by the high *fmmob* in Table 22. In this experiment foam also collapses much faster compared to the other experiments. The smoothest transition is encountered in the sandstone. *epcap* is very high for all model fits. Experiment R, which is an experiment performed on limestone, produced a very weak foam.

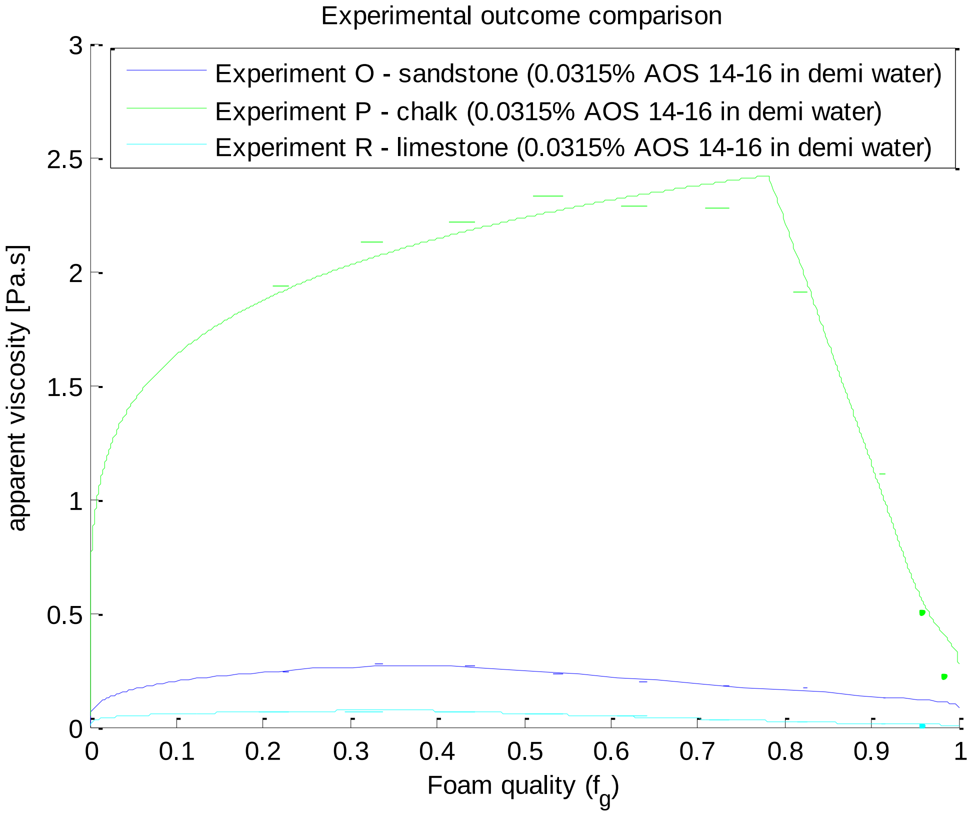

Figure 94: Effect of rock type: Experiment O - Sandstone, Experiment P - Chalk, Experiment R - Limestone

	Experiment O (SST)	Experiment P (Chalk)	Experiment R (Limest)
fmmob	$3.56 \cdot 10^{4}$	$3.34 \cdot 10^{5}$	5.7810^{3}
epdry	$1.63 \cdot 10^{2}$	$1.58 \cdot 10^{5}$	$8.91 \cdot 10^{4}$
fmdry	$3.64 \cdot 10^{-1}$	2.4210^{-1}	$4.60 \cdot 10^{-1}$
fmcap	$1.33 \cdot 10^{-4}$	$1.03 \cdot 10^{-3}$	$3.8 \cdot 10^{-5}$
epcap	2.30	3.93	3.37

Table 22: Estimated parameter comparison experiment O, P & R

6.8 Effect of nanoparticles

The effect of nanoparticles added to the carrier fluid can be determined by comparing experiment N and O. Both used a pure H_2O carrier, in case of experiment N with 5 g nanoparticles per litre. The back pressure is equal at 80 bar, using N_2 gas for both experiments.

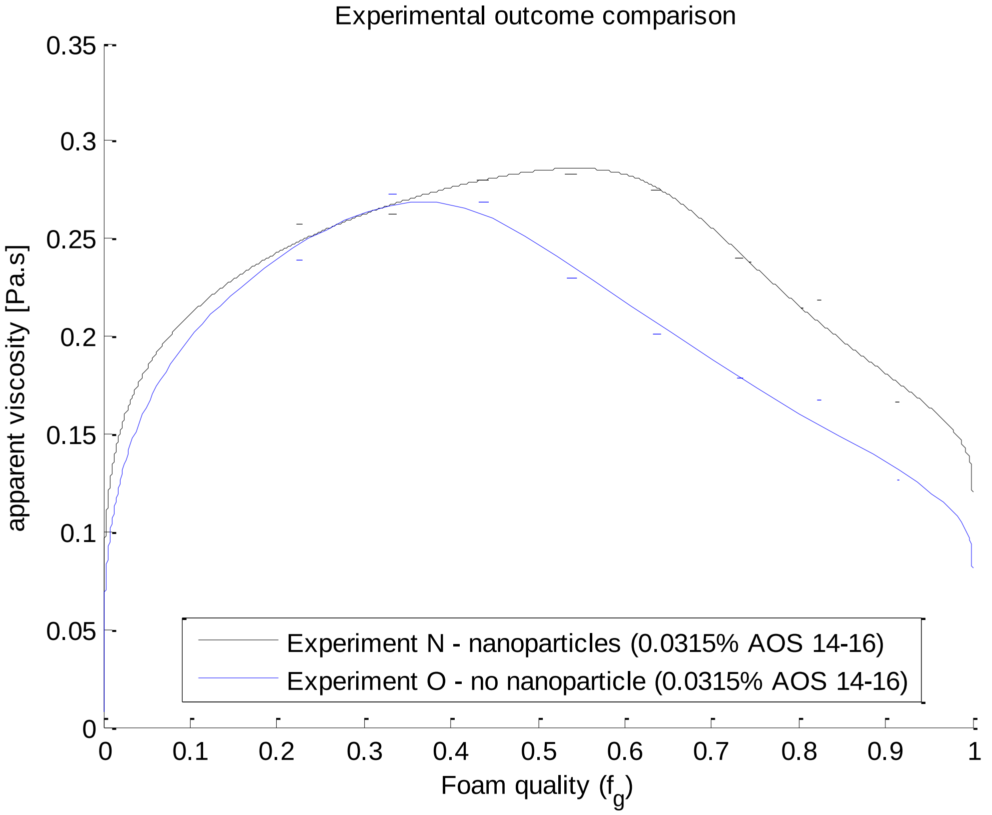

Figure 95: Effect of nanoparticles. Experiment N - with nanoparticles, Experiment O - no nanoparticles

Both experiments show similar behaviour in the low-quality regime. However, distinct differences are visible in the high-quality regime. Both the transitional foam quality and maximum achieved viscosity are higher for enhanced foam. This is an indication of the stabilizing effect of nanoparticles, such as slowing down drainage and lamella-bridging by wetting particles.

The increased stability is more pronounced at higher foam qualities. This could be related to the thickness of the foam films. If the lamellae are thick, the particles are smaller than the lamellae thickness. Therefore lamella-bridging is not occurring. Secondly, this increased stability at higher foam qualities could be due to the plateau border size. For smaller plateau border, the particle size relative to the border size is larger. This causes more resistance to flow compared to the situation where the particle size is small compared to the border size.

Even though the maximum achievable viscosity is only increased with approximately 15% by addition of nanoparticles, this viscosity occurs at a higher foam quality. This means less surfactant is required, which can aid in providing an economical field-scale solution.

	Experiment N (NP)	Experiment O (no NP)
fmmob	$3.75 \cdot 10^4$	$3.56 \cdot 10^5$
epdry	$1.28 \cdot 10^2$	$1.63 \cdot 10^4$
fmdry	$3.37 \cdot 10^{-1}$	$3.64 \cdot 10^{-1}$
fmcap	$1.32 \cdot 10^{-4}$	$1.33 \cdot 10^{-4}$
epcap	3.60	2.30

Table 23: Estimated parameter comparison experiment N & O

6.8.1 Nanoparticles in carbonates

The behaviour of nanoparticle foam has been studied in two different cores. A high permeable and high porosity chalk, and a low permeable limestone. In the highly permeable chalk from experiments P and Q a large difference improvement for nanoparticle foam was observed (Figure 96). Experiments on the low permeable limestone revealed no difference between nanoparticle and non-nanoparticle foam as can be seen in Figure 97.

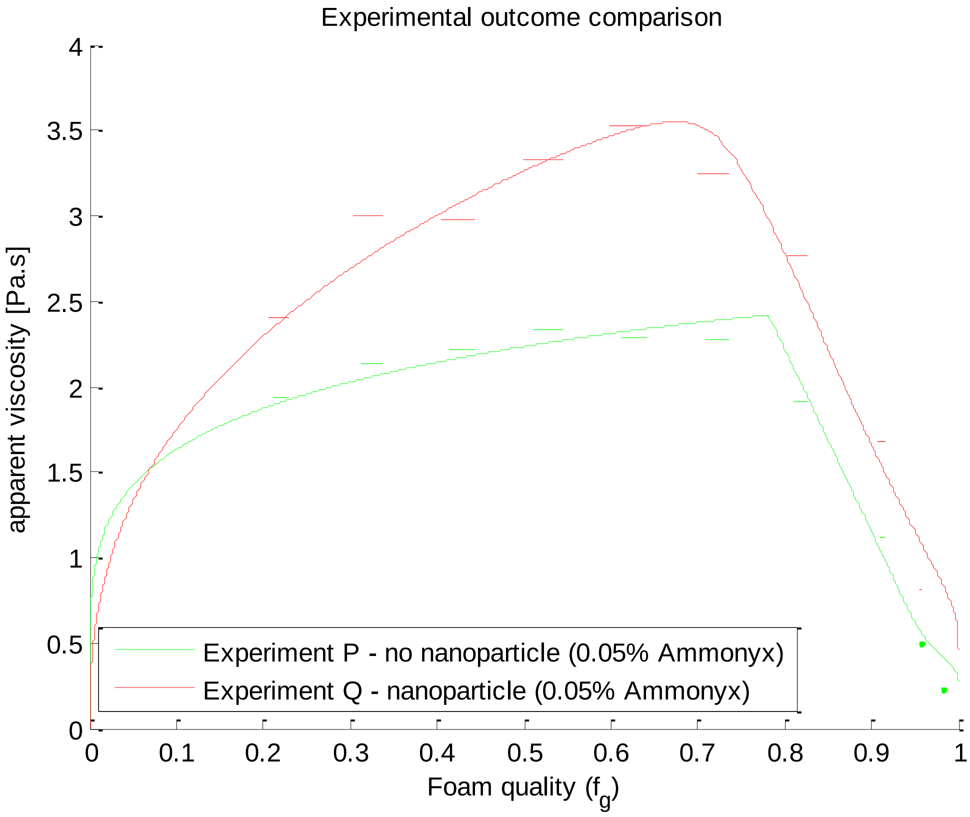

Figure 96: Effect of nanoparticles in Mergel Chalk. Experiment P - without nanoparticles, Experiment Q - with nanoparticles

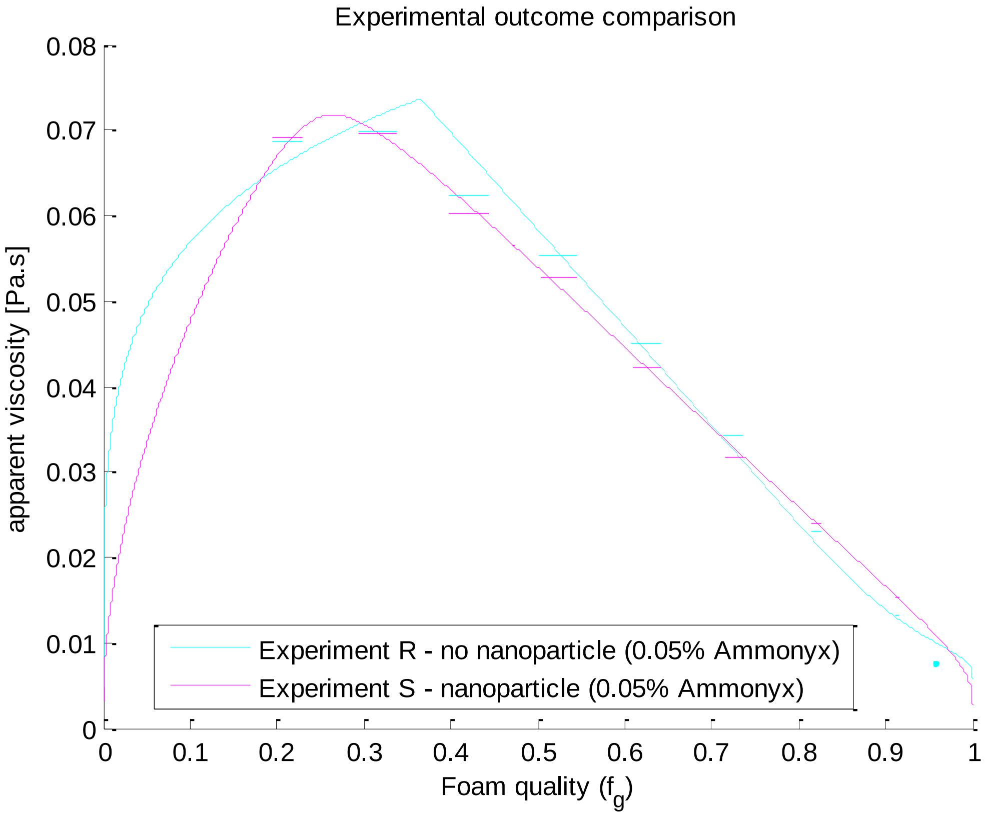

Figure 97: Effect of nanoparticles in Estaillades Limestone. Experiment R - without nanoparticles, Experiment S - with nanoparticles

It is important to analyse why adding nanoparticles worked for the chalk core flood, but did not improve foam viscosity for the limestone core flood. While conducting the experiment, the core-exiting foam was slightly grey, but the question is to what extend the nanoparticles had been able to travel through the core. SEM images have been taken from both cores to get an impression of the pore dimensions. The image from the chalk is shown in Figure 98 and the image taken from the limestone is shown in Figure 99.

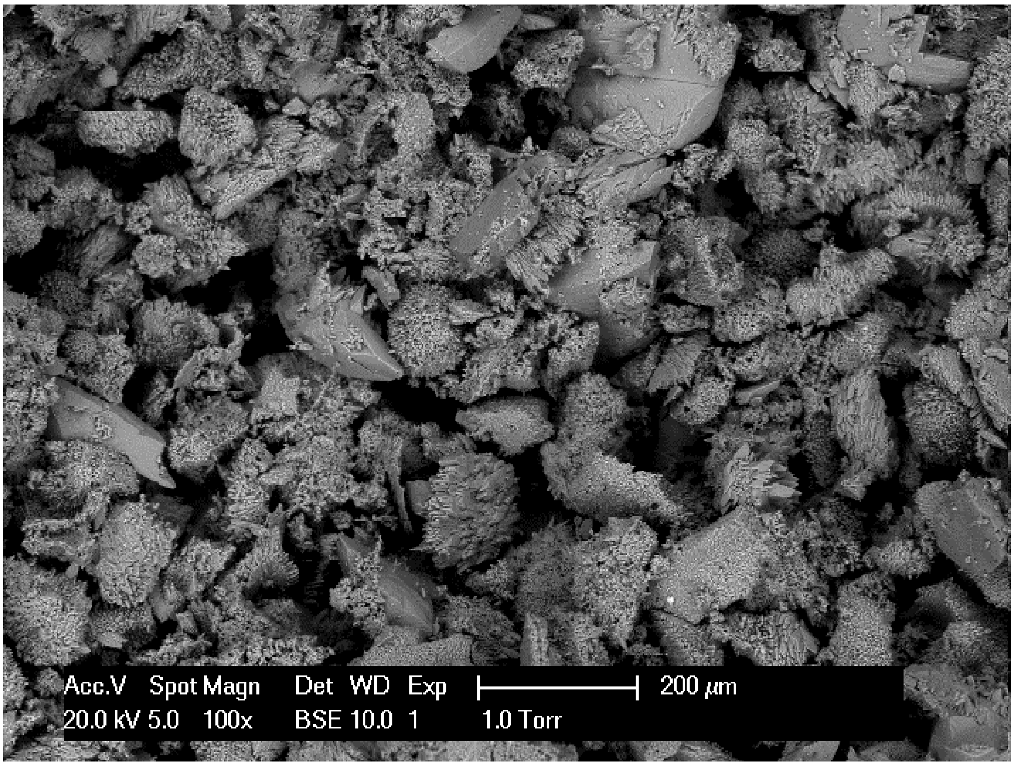

Figure 98: SEM image of Mergel Chalk

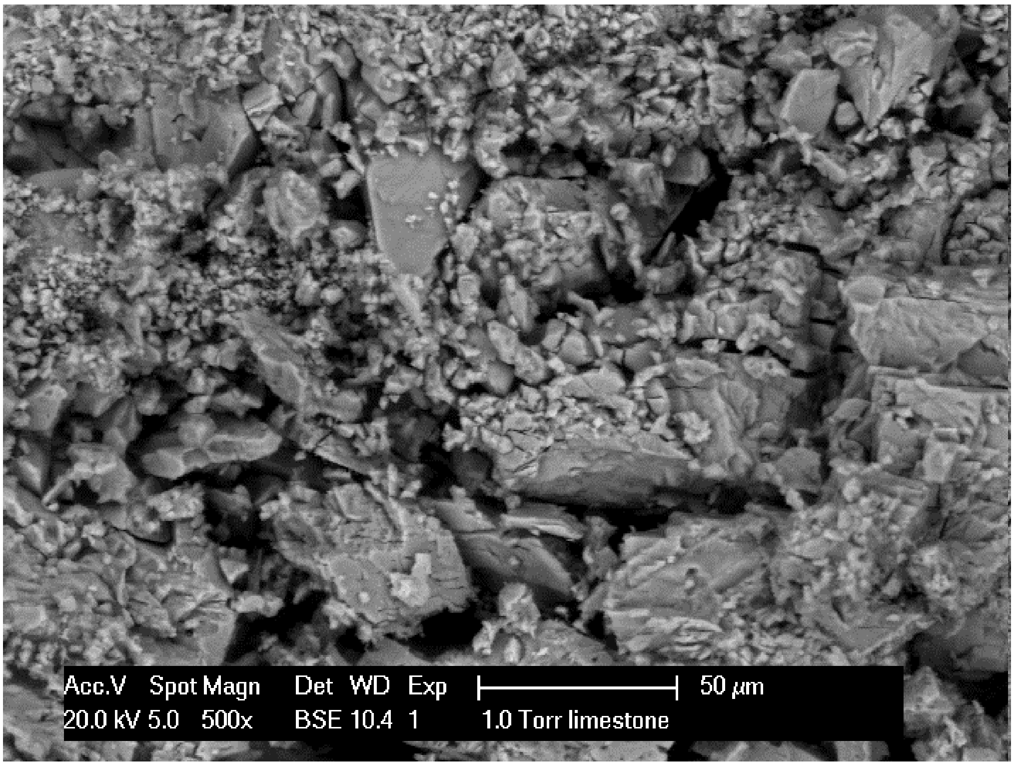

Figure 99: SEM image of Estadrailles Limestone

The images reveal the pores in the chalk being larger than the limestone. These images alone are not sufficient to determine pore size and geometry. However, the large visible pores in the limestone are roughly 5-10 µm. Figure 98 reveals multiple pores exceeding 50 µm for the chalk. This is also visible in Figure 100, which is a photograph taken of a thin section.

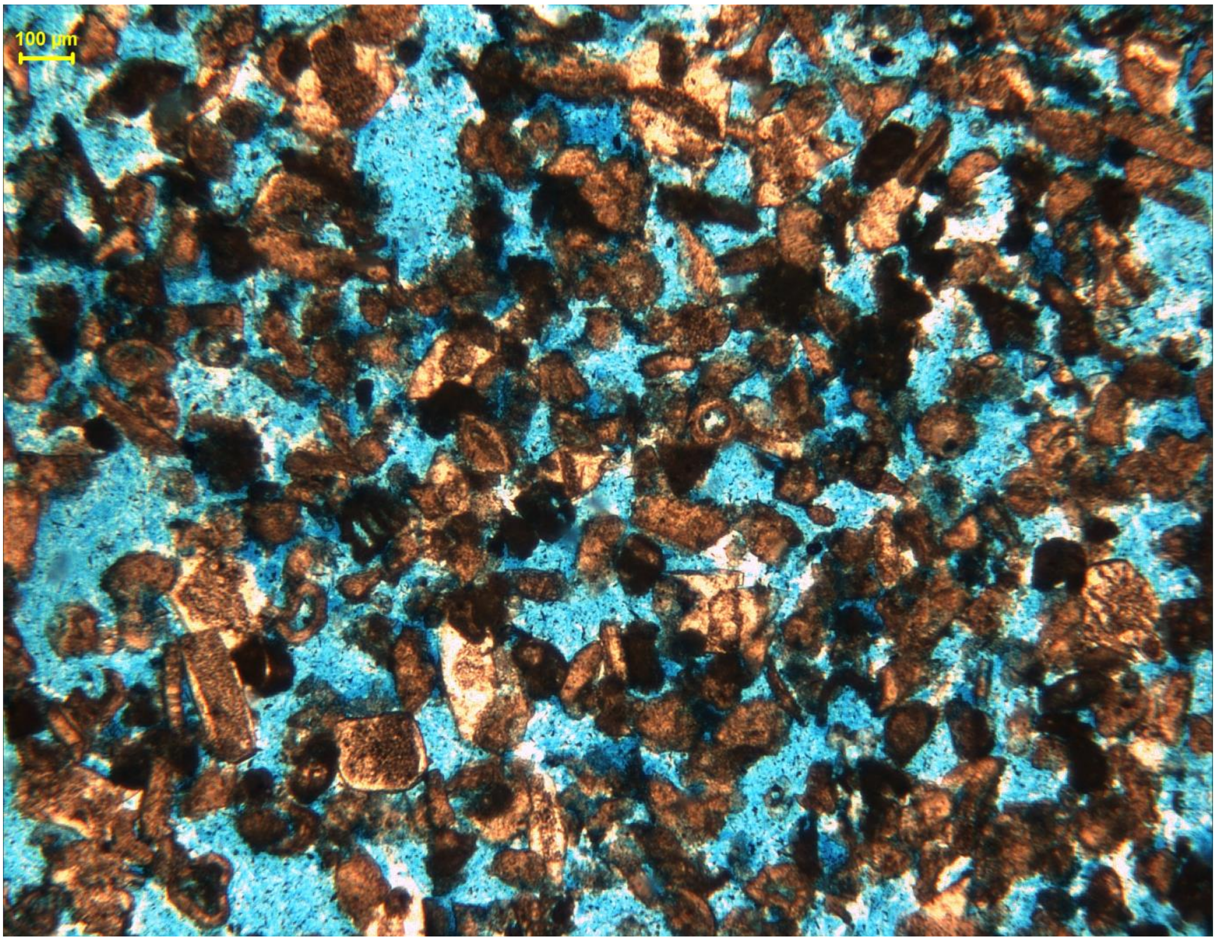

Figure 100: Thin section photograph of Mergel chalk. Pore space is blue.

Measurements performed on the size of the nanoparticles after milling and the ultrasound treatment indicated the size to be distributed around 150 nm, with agglomerated particles having a diameter around 1 µm or larger. These particles will be able to migrate through the chalk, as could be seen by the grey color of foam affluent during the experiments.

The small pore dimensions are a concern for the migration of solid nanoparticles. In order to get an estimation to what extend the particles have been able to travel through the limestone core, the core was cut in half to observe particle migration. The result is visible in Figure 101.

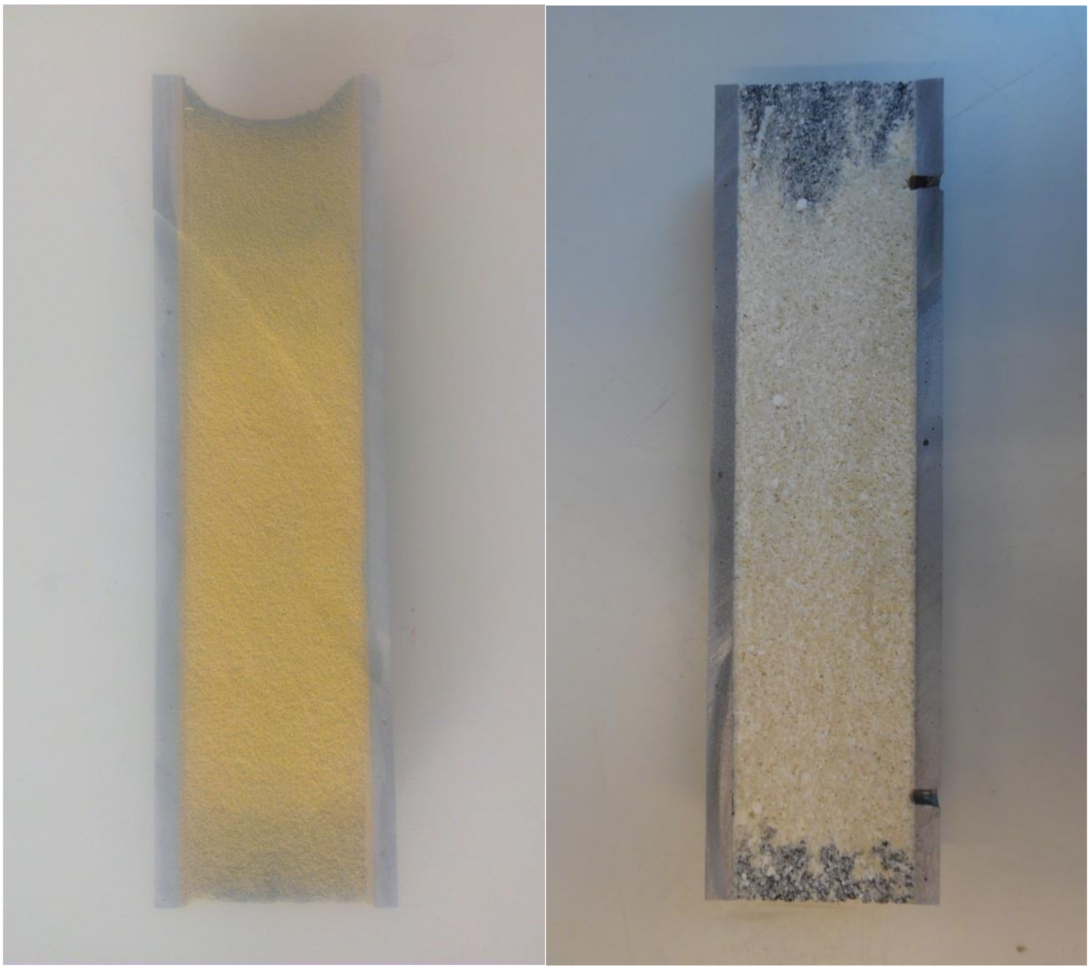

Figure 101: Left: chalk core after experiment. Right: limestone core after experiment

It can be observed that the nanoparticles have migrated approximately the same distance into the core. However, the chalk core shows a much more uniform nanoparticle front, whereas the nanoparticle front in the limestone appears to be more irregular. This observation is supporting the theory that there is heavy filtration due to the small limestone pore size. Only the largest connected pores offer paths for the particles to flow through. As soon as the particles are forced through the smaller pores they are filtered.

6.9 Applying nanoparticle-enhanced foam on a field scale

This study has been performed with the intention of helping to find a way to make foam an easily applicable field-scale solution for EOR. Many precautions had to be taken in order to successfully work with nanoparticles in the laboratory, because nanoparticles introduced some complications that are discussed earlier in this study. The extent to which these complications play a role in field-scale applications will be important in estimating if nanoparticle-foam can ever be applied in the field. This chapter discusses some observations from this study, and how they can be solved on a field-scale.

6.9.1 Nanoparticle preparation

Nanoparticle preparation on a field scale will be very different from preparation in a laboratory environment. The main resource for the production of this particle is plentiful available. In this study the nanoparticles were batch-produced with approximately 15 grams per batch. For it to become a field scale solution, nanoparticles will have to be prepared in larger batches with bigger equipment. However, preparing nanoparticles at a large scale will be expensive and energy-consuming. The yield of this process in a laboratory environment was very low. Less than 20% of the slurry entering the milling machine was retrieved as nanoparticle paste at the end of the process. The yield was low because it allowed the nanoparticle weight percentage to be known precisely. The sensitivity of the results with respect to nanoparticle concentration in the surfactant solution was not determined in this study. Future studies should attempt to determine this sensitivity, because if it is low the yield of nanoparticle preparation can be increased.

With decreasing particle size, the required energy to further break down the particle increases. In combination with the already low efficiency of milling and grinding processes, the required energy might be significant. To minimize milling cost and time, it is desired to use the largest particle size possible. As has been demonstrated in this study, nanoparticle size can be a limiting factor for the rocks to which this technology can be applied. In order to increase the viability of nanoparticle-enhanced foam the relationship between the pore size and geometry and the nanoparticle size still being able to flow through it should be determined.

Concluding: future research has to be conducted towards determining what particle sizes are practical for a certain application, to the particle concentration that can be used, and how to generate the nanoparticles as efficiently as possible.

6.9.2 Suspension stability in reservoirs

Surfactant aids in generating a stable suspension. In the experiments conducted in this study, the cores have been sufficiently flooded with surfactant to reach an equilibrium. This prevented further surfactant adsorption and caused the surfactant concentration to be constant throughout the experiments. In sandstone cores roughly 20 pore volumes were injected, while in carbonate cores 80 – 100 pore volumes were required. In an actual reservoir injecting that many pore volumes of surfactant is not an option. If the combination of nanoparticles and surfactant is injected into a reservoir, the surfactant will adsorb to the grains, destabilizing the nanoparticles. They will therefore precipitate and block the pores.

In order to prevent particle precipitation in the reservoir it is important to obtain insight in the stability criteria for these particles inside a porous media. As shown in Appendix B – Zeta potential measurements and as mentioned before, stability measurements have already been done to some extent. Insight has to be obtained on how to stay within the stability regions while keeping in mind the practical limitations field scale solutions bring.

6.9.3 Filtration

Dealing with filtration has been a challenging problem while conducting nanoparticle experiments. In this study a solution has been presented: The flow direction was reversed to wash away filtration by making use of a high pressure gradient.

If future studies indicate filtration is unavoidable, filtration is an issue that has to be dealt with downhole. Injecting from another point in a reservoir to reverse-flow the solution is not an option. First of all it will take a long time before the pressure gradient reaches the wellbore. Secondly, the flow rate of pressure differential such a technique can create is most likely not large enough.

In a well, the bottom hole pressure (BHP) can be manipulated by altering the specific weight of the borehole fluid. While injecting, the BHP is above reservoir pressure to force flow into the formation. If the BHP is set below reservoir pressure, the flow will be from the reservoir into the wellbore. When the differential is large enough, this might flush away filtration similar to the flow-reversal technique applied in the laboratory. This is shown in Figure 102. In addition, intervention techniques can remove cake from the wellbore, although many techniques do not reach into the rock formation.

Technologies to deal with filtration inside the wellbore or near-wellbore region already exist. However, the effectiveness of these techniques is not yet known. Reducing or preventing filtration in an actual wellbore can be subject of studies once this technology can be applied in real fields.

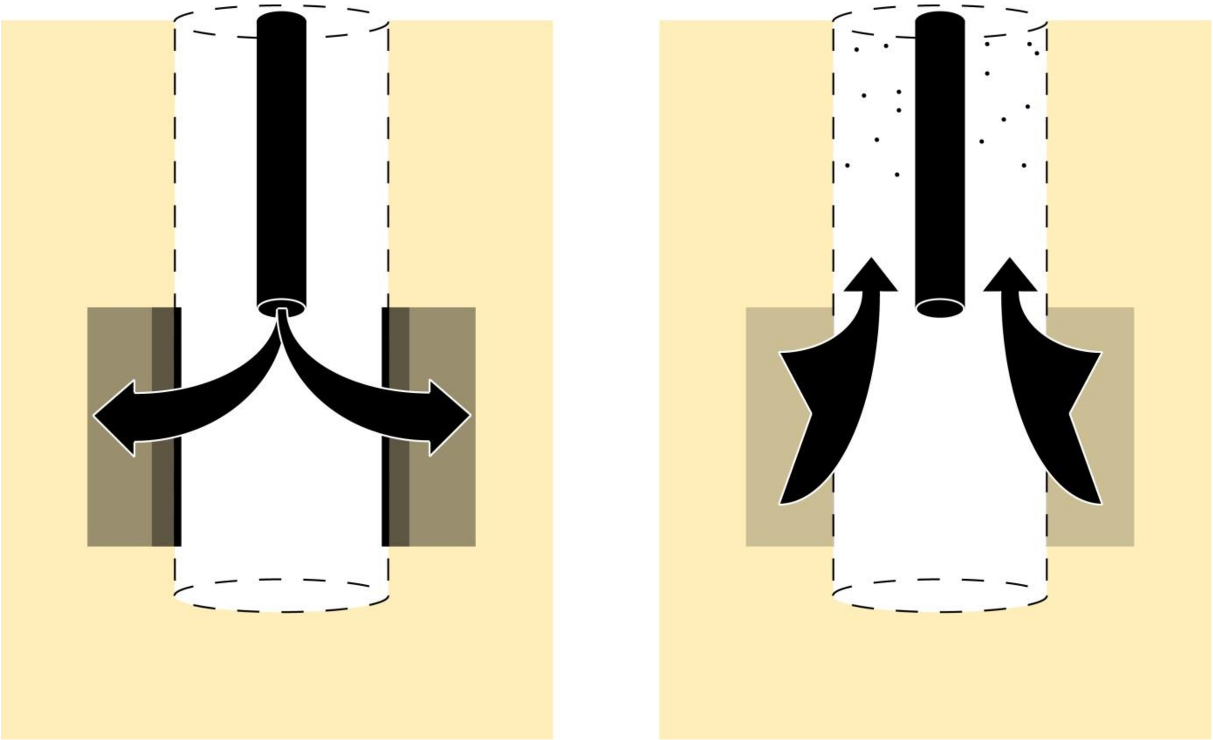

Figure 102: downhole filtration clean-up, on the left side a cake is forming because of particle filtration, on the right side the particles have been flushed away

7 Summary

The goal of this thesis, to assess the potential of these new nanoparticles to increase foam viscosity in a porous medium, has been achieved. A method was developed to reduce filtration effects which allowed the conduction of repeatable foam-scan experiments in a laboratory.

Through conduction of multiple core-flooding experiments it has been observed that adding nanoparticles with a concentration of 5 g/L did indeed enhance foam viscosity for cases where the nanoparticles were able to flow through the core. The particles were able to flow through the Bentheimer Sandstone with a permeability of around 2 Darcy, and the Mergel Chalk with a permeability of around 5,5 Darcy. The Estaillades Limestone with a permeability of around 0.1 Darcy proved to be difficult for the particles to flow through. Therefore the nanoparticle foam was not found to be more viscous when flowing through this medium.

Through the conduction of a secondary experiment drainage reduction was found to be a mechanism with which nanoparticles enhance foam strength. In an experiment where drainage was measured, nanoparticle foam was found to be up to 300% more wet than non-nanoparticle foam under the same conditions, indicating slower drainage. Therefore it is believed that also in a porous medium these particles help to reduce the rate at which foam lamellae are drained.

The effect on foam viscosity of changing salt concentration, temperature, gas, rock type and surfactant concentration has been identified and explained. A notable outcome is that increasing surfactant concentration above CMC did not enhance viscosity but only increased the gas fractional flow at which the highest viscosity occurred. Adding nanoparticles did enhance viscosity, in the case of the Chalk very significantly. Therefore it is believed there is great potential between the synergy of surfactants and nanoparticles. Rather than simply replacing surfactants, the new silica-based particle provides a mechanism which aids foam generation in a unique way.

8 Conclusion and recommendations

8.1 Conclusions

8.1.1 Nanoparticle-enhanced foam

- Strong foams can be made by using a mixture of nanoparticles and surfactant in both sandstone and carbonate rocks.
- The viscosity-increasing effect nanoparticles had on foam viscosity was larger for the chalk than it was for the sandstone.
- The nanoparticles had no foam-improving effect for the low-permeable limestone. This is likely caused by particle filtration.
- The reduction of drainage through foam films stabilized by nanoparticles are a likely mechanism to reduce lamella destruction by capillary suction.
- An experimental method to conduct reliable nanoparticle experiments has been developed.

8.1.2 General

- Increasing surfactant concentration did not increase the maximum foam viscosity, but shifted the point at which maximum foam viscosity was achieved to a higher gas fraction. This effect was more pronounced for higher temperatures.
- Using artificial seawater rather than pure H_2O increased foam viscosity considerably.
- High temperatures cause foam viscosity to decrease.
- A saline and high-temperature environment caused the nanoparticle suspension to destabilize, although this effect was not quantified in this study.

8.2 Recommendations

8.2.1 Recommendations for future research

- **Study the effect of nanoparticle concentration**

  In this study only one nanoparticle concentration was used. The aim of the next study should be to investigate the effect of different nanoparticle concentrations.

- **Determine under which conditions nanoparticle stability can be achieved.**

  For the silica-based particle to be successfully implemented in the field, particle stability should be achieved at in-situ conditions. It should be investigated how this can be achieved.

- **Explore the effect of nanoparticles in a saline environment**

  In this study the effect of adding surfactant in a saline environment was observed: no maximum viscosity increase was found. Due to stability issues the effect of nanoparticles could only be demonstrated in pure H_2O, where it could (significantly) enhance foam properties. If it is possible to stabilize the particle in a saline environment, where it still can enhance foam strength like it did as in the case for pure H_2O, a giant leap is done to bringing nanoparticles to the field.

- **Determine the foam-enhancing effect of the nanoparticle in presence of oil.**

  In a real field application, foam stability in presence of oil has to be achieved. Therefore, one of the next steps in the continuation of this thesis is to investigate potential beneficial effects of applying this type of nanoparticle in presence of oil.

- **Repeat the experiments for (supercritical) CO_2**

  CO_2 has some preferential characteristics over N_2 when displacing oil, but performing experiments with supercritical CO_2 is challenging.

- **Determine the relationship between the pore dimensions and particle size, for which the particles can still migrate through the core.**

  As has been observed in this study the particles were not able to migrate through the limestone. If the particles would be smaller they will be able to migrate through. In addition, perhaps there is a relationship between particle size and foam viscosity gain. If there is, it could help explain what mechanisms allow the particles to enhance foam.

8.2.2 Recommendations for setup enhancements

- **The setup should be fully remote-controlled.**

  Opening hours of the laboratory are restricted, which limits the amount of time the setup is physically accessible. During conduction of the experiments it was found that the productivity increased by a large amount when being able to remotely access the experiment-controlling computer. By using a secure internet connection and a software package (in this case Google Desktop) the computer placed in the laboratory could be accessed remotely with the use of a login name and password. By using a webcam it was possible to keep a good overview of the setup.

- **Make use of smart-monitoring**

  The computer receives measurements and controls gas and liquid flow. In this study the measurements were processed manually, and the gas and liquid flow rate were set manually. There are simple but labour intensive tasks that can be easily done by a computer. Algorithms are able to recognize when core conditions have achieved a steady state, and a simple script will be able to process and store data, and afterwards give the input for a new measurement to be conducted. This allows the experimental setup to complete the experiments without human intervention and without the risk of human errors, allowing for 24/7 experiment conduction.

  In addition to a productivity increase smart-monitoring will increase the safety in the laboratory. The strategic placement of remote-controlled valves can shut down the system immediately in case of any leak or other unexpected event. Not only do computers have a faster response time than humans, the computer will also always be there and scanning multiple times per second for hazardous conditions.

- **Increase the standard spacing between internal pressure tabs to 13 cm**

  When conducting nanoparticle experiments the entrance to the core will be susceptible to filtration effects. The external pressure gauges can therefore not be used for a reliable viscosity determination, as the permeability at the exit is decreasing. The internal pressure gauges should measure the pressure drop over the largest interval possible to give the most accurate result. It has been found that at a spacing of ~2 cm between the core entrance and first pressure tab is enough to avoid inaccuracies due to filtration.

- **Fortify the position of the transfer vessel on the stirrer**

The transfer vessel is a heavy steel cylinder filled with highly pressurized liquid and potentially gas. The electromagnetic stirrer on which it was placed had to carry this heavy load, for which it was possibly not designed. For safety reasons it would be advisable to support the weight of the transfer vessel, to avoid it from falling over and damaging people or equipment.

- **Use two gas flow controllers**

  Because of the high pressure and high flow rate, the gas flow feed to the system has to be both accurate and able to deliver a broad range of gas flows. The current equipment was not able to do this, as the minimal gas flow was 8 mLn/min. Therefore measurements at gas fractions below 0.2 could not be taken. A dual gas flow controller setup working in different ranges would be able to accurately deliver both high and low gas flows while still being remotely controllable.

- **Use a different back pressure**

  The weakest point of the setup is the back pressure. The pressure drop from 80 bar to atmospheric pressure is very large. Therefore, the pressure gradient that drives flow through the membrane is very high. As soon as the membrane allows flow, foam rapidly flows through the valve, which causes the pressure at the core outlet to drop slightly below the set value. These little vibrations induce a measurement error. In addition, the large pressure differential causes increased wear on the sensitive components. A 2-stage approach, where the pressure is firstly reduced to for example 60 bar, and then to atmospheric pressure, would be able to reduce these pressure fluctuations while reducing wear. Alternatively, digital feedback-controlled back pressures are available.

- **Standardize experimental procedures and create a database**

  The Delft University of Technology has a great laboratory with solid equipment and a capable technical staff. This allows for the conductance of many experiments. However, due to inefficiencies a lot of valuable data is lost, or difficult to find for other researchers. In addition the experimental procedures are not standardized which makes it difficult to compare one experiment with another. In the early stage of this study some experiments have been performed in absence of nanoparticles. If there would have been a database with all past experiments and their results, some of these might have been unnecessary. Especially if the way core-flooding experiments are performed is standardized it would be easy to compare experiments and contribute to the database.

Acknowledgements

I would like to use this opportunity to express my appreciation to my committee chairman Mr. Farajzadeh. I am very thankful for him for giving me the opportunity to work on this very interesting topic. Whenever I had a question Mr. Farajzadeh was not only able to provide the answer, but also give an explanation which was so clear I wondered how I haven't thought of that myself. Without his supervision and knowledge this study would never have been possible.

Secondly, I would like to thank my daily supervisor Mr. Eftekhari for his excellent mentorship. Despite his very busy schedule he was always able to find time to help me with any issues I faced. His enthusiasm for the project made him a great pleasure to work with, and helped bringing my thesis to a higher level.

I would like to thank my other graduation committee members Mr. Rossen, Mr. Vincent-Bonnieu and Mr. Maghami Nick for attending my presentation, reading my thesis and evaluating my work. I feel honoured they created the opportunity within their busy academic and corporate schedules to do so.

Lastly, the experimental work is a vital component of this study. Without the technical supervision and assistance of Mr. Slob I would never have been able to complete my experiments.

Bibliography

Abbaszadeh, M., Korrandi, A. K. N., Lopez-Salinas, J. L., Rodriguez- de la Garza, F., Pino, A. V., & Hirazaki, G. (2014). Experimentally-Based Empirical Foam Modeling. SPE Improved Oil Recovery Symposium, Tulsa, Olkahoma.

Aroonsri, A., Worthen, A., Hariz, T., Johnston, K., Huh, C., & Bryant, S. (2013). Conditions for Generating Nanoparticle-Stabilized CO 2 Foams in Fracture and Matrix Flow. *Society of Petroleum Engineering Annual Technical Conference and Exhibition, New Orleans, Louisiana*, (September).

Binks, B. P. (2002). Particles as surfactants - similarities and differences.

Boeije, C. S., & Rossen, W. R. (2013). Fitting Foam Simulation Model Parameters to Data. St. Petersburg, Russia: 17th European Symposium on Improved Oil Recovery.

Chen, M., Yortsos, Y. C., California, S., & Rossen, W. R. (2004). SPE 90939 A Pore-Network Study of the Mechanisms of Foam Generation.

Cheng, L., Reme, A. B., Shan, D., Coombe, D. A., & Rossen, W. R. (2000). Simulating Foam Processes at High and Low Foam Qualities. Society of Petroleum Engineers.

Computer Modeling Group. (2007). STARS user's guide. Calgary.

Deffeyes, K. S. (2001). *Hubbert's Peak*. Princeton University Press.

Dholkawala, Z., Sarma, H., & Kam, S. (2007). Application of fractional flow theory to foams in porous media. *Journal of Petroleum Science and Engineering*, *1*(2), 152–165.

Espinosa, D., Caldelas, F., Johnston, K., Bryant, S. L., & Huh, C. (2010). Nanoparticle-Stabilized Supercritical CO 2 Foams for Potential Mobility Control Applications. *SPE Improved Oil Recovery Symposium, Tulsa, Oklahoma*.

Falls, A. H., Co, S. D., Hlrasakl, G. J., Patzek, T. W., Gauglltz, D. A., Miller, D. D., … Co, D. (1988). Development of a Mechanistic Foam Simulator : The Population Balance and Generation by Snap-Off. *SPE journal*, (August).

Freedman, V. L., Zhang, Z. F., & Zhong, L. (2009). *Foam Transport in Porous Media – A Review*.

Gauglitz, P. A., & Rossen, W. R. (1990). Percolation Theory of Creation and Mobilization of Foams in Porous Media. *AiChE Journal*, *36*(8), 1176–1188.

Goodwin, J. (2009). *Colloids and Interfaces with Surfactants and Polymers*. Wiley.

Green, A. J., Littlejohn, K. a., Hooley, P., & Cox, P. W. (2013). Formation and stability of food foams and aerated emulsions: Hydrophobins as novel functional ingredients. *Current Opinion in Colloid & Interface Science*, *18*(4), 292–301. doi:10.1016/j.cocis.2013.04.008

Hunt, A. G. (2001). Applications of percolation theory to porous media with distributed local conductances. *Advances in Water Resources*, *24*, 279–307.

Kamiya, H., Gotoh, K., Shimada, M., Uchikoshi, T., Otani, Y., Fuji, M., … Miyahara, M. (2012). *Fundamentals chapter 3: Characteristics and Behaviour of Nanoparticles and its dispersion systems* (pp. 115–176).

Khatib, Z. I., Hirasaki, G. J., & Falls, A. H. (1988). Effects of Capillary Pressure on Coalescence and Phase Mobilities in Foams Flowing Through Porous Media. *SPE Reservoir Engineering*, (August), 919–926.

Kovscek, A. R. (1998). *Reservoir Simulation of Foam Displacement Processes*. Beijing: UNITAR International Conference on Heavy Oil and Tar Sands.

Lotfollahi, M., Farajzadeh, R., Delshad, M., Varavei, A., & Rossen, W. R. (2014). Comparison of Local-Equilibrium and Population-Balance Foam Models. *Journal of Petroleum Science and Engineering*.

Lyman, J., & Fleming, R. H. (1940). Composition of Seawaters. *University Press, Cambridge*.

Ma, K., Farajzadeh, R., Lopez-Salinas, J. L., Miller, C. a., Biswal, S. L., & Hirasaki, G. J. (2014). Non-uniqueness, Numerical Artifacts, and Parameter Sensitivity in Simulating Steady-State and Transient Foam Flow Through Porous Media. *Transport in Porous Media*, *102*(3), 325–348. doi:10.1007/s11242-014-0276-9

Ma, K., Lopez-salinas, J. L., Puerto, M. C., Miller, C. A., Biswal, S. L., & Hirasaki, G. J. (2013). Estimation of Parameters for the Simulation of Foam Flow through Porous Media . Part 1 : The Dry-Out E ff ect. *Energy & Fuels*.

Marinova, K. G., Gurkov, T. D., Dimitrova, T. D., Alargova, R. G., & Smith, D. (1998). Role of Oscillatory Structural Forces for Interactions in. Sofia, Bulgaria: Laboratory of Thermodynamics and Physico-Chemical Hydrodynamics, University of Sofia.

Mcelfresh, P., Wood, M., & Ector, D. (2012). Stabilizing Nano Particle Dispersions in High Salinity , High Temperature Downhole Environments. *Society of Petroleum Engineering International Oilfield Nanotechnology, Noordwijk, The Netherlands*, (June).

Mo, D., Jia, B., Yu, J., Liu, N., & Lee, R. (2014). Study Nanoparticle-Stabilized CO 2 Foam for Oil Recovery at Different. *Society of Petroleum Engineers Improved Oil Recovery Symposium, Tulsa, Oklahoma*, (April).

Nguyen, P., Fadaei, H., & Sinton, D. (2014). Nanoparticle Stablized CO 2 in Water Foam for Mobility Control in Enhanced Oil Recovery via Microfluidic Method. *Society of Petroleum ENgineers Heavy Oil Conference, Alberta, Canada*, (June).

Pickering, S. U. (1907). Emulsions. *Journal of the Chemical Society*, (91 (2001)), 2001–2021.

Ramirez, W. F., Marfoe, C. H., & Kazemi, H. (1987). Numerical Simulation of Foam Flow in Porous Media. Society of Petroleum Engineers.

Rossen, W. R. (n.d.). Snap-Off and Foam Generation in Porous Media.

Rossen, W. R. (1988). Theories on Foam Mobilization Pressure Gradient. *SPE/DOE Enhanced Oil Recovery Symposium Tulsa, Oklahoma, April 17-2*.

Rusanov, a. I., & Krotov, V. V. (2003). Gibbs Elasticity of Free Thin Liquid Films. *Doklady Physical Chemistry*, *393*(4-6), 350–352. doi:10.1023/B:DOPC.0000010341.98197.11

Schramm, L. L. (2005). Emulsions, Foams and Suspensions, Fundamentals and Applications. WILEY-VCH. doi:ISBN-13: 978-3-527-30743-2

Simjoo, M. (2012). *Immiscible Foam for Enhancing Oil Recovery*. Delft University of Technology.

Singh, S., & Mohanty, K. K. (2014). Synergistic Stabilization of Foams by a Mixture of Nanoparticles and Surfactants. *Society of Petroleum Engineers Improved Oil Recovery Syposium, Tulsa, Oklahoma*, (April). doi:10.2118/169126-MS

Span, R., & Wagner, W. (1994). A New Equation of State for Carbon Dioxide Covering the Fluid Region from the Triple-Point Temperature to 1100 K at Pressure up to 800 MPa. Bochum: Lehrstuhl für Thermodynamik, Ruhr-Universität Bochum.

Spencer, N., & Heuberger, M. P. (2009). Surfaces, Interfaces, and their Applications I, 262–275.

Stubenrauch, C., & Klitzing, R. Von. (2003). Disjoining pressure in thin liquid foam and emulsion films — new concepts and perspectives. *Journal of Physics: Condensed Matter*, *15*, R1197–R1232.

Tanzil, D., Hirasaki, G. J., & Miller, C. A. (2002). SPE 75176 Conditions for Foam Generation in Homogeneous Porous Media. *SPE Improved Oil Recovery Symposium, Tulsa, Oklahoma*.

Tzimas, E., Georgakaki, A., Garcia Cortes, C., & Peteves, S. D. (2005). *Enhanced Oil Recovery using Carbon Dioxide in the European Energy System*.

Ultrasonic Wet-Milling and Micro-Grinding. (2014). *Hielscher Ultrasound Technology*. Retrieved October 10, 2014, from http://www.hielscher.com/mill_01.htm

Verwey, E. J. W., & Overbeek, J. T. G. (1999). *Theory of the Stability of Lyophobic Colloids*. New York: Dover.

Woodcock, L. V., Dorfmuller, G., & Williams, G. (1987). Proceedings for workwhop at Centrum fur Interdizciplinare Forschung University Bielefield. *Lecture Notes Physics*, *November*(277), 113–124.

Yu, J, Liu, N., Li, L., & Lee, R. (2012). Generation of Nanoparticle-Stabilized Supercritical CO 2 Foams. *Carbon Management Technology Conference, Orlando, Florida*, (February).

Yu, Jianjia, Mo, D., Liu, N., & Lee, R. (2013). The Application of Nanoparticle-Stabilized CO 2 Foam for Oil Recovery. *Society of Petroleum Engineering International Symposium on Oilfield Chemistry, The Woodlands, Texas*, (April).

Yu, Jianjia, Wang, S., Liu, N., & Lee, R. (2014). Study of Particle Structure and Hydrophobicity Effects on the Flow Behavior of Nanoparticle-Stabilized CO 2 Foam in Porous Media. *Society of Petroleum Engineers Improved Oil Recovery Symposium, Tulsa, Oklahoma*, (April).

Appendix A – MATLAB scripts

Measurement processing

```
% The big coreflood analyzing Matlab Script
% This script works for Setup 1 and 2

%% Set experiment data parameters
RawData=xlsread('HP 0,0315AOS REFERENCE NANOPARTICLE.xlsx');
InletColumn = 5;
P3Column = 2;
QualityColumn = 1;
InternalColumn = 3;
ExternalColumn = 4;
GasFlowColumn = 6;

% Choose gas
Gas = 1;    % 1 = Nitrogen, 2 = CO2

% Some core constants
k = 1.78e-12;
A = (1/4)*pi()*0.038^2; % Cross sectional area in m2
L = [0.09 0.18]; % Core lenghts in m

% Experiment target total flowrate
Qtarget = 1.0; %ml/min
FlowmeterCorrection = 1.782;

%% Calculate pressure matrix
% Make pressure matrix with 3 rows: Inlet, Average and Outlet and convert
% to absolute pressure

Pressure = zeros(length(RawData),3); % Pressure in [bar]
Pressure(:,1) = RawData(:,InletColumn);
Pressure(:,2) = RawData(:,P3Column)+0.5*RawData(:,InternalColumn);
Pressure(:,3) = RawData(:,InletColumn)-RawData(:,ExternalColumn);
Pressure = Pressure+1;

%% Obtain compressible gas flow rates in core
% Calculate gas density in core. Matrix gets same size as Pressure matrix.
% Calculate compressibility based on appropriate EOS
Z = zeros(size(Pressure,1),size(Pressure,2));

if Gas == 1
    for x=1:size(Pressure,2)
        for y=1:size(Pressure,1)
            Z(y,x) = 
JacobsenStewart_N2(Pressure(y,x)*100000,(273+80))/JacobsenStewart_N2(100000
,(273));
        end
    end
end

if Gas == 2
    for x=1:size(Pressure,2)
        for y=1:size(Pressure,1)
            Z(y,x) = 
CO2GasDensity(273+80,Pressure(y,x)*100000)/CO2GasDensity(273,100000);
        end
    end
 end
```

```
%% Calculate solubility for case CO2
kh = 0.034;
GasFlow = zeros(size(Pressure,1),size(Pressure,2));
Quality = RawData(:,QualityColumn);

if Gas == 2
    S = zeros(size(Pressure,1),size(Pressure,2));
    CO2Density = zeros(size(Pressure,1),size(Pressure,2));
    Dissolved = zeros(size(Pressure,1),size(Pressure,2));

    VolumeDissolved = zeros(size(Pressure,1),size(Pressure,2));


    for x=1:size(Pressure,2)
        for y=1:size(Pressure,1)
            % Calculate solubility
            S(y,x) = kh*Pressure(y,x)/1000; % Solubility in [mol/mL]
            Dissolved(y,x) = Qtarget*(1-Quality(y)) * S(y,x); % Mol gas
dissolved per minute / time unit
                            % Qtarget * 1-Quality = water flow
            CO2Density(y,x) =
CO2GasDensity((273+21),Pressure(y,x)*100000)/1000000;  % Density in
[mol/mL]

            VolumeDissolved(y,x) = Dissolved(y,x)/CO2Density(y,x); % Volume
dissolved at core conditions

            GasFlow(y,x) = max(0,RawData(y,GasFlowColumn)/Z(y,x)-
VolumeDissolved(y,x)); % This is the remaining gasflow after subtracting
dissolved flow

        end
    end
end

if Gas == 1
    for x=1:size(Pressure,2)
        for y=1:size(Pressure,1)
    GasFlow(y,x) =
max(0,RawData(y,GasFlowColumn)/Z(y,x))*FlowmeterCorrection;
        end
    end

end


%% Calculate real total flow, apparent viscosity
RealFlow = zeros(size(Pressure,1),size(Pressure,2));                % Empty
matrix for real total flowrate
muInternal = zeros(1,size(Pressure,1));            % Empty matrix for
apparent viscosity (internal)
muExternal = zeros(1,size(Pressure,1));              % Empty matrix for
apparent viscosity (external)
for x=1:size(Pressure,2)
        for y=1:size(Pressure,1)
            RealFlow(y,x) = (1-Quality(y))*Qtarget+GasFlow(y,x);        %
Account for target flow rate.
        end
end
```

```
RealFlowSI = zeros(size(Pressure,1),size(Pressure,2));
for x=1:size(Pressure,2)
        for y=1:size(Pressure,1)
            RealFlowSI(y,x)=(RealFlow(y,x)/60)/1000000;
        end
end

% For the final plot the apparent viscosity, and REAL quality at inlet,
% outlet and average is required. The REAL quality = GasFlow/ ( (1-Quality)
% + GasFlow)

RealQuality = zeros(size(Pressure,1),size(Pressure,2));
for x=1:size(Pressure,2)
        for y=1:size(Pressure,1)
            RealQuality(y,x)=GasFlow(y,x)/(((1-
Quality(y))*Qtarget)+GasFlow(y,x)); % Calculates real quality
        end
end

for y=1:size(Pressure,1)

muInternal(y)=k*A/RealFlowSI(y,2)*RawData(y,InternalColumn)*100000/L(1); %
Note pressure changed to SI (*100000)

muExternal(y)=k*A/RealFlowSI(y,2)*RawData(y,ExternalColumn)*100000/L(2);
end

%% Plotting routines
close all
figure(1)
scatter(Quality(:),RawData(:,ExternalColumn),'r*')
% axis[xmin xmax ymin ymax])
ylabel('Pressure drop [bar]')
xlabel('Quality [-]')
title('Pressure drop')
legend(['Q = 1,0 mL/min', 10, 'k = 1,78 D Bentheim SST',10,'0,0315% AS-40,
H_2O + N_2'],'Location','South')
axis([0 1 0 6])

figure(2)
hold on
scatter(RealQuality(:,1),muExternal,'b.')
scatter(RealQuality(:,2),muExternal,'g*')
scatter(RealQuality(:,3),muExternal,'b.')
for y=1:length(RealQuality)
    plot([RealQuality(y,1),RealQuality(y,3)],[muExternal(y),
muExternal(y)])
end
axis([0 1 0 0.4])
ylabel('Apparent viscosity [Pa*s]')
xlabel('Actual quality [-]')
title('Apparent viscosity')
legend(['Q = 1,0 mL/min', 10, 'k = 1,78 D Bentheim SST',10,'0,0315% AS-40,
H_2O + N_2'],'Location','South')
hold off

%% Write apparent viscosity and average actual quality to output file
OutputQuality = (RealQuality(:,1)+RealQuality(:,3))/2;
OutputViscosity = muExternal';
Output = [OutputQuality, OutputViscosity];
xlswrite('ExpOParameterfitOutput',Output)
```

Model fitting

```
% estimating foam parameters for a 0.0315 wt% AOS and N2
clc;
%% data

Data = xlsread('ExpOParameterfitOutput.xls');
fg_exp = Data(:,1);% Gas fraction from experimental data
muf_exp = Data(:,2); % Viscosity from experimental data

%% Apparent viscosity, calculated from experimental data

[muf_t, muf_t_ind] = max(muf_exp);  % Finds maximum apparent viscosity, and
returns index of that viscosity in matrix muf_exp
w = ones(length(muf_exp), 1);       % Creates 1-matrix
w(muf_t_ind) = 1;                   % Puts value at index of max muf_exp at
1. This is a weight factor for fitting the maximum value in the model.

sigma_wg = 0.027;    % [N/m]
k = 1.78e-12;          % [m^2]
A = pi()*0.038^2/4; % [m^2] cross section area of the core
u = 1e-6/60/A;      % [m/s]

Nca_exp = u*muf_exp/sigma_wg; % Capillary number, one for each data point

%% Define the functions

swc = 0.1443;     % Connate water saturation
sgr = 0.0594;      % Residual gas saturation
krg0 = 0.9560;       % Gas end relperm
ng = 1.4293;         % Exponent kg curve
krw0 = 0.2843;       % Water end relperm
nw = 3.9173;         % Exponent kw curve
% swc = 0.07;     % Connate water saturation
% sgr = 0.0;      % Residual gas saturation
% krg0 = 1;       % Gas end relperm
% ng = 2;         % Exponent kg curve
% krw0 = 1;       % Water end relperm
% nw = 2;         % Exponent kw curve

sws = @(sw)((sw>swc).*(sw-swc)/(1-sgr-swc)); % Function for calculation of
sws
kr = @(sw)(krg0*(1-sws(sw)).^ng);            % Function for calculation of
relative permeability in case of no foam

% F2(1) = fmmob
% F2(2) = epdry
% F2(3) = fmdry
% F5(1) = fmcap
% F5(2) = epcap
fm = @(sw, F2)(1+F2(1)*(0.5+atan(F2(2).*(sw-F2(3)))/pi())); % Function
which calculates (1 + fmmob * F2)
krg = @(sw, F2)(kr(sw)./fm(sw, F2));                        % Calculates
relative gas permeability in case of foam (kg_nofoam*FM)
krw = @(sw)(krw0*sws(sw).^nw);                              % Calculates
relative water permeability

%% Physical properties
muw = 3.55e-04; % Pa.s
```

```
% mug = 2e-5; % Pa.s
mug = N2viscosity(80e5,273+25); %Pa.s

%% Define the main objective functions
fg = @(sw, F2)((krg(sw,F2)/mug)./(krw(sw)/muw+krg(sw,F2)/mug));     % Main
functions in CMG-STARS model are calculations of fg and mu_foam
mu_foam = @(sw, F2)(1./(krw(sw)/muw+krg(sw, F2)/mug));

%% Yet another objective function
sw = swc:0.0001:1-sgr;
% Range of water saturations to explore between connate water and residual
gas
Fun5 = @(x)(w.*abs(interp1(fg(sw, x), mu_foam(sw,x), fg_exp)-muf_exp));
% Multiplies weight factor with absolute interpolated values of all points
in fg(sw,x) of function mu_foam(sw,x) and subtracts the experimentally
measured data
x_guess5 = [10000 500 0.3];
% Some initial guess
[x_new5, fval5]=lsqnonlin(Fun5, x_guess5,...
% Finds the values for which the least-square error of the measured values
with the modelled values is the smallest.
    [1000 10 swc], [500000 10000 krw0]);
% States lower and upper boundaries
fmmob = sprintf('%0.5e',x_new5(1))                    % Reference mobility
reduction factor in foam model (larger = stronger foam)
epdry = sprintf('%0.5e',x_new5(2))                    % Parameter regulating
slope (abruptness) of dry-out function
fmdry = sprintf('%0.5e',x_new5(3))                    % Critical water
saturation. Below this saturation foam collapses in model

%% plot the final results
x=x_new5(1:3);                                        % Reads the result from
least-square error optimization
fg_cal = fg(sw, [x(1) x(2) x(3)]);                    % Calculates fg at
points sw for calculated fmmob, epdry and fmdry
muf_cal = mu_foam(sw, [x(1) x(2) x(3)]);              % Calculates muf at
points sw for calculated fmmob,epdry and fmdry
[muf_t, muf_t_ind] = max(muf_cal);
sw_t = sprintf('%0.5e',sw(muf_t_ind))

figure(1);subplot(1,2,1);plot(fg_cal, muf_cal, '.', fg_exp, muf_exp, 'o')
xlabel('Foam quality (f_g)'); ylabel('apparent viscosity [Pa.s]')
subplot(1,2,2); plot(fg_cal, sw)
xlabel('Foam quality (f_g)'); ylabel('Liquid saturation (S_w)')

%% Including capillary pressure
Fun6 = @(x)(w.*abs(objfun_foam(x(1:3), x(4:5), fg_exp)-muf_exp));   %
Multiplies the weight factor with the difference between the measured
values for muf and the ones calculated by the objfun_foam function. This
includes F5.
x_guess5 = [x_new5 2e-5 1.1];                                        % The
initial guess, using the result from the previous simulation with 2
estimates for fmcap and epcap.
[x_new6, fval6]=lsqnonlin(Fun6, x_guess5,...                         % Finds
the values for which the least-square error of the measured values with the
modelled values is the smallest.
    [1000 10 swc 1e-6 0.5], [500000 5000000 swc+0.4 2e-3 5])
fmmob = sprintf('%0.5e',x_new6(1))
epdry = sprintf('%0.5e',x_new6(2))
fmdry = sprintf('%0.5e',x_new6(3))
```

```
fmcap = sprintf('%0.5e',x_new6(4))
epcap = sprintf('%0.5e',x_new6(5))

%% visualize the results
% x_new = [1.0532e+05   5.0000e+03   1.2000e-01   1.0335e-04    8.0000e-
01];
[~, f1, f2] = objfun_foam(x_new6(1:3), x_new6(4:5), fg_exp);
muf_cal = f2(fg_cal);

figure(2);
hold on
plot(fg_cal, muf_cal, '.', fg_exp, muf_exp, 'g*')
scatter(RealQuality(:,1),muExternal,'g.')
scatter(RealQuality(:,3),muExternal,'g.')
for y=1:length(RealQuality)
    plot([RealQuality(y,1),RealQuality(y,3)],[muExternal(y),
muExternal(y)])
end
xlabel('Foam quality (f_g)'); ylabel('apparent viscosity [Pa.s]')
legend(['fmmob =' fmmob,10,'epdry =' epdry,10,'fmdry =' fmdry,10,'fmcap ='
fmcap,10,'epcap =' epcap],'Location','NorthWest')
hold off


%% Extra fancy stuff just in case
% options = gaoptimset;
% options.Generations = 1000;
% options.TolFun = 1e-30;
% [x_new3, fval3] = ga(Fun2, 3, [],[],[],[], ...
%     [0 0 0 0], [200000 100000 swt0 0.2], [], options)% x_guess3)
% options = psoptimset;
% options.MaxIter = 10000;
% options.TolMesh = 1e-30;
% options.TolX = 1e-30;
% options.TolFun = 1e-30;
% [x_new3, fval3] = patternsearch(Fun3, x_guess3, [],[],[],[], ...
%     [0 0 0 0], [200000 100000 0.15 0.2], [], options)% x_guess3)
```

Appendix B – Zeta potential measurements

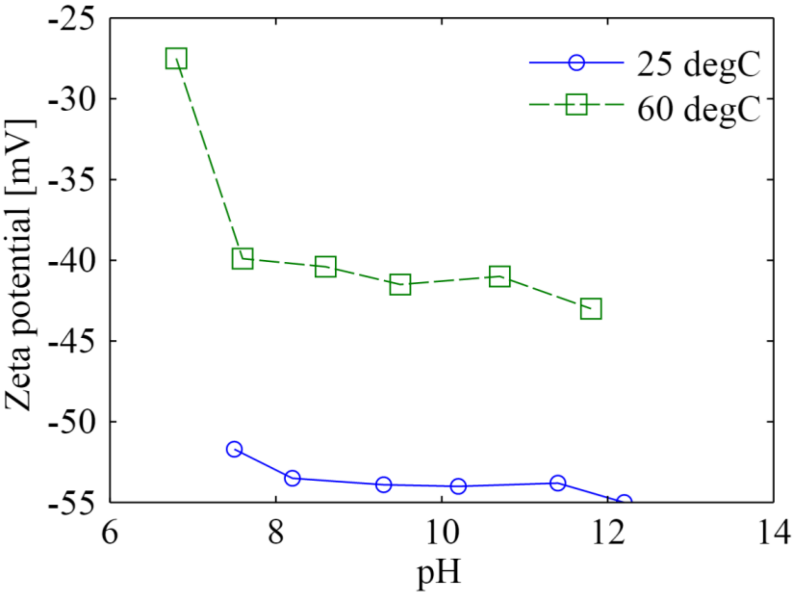

Figure 103: Zeta potential for different temperatures

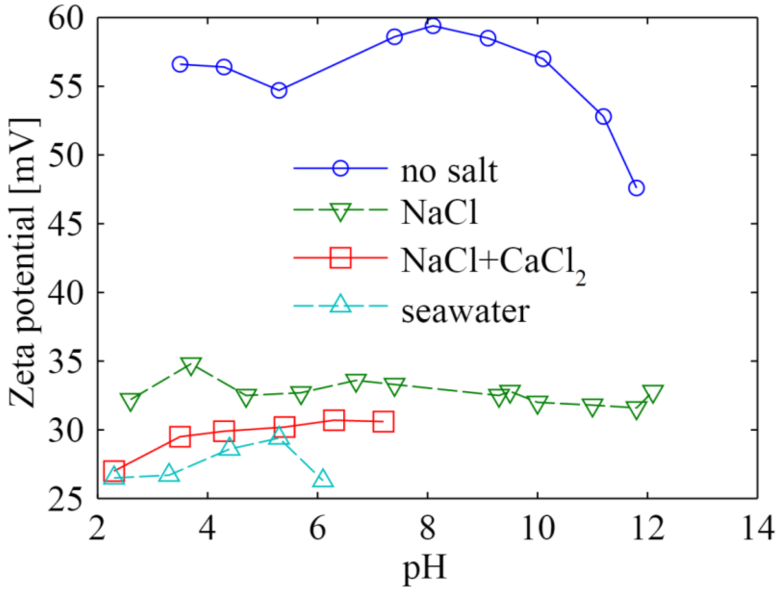

Figure 104: Zeta potential for different salts (AMMONYX surfactant)

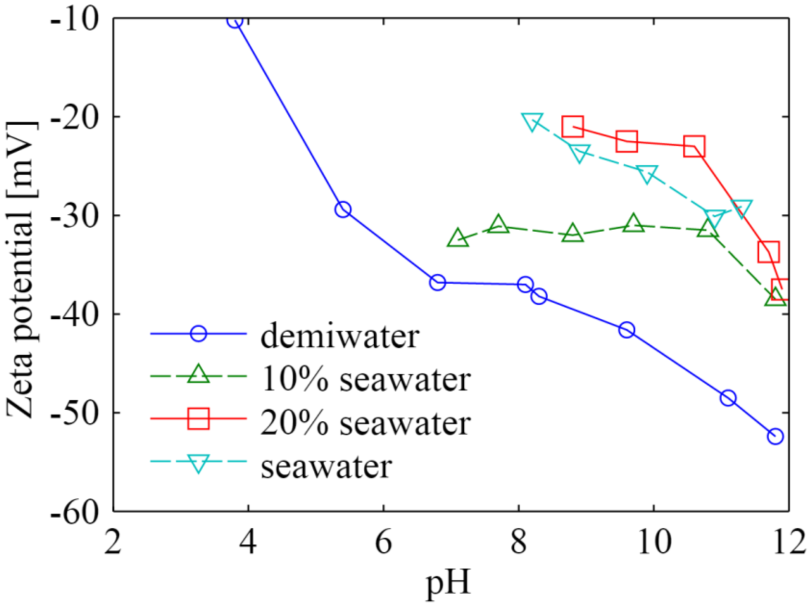

Figure 105: Zeta potential for seawater concentrations

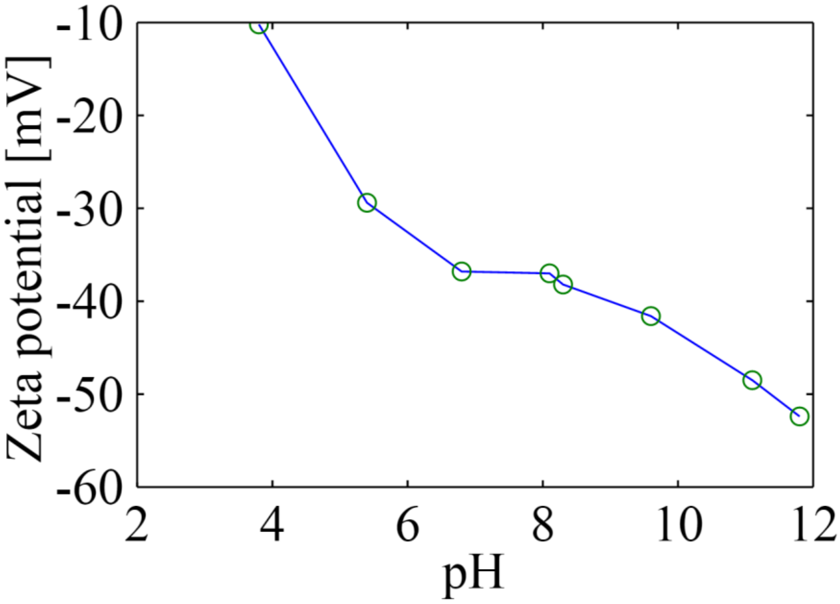

Figure 106: Zeta potential for 1 mM AOS as function of pH